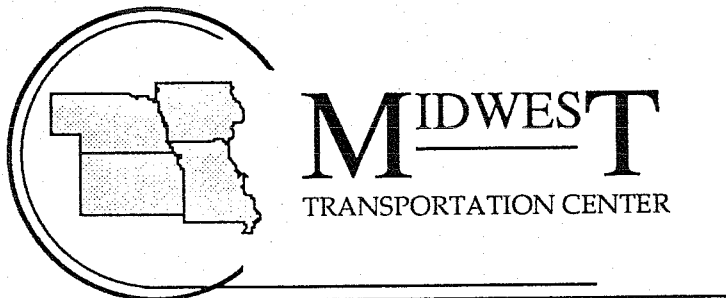


**DYNAMIC SIMULATION METHODS
FOR EVALUATING VEHICLE
CONFIGURATION AND ROADWAY DESIGN**

Prepared by
The University of Iowa
Public Policy Center
in conjunction with the
Midwest Transportation Center

July, 1991



Commissioned by the
Midwest Transportation Center
A Consortium of Iowa State University
and The University of Iowa

Director

Thomas H. Maze, Ph.D.
Manager, Iowa Transportation
Center
Associate Professor of Civil and
Construction Engineering
Iowa State University

Associate Director

David J. Forkenbrock, Ph.D.
Director, Public Policy Center
Professor of Urban and Regional
Planning and
Civil and Environmental
Engineering
The University of Iowa

Advisory Committee

Barbara J. Dunn, Former Executive Director, Public Transit Association

William E. Greenwood, Chief Operating Officer, Burlington Northern Railroad

Allen A. Housh, Vice President of Transportation, Cargill, Incorporated

V. Kenneth Jensen, Federal Region VII Regional Administrator, Federal Highway Administration

John R. McKenzie, President, Alter Barge Line, Inc.

Larry Miller, President, Ruan Transportation Management Systems

Darrel Rensink, Director, Iowa Department of Transportation

Lee O. Waddleton, Federal Region VII Area Director, Urban Mass Transit Administration

Public Policy Center
227 South Quad
University of Iowa
Iowa City, Iowa 52242
Phone: (319) 335-6800
Fax: (319) 335-6801

DYNAMIC SIMULATION METHODS FOR EVALUATING VEHICLE CONFIGURATION AND ROADWAY DESIGN

James W. Stoner

M. Asghar Bhatti

S. S. Kim

James E. Bernard

J. P. Idelin Molinas Vega

Carlos Quintero Febres

Bryce A. Amhof

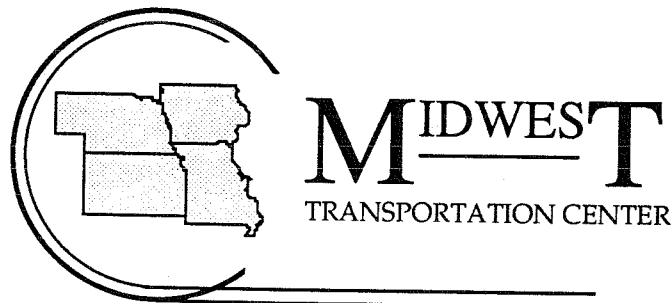
J. K. Koo

Scott W. Stearns

Norman S. J. Foster

Prepared by
The University of Iowa
Public Policy Center
in conjunction with the
Midwest Transportation Center

July, 1991



PREFACE

This report is the product of a second-year research project in the University Transportation Centers Program. The Program was created by Congress in 1987 to "contribute to the solution of important regional and national transportation problems." A university-based center was established in each of ten federal regions following a national competition in 1988. Each center has a unique theme and research purpose, although all are interdisciplinary and also have educational missions.

The Midwest Transportation Center is one of the ten centers; it is a consortium that includes Iowa State University (lead institution) and The University of Iowa. The Center serves federal Region 7 which includes Iowa, Kansas, Missouri, and Nebraska. Its theme is "transportation actions and strategies in a region undergoing major social and economic transition." Research projects conducted through the Center bring together the collective talents of faculty, staff, and students within the region to address issues related to this important theme.

This particular project was carried out by an interdisciplinary research team at The University of Iowa's Public Policy Center. This center is a reflection of the University's renewed commitment to applied research that seeks to advance the public interest. The Center's projects generally involve close interaction with decision makers and resource people in both the public and private sectors.

The project is central to the Midwest Transportation Center's theme in that it examines the relationship between road highway design and allowable truck axle weights and configurations. The principal investigator was Professor James W. Stoner, Civil and Environmental Engineering. Co-investigators were Professors Sang Sup Kim, Mechanical Engineering; Asghar Bhatti, Civil and Environmental Engineering; and James Bernard, Mechanical Engineering, Iowa State University. They were assisted by Jakyum Koo, Carlos Quintero Febres, and Idelin Molinas-Vega, graduate students in Engineering, and Bryce Amhof and Scott Stearns, undergraduate students in Civil and Environmental Engineering. Support services for computing were provided by the Center for Simulation and Design Optimization and the Public Policy Center at the University of Iowa.

ACKNOWLEDGMENTS

The research and development performed during the second year of this project required the assistance of many people. The Project Advisory Committee satisfied many of our critical data needs, assisted in the preparation of our work program, and reviewed our drafts of this report. Members of the Advisory Committee included Bill McCall and Brian McWaters of the Iowa Department of Transportation; Bill Giles of the Ruan Companies; and Charley Powell of Navistar. In addition, staff members at the Iowa Department of Transportation provided advice and data, specifically Charlie Potter and Samil Sermet.

The University Transportation Centers Program of the U.S. Department of Transportation deserves our thanks for making it possible to carry out this research. Also, Professor Maze and his colleagues at Iowa State University provided direction and administrative guidance that helped us through the project.

Anita Makuluni edited the report, while our other associates at the Public Policy Center assisted us in numerous ways. We thank them all.

CONTENTS

PREFACE	iii
ACKNOWLEDGMENTS	v
LIST OF FIGURES	xi
LIST OF TABLES	xv
1. INTRODUCTION.....	1
Previous Research	1
Vehicle Load History Studies	1
Pavement Analysis	2
Research Summary.....	3
2. TRUCK MODELING	5
Introduction	5
Review of Phase I	5
Overview of Phase II.....	5
Truck Modeling	6
Multibody Dynamic Formulation	7
Recursive Kinematics	8
Recursive Dynamics	13
Truck Subsystem Models	18
Spring Models	18
Translational Spring Damper Force Model.....	18
Rotational Spring-Damper Force Model.....	19
Leaf Spring Force Model	20
Air Bag Spring	21
Tire/Road Models	22
Radial Spring Tire Model	23
Point Follower Tire Model	23
Suspension Models	23
Structure of Truck Simulation Program	25
Truck Modeling Program	25
Dynamic Analysis Program	27

Performance Analysis Program	27
Aggregated Force	27
Dynamic Load Coefficient	28
Simulations and Discussions	29
Program Validation	29
Quarter Truck Model	29
Double Truck Model	31
Parametric Studies	31
3. PAVEMENT MODELING	37
Pavement Evaluation	37
Pavement Response Analysis Procedure	37
Dynamic Force Estimates at Tire-Pavement Contact Points	37
Pavement Response Analysis Calculations	37
Generation of Influence Curves	37
Response Curve for a Particular Node	37
Parametric Study	38
Results of Parametric Studies	38
Nominal Case	39
One-Third Payload	39
Presentation of Response Results for Each Case	39
Two-Thirds Payload	41
Reduction of Tire Stiffness by 10 Percent	41
Reduction of Tire Stiffness by 20 Percent	41
Increase of Leaf Spring Stiffness by 10 Percent	41
Decrease of Leaf Spring Stiffness by 10 Percent	41
Comparative Analysis	42
Rigid Pavement Representation	49
Concrete Modeling	49
Concrete in Compression	49
The Yield Surface and Flow Rule	49
The Crushing Condition	50
Concrete in Tension	52
Stress-Strain Relations for Cracked Systems	52
Tension Stiffening	53
Steel in Compression and in Tension	54
Fatigue of Concrete in Tension	54
Subgrade Model	58

Finite Element Model	58
Pumping Representation	59
Dowel Bar Model	60
Dowel Representation	60
Effect of Repetitive Loading	64
Examples of Pavement Model Formulation	65
Example 1	65
Results	66
Fatigue Damage	66
Pumping Damage	66
Example 2	75
Results	75
4. INTEGRATED SOFTWARE ENVIRONMENT	81
Introduction	81
Vehicle Modeling Front End Program	82
Vehicle Response Simulation and Post-Processing of Simulation Results	88
Pavement Modeling Front End Program	88
Pavement Response Simulation and Post-Processing of Simulation Results	90
APPENDIX	93
REFERENCES	97

LIST OF FIGURES

2-1	Typical Heavy Truck Configurations	6
2-2	Modular Truck Modeling Structure	7
2-3	Kinematic Parameters of Two Contiguous Bodies	9
2-4	A Rigid Body in a Plane	13
2-5	Single Chain of A Multibody System	15
2-6	Translational Spring-Damper-Actuator Model	19
2-7	Rotational Spring-Damper-Actuator Model	20
2-8	Point Follower Tire Model	23
2-9	Radial Spring Tire Model	23
2-10	Structure of Truck Simulation Program	25
2-11	Prototype of Quarter Truck Model	29
2-12	Multibody Configuration of 27-Foot Doubles Combination	30
2-13	Multibody Configuration of Eighteen Wheeler Tractor and Semitrailer Combination	30
2-14	Half Inch Faulting Road Profile	32
2-15	Rough Random Road Profile	32
2-16	Smooth Random Road Profile	32
2-17	Comparison of Axle Load of Quarter Truck, With TSDA Spring	34
2-18	Comparison of Axle Load of Quarter Truck, With Leaf Spring	34
2-19	Comparison of Second Axle Load of Double Truck, With TSDA Spring ..	34
2-20	Comparison of Fourth Axle Load of Double Truck, With TSDA Spring ..	35
2-21	Comparison of Axle Load of Leading Tandem Axle of Tractor	35
2-22	Comparison of Axle Load of Leading Tandem Axle of Semitrailer	35
3-1	Pavement Model for Parametric Study	38
3-2	Travelling Path on Test Slabs	39
3-3	First Axle Forces (65 mph, nominal case, rough profile)	40
3-4	Second and Third Axle Forces (65 mph, nominal case, rough profile) ...	40
3-5	Fourth and Fifth Axle Forces (65 mph, nominal case, rough profile)	40
3-6	Maximum Pavement Displacement (65 mph, nominal case, rough profile)	41
3-7a	Maximum Pavement Displacements for 45 mph	42
3-7b	Maximum Pavement Displacements for 65 mph	42
3-8a	Maximum Pavement Displacements for Rough Profile	43
3-8b	Maximum Pavement Displacements for Smooth Profile	43
3-9	Envelopes of Maximum Pavement Displacements for 45 mph on Rough Profile With Reduction of Payload	44
3-10	Envelopes of Maximum Pavement Displacements for 45 mph on Smooth Profile With Reduction of Payload	44
3-11	Envelopes of Maximum Pavement Displacements for 65 mph on Rough Profile With Reduction of Payload	44
3-12	Envelopes of Maximum Pavement Displacements for 65 mph on Smooth Profile With Reduction of Payload	45
3-13	Envelopes of Maximum Pavement Displacements for 45 mph on Rough Profile With Reduction of Tire Stiffness	45
3-14	Envelopes of Maximum Pavement Displacements for 65 mph on Rough Profile With Reduction of Tire Stiffness	45

3-15	Envelopes of Maximum Pavement Displacements for 45 mph on Smooth Profile With Reduction of Tire Stiffness	46
3-16	Envelopes of Maximum Pavement Displacements for 65 mph on Smooth Profile With Reduction of Tire Stiffness	46
3-17	Envelopes of Maximum Pavement Displacements for 45 mph on Rough Profile With Changes in Leaf Spring Thickness	46
3-18	Envelopes of Maximum Pavement Displacements for 65 mph on Rough Profile With Changes in Leaf Spring Thickness	47
3-19	Envelopes of Maximum Pavement Displacements for 45 mph on Smooth Profile With Changes in Leaf Spring Thickness	47
3-20	Envelopes of Maximum Pavement Displacements for 65 mph on Smooth Profile With Changes in Leaf Spring Thickness	47
3-21a	Concrete Behavior Idealization: Comparison with Data from Kupfer, Hilsdorf, and Rusch (1969)	51
3-21b	Concrete Behavior Idealization: Uniaxial Stress-Strain Representation . .	51
3-22	Tension Stiffening Idealization	54
3-23	Endurance Curve for Concrete in Tension Under Cyclic Loading	56
3-24	Types of Subgrade Representation	58
3-25	Beam Element: Local Node Numbering and Degrees of Freedom	60
3-26	Relative Deformations Between Dowel Bar and Concrete Slab	62
3-27	Relative Deformation Between Dowel and Concrete Slab: (a) Under Shear Loading; and (b) Under Moment Loading	63
3-28	Finite Element Idealization of Dowel Bars	63
3-29a	Slab Geometry and Loads Used in Example 1	65
3-29b	Element Configuration and Layer Discretization for Example 1	66
3-30	Displacement Along Path A-A for Different Numbers of Cycles (Fatigue Only)	67
3-31	Normalized Displacements Under Fatigue Analysis.	67
3-32a	Stress Distribution, in X-Direction, At Bottom of Slab After One Load Repetition: Fatigue Damage Only	68
3-32b	Stress Distribution, in X-Direction, At Top of Slab After One Load Repetition: Fatigue Damage Only	68
3-33a	Stress Distribution, in Y-Direction, At Bottom of Slab After One Load Repetition: Fatigue Damage Only	68
3-33b	Stress Distribution, in Y-Direction, At Top of Slab After One Load Repetition: Fatigue Damage Only	68
3-34a	Stress Distribution, in X-Direction, At Bottom of Slab After 1,250,000 Load Repetitions: Fatigue Damage Only	69
3-34b	Stress Distribution, in X-Direction, At Top of Slab After 1,250,000 Load Repetitions: Fatigue Damage Only	69
3-35a	Stress Distribution, in Y-Direction, At Bottom of Slab After 1,250,000 Load Repetitions: Fatigue Damage Only	69
3-35b	Stress Distribution, in Y-Direction, At Top of Slab After 1,250,000 Load Repetitions: Fatigue Damage Only	69
3-36	Displacements Along Path A-A for Different Numbers of Load Applications For Pumping Damage Analysis	70
3-37	Volume of Material Ejected For Different Numbers of Load Applications During Pumping Damage Analysis	70

3-38	Void Distribution Due to Pumping After 100,000 Load Repetitions	70
3-39	Void Distribution Due to Pumping After 250,000 Load Repetitions	71
3-40	Void Distribution Due to Pumping After 500,000 Load Repetitions	71
3-41	Void Distribution Due to Pumping After 750,000 Load Repetitions	71
3-42	Void Distribution Due to Pumping After 1,000,000 Load Repetitions	71
3-43a	Maximum Principal Stress Distribution At Bottom of Slab After One Load Repetition: Pumping Damage Only	72
3-43b	Maximum Principal Stress Distribution At Top of Slab After One Load Repetition: Pumping Damage Only	72
3-44a	Minimum Principal Stress Distribution At Bottom of Slab After One Load Repetition: Pumping Damage Only	72
3-44b	Minimum Principal Stress Distribution At Top of Slab After One Load Repetition: Pumping Damage Only	72
3-45a	Maximum Principal Stress Distribution At Bottom of Slab After 250,000 Load Repetitions: Pumping Damage Only	73
3-45b	Maximum Principal Stress Distribution At Top of Slab After 250,000 Load Repetitions: Pumping Damage Only	73
3-46a	Minimum Principal Stress Distribution At Bottom of Slab After 250,000 Load Repetitions: Pumping Damage Only	73
3-46b	Minimum Principal Stress Distribution At Top of Slab After 250,000 Load Repetitions: Pumping Damage Only	73
3-47a	Maximum Principal Stress Distribution At Bottom of Slab After 750,000 Load Repetitions: Pumping Damage Only	74
3-47b	Maximum Principal Stress Distribution At Top of Slab After 750,000 Load Repetitions: Pumping Damage Only	74
3-48a	Minimum Principal Stress Distribution At Bottom of Slab After 750,000 Load Repetitions: Pumping Damage Only	74
3-48b	Minimum Principal Stress Distribution At Top of Slab After 750,000 Load Repetitions: Pumping Damage Only	74
3-49	Slab Configuration Used in Example 2	75
3-50	Calculated Deflection for Different Gradients of Temperature	76
3-51	Displacements Calculated with a Temperature Gradient of 0.0 F/in.	77
3-52	Displacements Calculated with a Temperature Gradient of +1.5 F/in.	77
3-53	Displacements Calculated with a Temperature Gradient of -1.5 F/in.	77
3-54	Effect of Temperature Gradient on Displacements After One Load Application	78
3-55	Effect of Temperature Gradient on Displacements After 100,000 Load Applications	78
3-56	Effect of Temperature Gradient on Displacements After 500,000 Load Applications	78
3-57	Effect of Temperature Gradient on Displacements After 1,000,000 Load Applications	79
3-58	Effect of Temperature Gradient in Pumped Material For Different Numbers of Load Applications	79
4-1	An Overview of the Integrated Software Environment	81
4-2	Vehicle Modeling Choices	83
4-3	Simulation Control Card	83
4-4	Tandem-Axle Tractor Data	84

4-5	Tractor Front Tire and Wheel Parameters	84
4-6	Tractor Front Axle Parameters	85
4-7	Tractor Rear Axle Parameters	85
4-8	Trailer Parameters	86
4-9	Trailer Payload Parameters	86
4-10	Trailer Rear Tire and Wheel Parameters	87
4-11	Trailer Rear Axle Parameters	87
4-12	Pavement Slab Data	89
4-13	Pavement Discretization Into Finite Elements	89
4-14	Dowel Data	90
4-15	Truck Travel Path	91
4-16	General Pavement Analysis Information	91

LIST OF TABLES

2-1	Library of Truck Subsystem Models	24
2-2	Truck Subsystem Library and Parameters Considered	26
2-3	CPU Time Comparison Between DADS and Recursive Code For Five-Second Simulation (seconds)	31
2-4	Dynamic Load Coefficients for Varying Tire Spring Stiffness	33
2-5	Dynamic Load Coefficients for Varying Leaf Spring Stiffness	36
2-6	Dynamic Load Coefficients for Varying Payload (Full Payload = 2,884 N)	36
3-1	Axles Causing Maximum Deflections for Different Load Conditions	48

1. INTRODUCTION

This report documents three elements of a two-year project conducted under the direction of the Midwest Transportation Center. The first element, a comprehensive two-dimensional truck simulation, has a modular program construction to allow variation of vehicle characteristics, and is able to predict vehicle motion and the tire-road surface interaction forces. The second element is a rigid pavement model that is used to determine slab deflection, cracking, and stress at predetermined nodes. The pavement model allows for user control of traditional thickness design factors. The third and final element describes the implementation of both modeling systems using a work station with menu driven modules and Hypercard interfaces, allowing both existing and proposed pavements to be evaluated given specific characteristics of the heavy vehicles that will be using the facility. This modeling package will assist the Departments of Transportation in their evaluation of maintenance procedures and determination of appropriate performance standards for urban and rural highway segments and commercial highway networks. This report presents the results of and documents the work that has been performed during this two-year study.

Previous Research

Vehicle Load History Studies

Modeling of different truck configurations has been performed by researchers throughout the world, but there are only three research groups currently working with computer models of heavy vehicles to predict dynamic loads: UMTRI at the University of Michigan, the Massachusetts Institute of Technology, and CCAD at the University of Iowa. Other research measuring normal forces produced by vehicles has used instruments implanted in or placed on the roadway, shaker tables under actual vehicles, and instrumented truck axles.

Dynamic loads are traditionally typified by two statistics: the dynamic load coefficient, that is the standard deviation of the dynamic load divided by the static load; and the peak load or impact factor.

Dynamic load is a significant component of the total force; but obviously, what goes up must come down, so the peak forces are distributed along the wheel path according to the wave forms that are produced by the frequencies excited by the road roughness or non-uniformities encountered in the road profile.

Smooth roads produce very small values of the Dynamic Load Coefficient (DLC), but even on relatively good roads, there is a significant difference in the performance of different suspension designs. Walking beam suspensions are the worst; while air bags, with DLC values roughly half those of the walking beam suspensions, are the best. Leaf springs are somewhere in between, with the value depending on the spring stiffness and axle spacing.

There is some difference of opinion concerning the effect of tire pressure, although in general tire pressures do not have a significant effect; they only increase the total axle loads a small amount, 5.5 percent for 125 psi versus 75 psi. The change in the contact patch and tire stiffness would cause considerable difference in the contact pressures on the pavement, a factor that could have considerable influence on flexible pavements. There is little effect for rigid pavement because of the shape of the influence function due to the bridging capability of the material.

Vehicle speed is an important factor, both in magnitude of the peak forces and the point where the maximum forces impact on the slab. At low speeds, dynamic contributions are minimal and the resulting forces are much like static load. There are critical mid-range speeds, 45-60 mph, where the specific vehicle and pavement characteristics combine to maximize tire forces. At higher speeds, the overall dynamic forces are reduced, but extremely rough pavement could excite some of the suspension modes and produce increased dynamic loads.

Pavement Analysis

Numerous analyses using several mathematical procedures have been performed on strains and deflections in pavement caused by the passage of heavy vehicles. Instrumented pavements have been used to gather experimental data, and complex finite element codes have been used to represent both rigid and flexible pavement layers. Flexible pavement is significantly different in terms of its response to load because of both the nature of the materials and the shape of the influence pattern, but both flexible and rigid pavements must eventually distribute the loads to the prepared subgrade and soil layers. A number of references describe traditional thickness design procedures and the analysis of strains, temperature differentials, deformation, and consequent damage to pavements. This interim study is concerned only with the response of rigid Portland Cement Concrete (PCC) pavement of the types typically found in Iowa.

A common measurement of stress is the deflection induced at specific points in the roadway. The road stress factor, which is the fourth power of the ratio of the peak force at a point to the mean force, or static load, has been used to summarize the effect of loads on pavement. This measure, however, has been seriously questioned in recent studies (Small, Winston, and Evans, 1989). There is considerable variation in the loads along the wheel path. The most conservative studies estimate at least a 25 percent point-to-point variation. The load pattern and the variation in load is determined by the variation in the road profile or, to some degree, the relative road roughness.

Previous studies have shown that the height of a joint fault or bump is directly related to the magnitude of the peak load or impact force, but it does not affect the relative location of impact. The increase in magnitude appears to be a power function of the height of the deformation. Slab warp has been found to have considerable influence on both location and magnitude of peak loads. The determining factors are slab length, displacement, slab radius of curvature, vehicle speed, and axle spacing and configuration. Overall low levels of slab roughness seem to have little effect on the dynamic loads. The deformation at rigid pavement joints were the primary factor in excitation of the vehicle modes.

The response of the pavement in terms of deflection and eventual plastic deformation of the subgrade, is related to the bearing capacity or support value of the stabilized or natural base. As previously stated, this can be a function of many climatic and environmental characteristics.

Research Summary

Vehicle models of tractor-trailer combinations were created using a specialized code based on an efficient recursive multibody dynamic formulation for simulating mechanical systems. Wheel load histories for individual vehicles are estimated for the wheel path of a sequence of doweled portland cement concrete slabs defined by the user. The specifications for the axle, tires, suspension, and drive train; and the dimensions and structural descriptions of the vehicle components can be obtained from the manufacturer's data or can be based on an analyst's assumptions. A finite element structural analysis program was developed to model the pavement, allowing estimation of strains and displacements on and within the slab and at the doweled joints. The model was validated using results obtained from other finite element codes and experimental results.

The modeling process can be viewed from the perspective of both the vehicle and the roadway. The variables and the modeling procedures are different, but there is necessary interaction between the two. The tractor-trailer combination generates wheel load forces from both the sprung and unsprung vehicle mass as it moves down the highway. The variables affecting the magnitude of the dynamic load include specific vehicle or vehicle type characteristics such as axle load; load distribution; suspension type, design and condition; tire stiffness; axle spacing and load leveling; and tire and wheel configuration. Operating conditions such as vehicle speed, road surface roughness and irregularities, geometric design of the roadway, and even environmental conditions, can also have significant influence.

The rigid pavement suffers some displacement as the load is applied through normal tire forces on the surface. The load is distributed and transferred to the subgrade and soil, whose support value is determined by soil or aggregate type and modified by the soil stabilization, temperature, and moisture content. The properties of the concrete include the modulus of rupture, thickness, and load transfer efficiencies at the longitudinal and transverse joints. The slab may contain surface deformities and warp and curl induced by the natural curing process or internal temperature differences. Displacement also occurs during the traversing of the axle loads, causing some deformation and skewing of the slab. The ability of the slab to distribute and accommodate load is often a function of the cracking, faulting, and other damage resulting from cumulative repetitions of axle loads.

Computer runs were performed during this study, varying the parameters defining both vehicle and road elements. For the vehicle, these included speed, weight and weight distribution, suspension type, tire pressures, and load leveling capability of the suspension. For the roadway, the sensitivity of results is related to road roughness, bumps or faults at the joints, soil support values, slab warp and curl, and load distribution and concurrent displacement induced by the vehicle passing over the slabs.

The resulting displacements for each pavement node are plotted, and the displacement basin defined. Relative damage to the pavement can then be estimated, using a damage function based on load replication. The results of individual or cumulative computer runs can be displayed and plotted as an integral part of the modeling package.

The objectives of the research were to create a set of tools for policy analysis affecting decisions on allowable vehicle configurations and roadway design and maintenance. The parametric studies discussed in this report are limited to a traditional 48-foot semitrailer operating under different loading conditions on an 11-inch rigid pavement with different levels of road roughness. The difference in dynamic load and slab displacement between

smooth, new construction paving and that exhibiting moderate roughness and mild cracking was not significant. The effects of pavement conditions are best exhibited by comparing new paving exhibiting Pavement Serviceability Index (PSI) values of 4.0-4.5 with pavement at the 2.0-2.5 PSI level.

Generally speaking, the rough pavement greatly accentuates the dynamic load, causes much greater pavement damage at critical speeds, and causes the relative damage from progressively heavier axle loads to increase at a much faster rate. Damage also increases with speed for smooth pavement, but does not increase directly with speed for rough conditions. The effects of the vehicle component variables such as the tire and leaf spring stiffness are presented in Chapter 3. The effects of temperature gradients and subsoil conditions contribute significantly to the creation of pumping conditions that ultimately result in joint failure and extensive D-cracking.

The model structure seems to bear considerable promise in pavement evaluation. The modular construction of the program and the use of off-the-shelf interfaces and post-processing programs contribute to the adaptability and ease of modification for the computer program.

The next phase of the study will use the model structure to look at the ability of pavements in Iowa to accommodate heavier and longer commercial vehicles on a designated commercial vehicle network. The freight movement studies conducted as part of the Midwest Transportation Center project, will be used to provide estimates of commercial vehicle movements and traffic composition on different segments of the network.

The alternative vehicle configurations; including various multi-trailer, single, tandem, and tridem axle combinations; alternate suspension systems; and higher payload limits will be identified and the relative impact loads and dynamic load coefficients estimated. The various roadway cross-sectional design standards can be modeled to determine the effective displacements and stresses. The required commercial network standards and vehicle limits can be evaluated prior to actual experience.

The existing model structure can be modified to utilize alternate damage models and pavement response if better approaches can be identified. It will be an evolving process to determine the best use with respect to integrating the procedures with traditional pavement design techniques and validating the modeling assumptions.

2. TRUCK MODELING

Introduction

Review of Phase I

Recent studies of the dynamic response of heavy vehicles (MacAdam et al., 1980; Sayers and Gillespie, 1983; Markow et al., 1988; Cebon, 1988a, 1988b) have involved manual writing of equations of motion for a specific truck or its components. Federal studies have used this hand-tailored method to define equations of motion for several types of tractor and trailer combinations.

The equations are solved using linear analysis of the linearized equations of motion, or numerical integration of the nonlinear equations for specific maneuvers and loading conditions. Manual derivation of the necessary equations of motion for such a system is time-consuming and prone to error. Also, any change in truck type or specific components, or even a slight modeling variation during parametric studies may result in very expensive new derivations and, consequently, new programming activities.

A general purpose, multibody system analysis program has the advantage of automatically defining the equations of motion for any arbitrary assembly of links and constraints. DADS, Dynamic Analysis and Design System (Computer Aided Design Software, Inc., 1988), was used to model a typical tractor and semitrailer under various simulation environments during Phase I of this study. Because DADS is structured as a combination of individually modulated subroutines, it has become advantageous to attach truck subsystem models, such as tires and leaf spring, to the existing DADS code.

A two-dimensional model of a typical 3-S2 tractor and semitrailer combination was created using the DADS code for the initial truck and pavement interaction studies. Computer runs have been performed, varying the parameters that define truck elements such as truck speed, weight distribution, suspension types, and load leveling capabilities of the suspension.

Overview of Phase II

Truck simulations have traditionally used general purpose multibody dynamics software emphasizing the generality of the formulations (Wehage and Haug, 1982; Orlandea, Chase, and Calahn, 1977; Schiehlen, 1990). DADS is an example of a commercially available computer program that can only be executed on mainframe computers, using the Cartesian coordinates as generalized coordinates. Each body in the system is referred to the same generalized coordinates; hence, the equations are easily formulated for computer implementation. This method results, however, in a maximal number of differential equations and constraints that significantly reduces numerical efficiency.

Practicality requires that any analytical procedures that are developed should be both efficient and generalizable to be used for routine design and evaluation. Any procedure that cannot be executed on a personal microcomputer will be considered too time-consuming and complex by most highway engineers. Direct use of a complete state-of-the-art dynamic analysis would require analytically-trained engineers with vehicle dynamics and finite elements experience.

The objective of the vehicle modeling segment of this study is to develop a comprehensive truck simulation tool that executes *fast*, has a *modular program construction* to allow variation of vehicle characteristics, and is able to realistically predict vehicle motion and tire-road surface interaction forces at a *workstation environment*. A general purpose truck simulation program was developed based on an efficient multibody formulation. A library of truck subsystem models was created, allowing a modular building block approach. An interface between the complex multibody data and conventional truck modeling descriptions was developed to promote ease of use.

Truck Modeling

Every simulation of a truck system starts with *modeling*, i.e., the definition of physical and mathematical models that behave analogous to the real truck. It is well known that models are problem dependent (i.e., only those motions that are of importance for evaluating a specific problem have to be considered). The type of truck determines how many bodies and the degrees of freedom that have to be assigned to a truck modeling system. Figure 2-1 illustrates typical truck configurations. Establishing meaningful models and describing required parameters remains the basic engineering art.

The following design assumptions are made:

1. A *two dimensional pitch plane simulation* is considered adequate for the truck and pavement interaction study.
2. A truck consists of a finite number of *rigid bodies*.
3. The multibody vehicle model will use a modular building block approach.

A modular building block approach for modeling trucks and their subsystems permits engineers to implement models of unique and even proprietary subsystem characteristics. This approach creates truck models that can be easily modified and combined to generate more sophisticated models. The modular structure employed in this study is diagrammed in Figure 2-2.

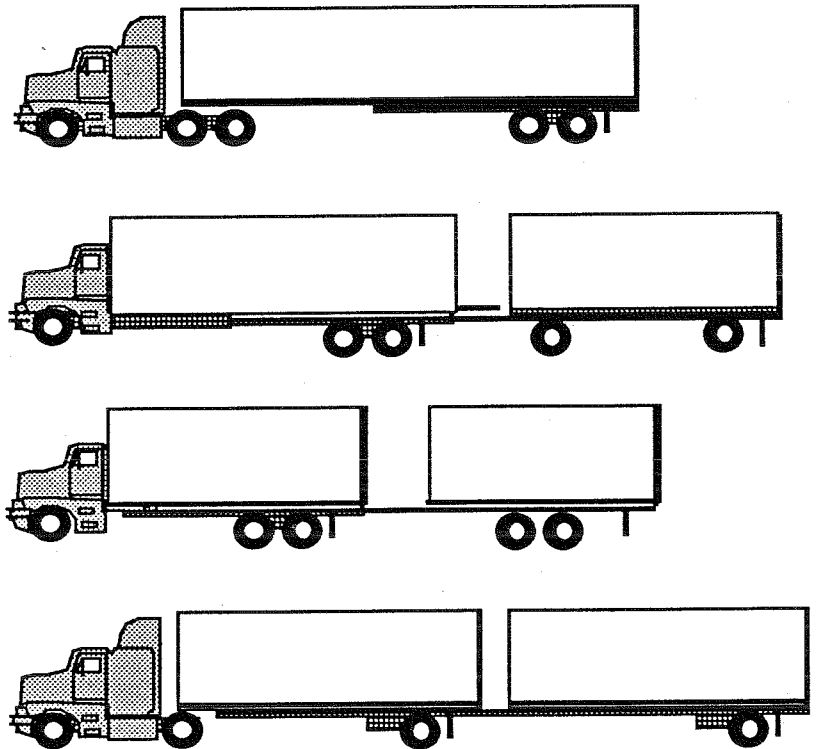


Figure 2-1
Typical Heavy Truck Configurations

There are two basic types of modules: A Truck Dynamics Equation Generator, and a set of Truck Subsystem Models. Interfaces are required to pass data for force computation to each of the Subsystem Models and to return forces to the Equation Generator.

A recursive multibody dynamic formulation is used for the Equation Generator, and has the advantage of automatically generating the equations of motion for any arbitrary assembly of bodies and joints. Details of the multibody dynamics formulation are described in the next section.

Multibody Dynamic Formulation

An important step in creating a mathematical truck model requires the creation of the equations of motion for truck dynamic simulation. The dynamic simulation is performed by solving the second order differential equations of motion to obtain values for the position, velocity, and acceleration of all rigid bodies in the model.

Recent, recursive dynamic formulations (Li, 1989; Walker and Orin, 1982; Featherstone, 1987) are considered to be the most efficient technique, taking advantage of the dynamic formulations based on Cartesian coordinates (systematically defining the initial system kinematics) and Lagrangian coordinates (resulting in the minimal set of differential equations). In this section, a recursive formulation based on the multibody system will be developed for a pitch plane truck model.

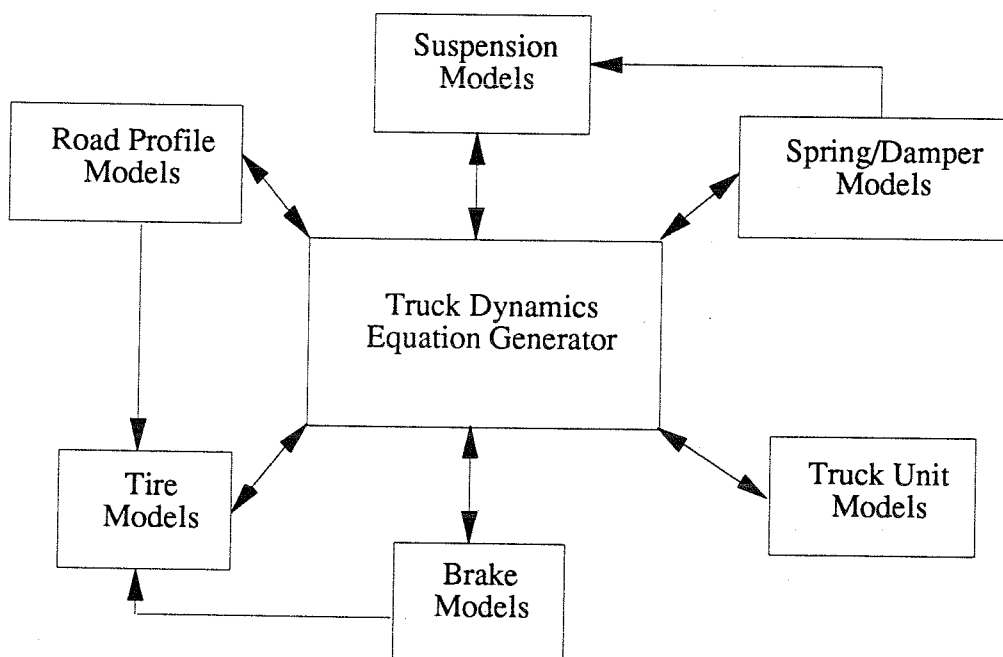


Figure 2-2
Modular Truck Modeling Structure

Recursive Kinematics

A two-dimensional recursive kinematics of two contiguous bodies is derived in this section. Figure 2-3 shows two bodies connected by a revolute-translational joint. A number of basic definitions and notations used in this section are as follows:

O_0	Origin of inertial reference frame X_0Y_0
O_i	Origin of joint-fixed local reference frame X_iY_i
P_{i-1}	Origin of body-fixed joint reference frame $\zeta_{i-1}\xi_{i-1}$ fixed to body $i-1$
A_i	The orientation matrix of body i with respect to the global reference frame
r_i^*	A position vector from O_0 to O_i referred to global reference frame (Note that a superscript asterisk $*$ denotes vectors defined in the global reference frame.)
r_i	A position vector from O_0 to O_i referred to the i th joint-fixed local reference frame; thus $r_i^* = A_i r_i$
ρ_{i-1}	A position vector from O_{i-1} to the center of mass of body $i-1$ referred to the joint-fixed local reference frame of body $i-1$
s_{i-1}	A position vector from O_{i-1} to P_{i-1} referred to joint-fixed local reference frame of body $i-1$
$d_{i,i-1}$	A position vector from O_{i-1} to O_i referred to joint-fixed local reference frame of body $i-1$
u_i	A unit vector along the Y axis of the joint-fixed local reference frame of body i

Initially, Cartesian coordinates are assigned to define the position of the bodies. The Cartesian coordinate vector for the i th body is defined as

$$z_i = [x_i, y_i, \theta_i]^T \quad (1)$$

where x_i and y_i are x and y components of the position vector r_i . θ_i is the rotational component of the i th body with respect to the global reference frame. This makes initial kinematic definition of a system very systematic and straightforward.

Relative joint coordinates are defined as relative angles f_i (for revolute joint) and relative distances t_i (for translational joint) to describe the relative motion of two contiguous bodies connected by kinematic joints. For example, if both rotational and translational motions are allowed between the two bodies, two generalized coordinates are assigned as

$$q_i = [t_i, f_i]^T \quad (2)$$

The kinematic equations are initially derived from global reference coordinates and then transformed to joint-fixed local reference coordinates. In general, bold lower and upper case letters represent vectors and matrices, respectively.

As shown in Figure 2-3, position vector r_i^* of body i can be represented by r_{i-1}^* of body $i-1$ and distance vector $d_{i,i-1}^*$ as

$$r_i^* = r_{i-1}^* + d_{i,i-1}^* \quad (3)$$

where

$$\mathbf{d}_{i,i-1}^* = \mathbf{s}_{i-1}^* + \mathbf{u}_i^* \tau_i \quad (4)$$

Substituting equation 4 into equation 3 yields

$$\mathbf{r}_i^* = \mathbf{r}_{i-1}^* + \mathbf{s}_{i-1}^* + \mathbf{u}_i^* \tau_i \quad (5)$$

Converting equation 5 into local joint-fixed frame,

$$\mathbf{A}_i \mathbf{r}_i = \mathbf{A}_{i-1} \mathbf{r}_{i-1} + \mathbf{A}_{i-1} \mathbf{s}_{i-1} + \mathbf{A}_i \mathbf{u}_i \tau_i \quad (6)$$

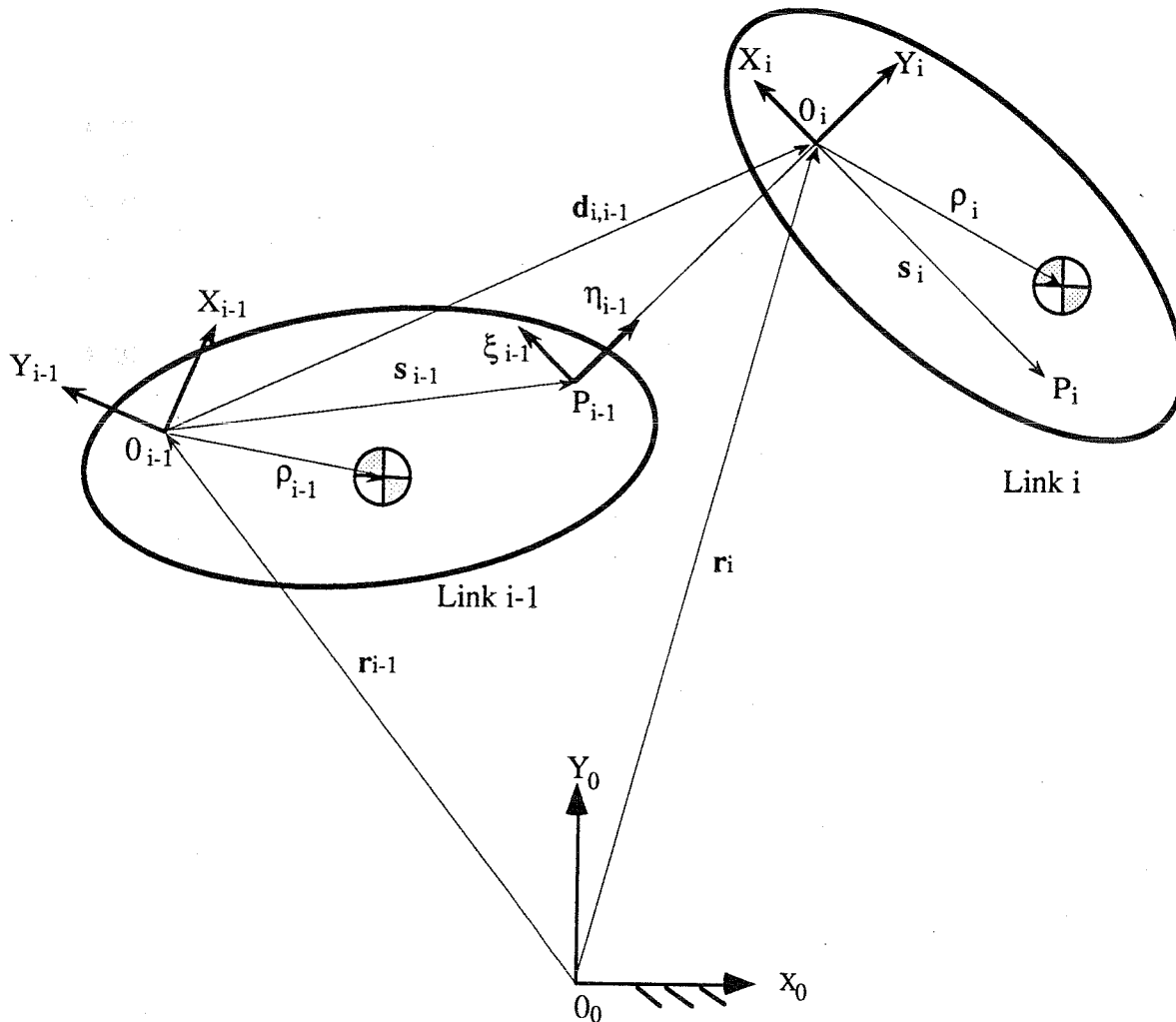


Figure 2-3
Kinematic Parameters of Two Contiguous Bodies

Premultiplying the transpose of the orientation matrix A_i on both sides, equation 6 can be rewritten in terms of local link coordinates,

$$\mathbf{r}_i = A_{i,i-1} \mathbf{r}_{i-1} + A_{i,i-1} \mathbf{s}_{i-1} + \mathbf{u}_i \tau_i \quad (7)$$

where

$$A_{i,i-1} \equiv A_i^T A_{i-1} = A(\phi_i) C_{i,i-1}$$

$C_{i,i-1}$ is a constant orientation matrix of x_{i-1}, h_{i-1} frame with respect to X_{i-1}, Y_{i-1} and $A(\phi_i)$ is a relative orientation matrix of X_i, Y_i with respect to x_{i-1}, h_{i-1} . Here, for the revolute joint,

$$A(\phi_i) = \begin{bmatrix} \cos\phi_i & \sin\phi_i \\ -\sin\phi_i & \cos\phi_i \end{bmatrix}$$

Note that locally transformed vectors s_{i-1} and u_i are defined in terms of the different local link coordinates. A second subscript means that a vector is defined at this link's coordinates and a first subscript indicates that the vector directs to the origin of that link's coordinates. For example, $d_{i,i-1}$ is the vector defined at the local link coordinates of body $i-1$ and directs to the origin of link reference frame of body i . If there is one subscript, this means that a vector is defined at these coordinates.

Angular velocity of body i is

$$\omega_i = \omega_{i-1} + \dot{\phi}_i \quad (8)$$

The time derivative of equations 3 and 4 are

$$\dot{\mathbf{r}}_i^* = \dot{\mathbf{r}}_{i-1}^* + \dot{\mathbf{d}}_{i,i-1}^* \quad (9)$$

$$\dot{\mathbf{d}}_{i,i-1}^* = \dot{\mathbf{s}}_{i-1}^* + \omega_{i-1} \mathbf{d}_{i,i-1}^{\perp*} + \mathbf{u}_i^* \dot{\tau}_i \quad (10)$$

$$\text{where } \mathbf{d}_{i,i-1}^{\perp*} = [d_y \ -d_x]^T$$

Substituting equation 10 into equation 9,

$$\dot{\mathbf{r}}_i^* = \dot{\mathbf{r}}_{i-1}^* + \omega_{i-1} \mathbf{d}_{i,i-1}^{\perp*} + \mathbf{u}_i^* \dot{\tau}_i \quad (11)$$

Define

$$\dot{\mathbf{r}}_i = A_i^T \dot{\mathbf{r}}_i^* \quad (12)$$

Similar to equation 6, premultiplying A_i on both sides of equation 11 and using equation 12, globally defined translational velocities in equation 11 can be converted into local translational velocities in each local link coordinate as

$$\dot{\mathbf{r}}_i = A_{i,i-1} \dot{\mathbf{r}}_{i-1} + \omega_{i-1} A_{i,i-1} \mathbf{d}_{i,i-1}^{\perp} + \mathbf{u}_i \dot{\tau}_i \quad (13)$$

Using equations 8 and 13, recursive velocity relation of the two contiguous bodies $i-1$ and i can be written in a matrix form as

$$\begin{bmatrix} \dot{\mathbf{r}}_i \\ \dot{\omega}_i \end{bmatrix} = \begin{bmatrix} \mathbf{A}_{i,i-1} & \mathbf{A}_{i,i-1} \mathbf{d}_{i,i-1}^\perp \\ \mathbf{0} & 1 \end{bmatrix} \begin{bmatrix} \dot{\mathbf{r}}_{i-1} \\ \dot{\omega}_{i-1} \end{bmatrix} + \begin{bmatrix} 0 & 0 \\ 1 & 0 \\ 0 & 1 \end{bmatrix} \begin{bmatrix} \dot{\tau}_i \\ \dot{\phi}_i \end{bmatrix} \quad (14)$$

or written in symbolic form,

$$\dot{\mathbf{z}}_i = \mathbf{E}_{i,i-1} \dot{\mathbf{z}}_{i-1} + \mathbf{B}_i \dot{\mathbf{q}}_i \quad (15)$$

where

$$\dot{\mathbf{z}}_i = \begin{bmatrix} \dot{\mathbf{r}}_i \\ \dot{\omega}_i \end{bmatrix} \quad (16)$$

$$\mathbf{E}_{i,i-1} = \begin{bmatrix} \mathbf{A}_{i,i-1} & \mathbf{A}_{i,i-1} \mathbf{d}_{i,i-1}^\perp \\ \mathbf{0} & 1 \end{bmatrix} \quad (17)$$

$$\mathbf{B}_i = \begin{bmatrix} 0 & 0 \\ 1 & 0 \\ 0 & 1 \end{bmatrix} \quad (18)$$

The angular acceleration of body i is obtained by taking a time derivation of equation 8,

$$\dot{\omega}_i = \dot{\omega}_{i-1} + \ddot{\phi}_i \quad (19)$$

The translational acceleration of body i is obtained by taking the time derivative of equation 11,

$$\ddot{\mathbf{r}}_i^* = \ddot{\mathbf{r}}_{i-1}^* + \dot{\omega}_{i-1} \mathbf{d}_{i,i-1}^{\perp*} + \omega_{i-1} \dot{\mathbf{d}}_{i,i-1}^{\perp*} + \omega_i \mathbf{u}_i^{\perp*} \dot{\tau}_i + \mathbf{u}_i^* \ddot{\tau}_i \quad (20)$$

Substituting for $\dot{\mathbf{d}}_{i,i-1}^*$ from equation 10 into equation 20,

$$\ddot{\mathbf{r}}_i^* = \ddot{\mathbf{r}}_{i-1}^* + \omega_{i-1} \dot{\mathbf{d}}_{i,i-1}^{\perp*} - \omega_{i-1} \omega_{i-1} \mathbf{d}_{i,i-1}^* + \omega_{i-1} \mathbf{u}_i^{\perp*} \dot{\tau}_i + \omega_i \mathbf{u}_i^{\perp*} \dot{\tau}_i + \mathbf{u}_i^* \ddot{\tau}_i \quad (21)$$

Substituting for ω_{i-1} from equation 8 into equation 21,

$$\ddot{\mathbf{r}}_i^* = \ddot{\mathbf{r}}_{i-1}^* + \omega_{i-1} \dot{\mathbf{d}}_{i,i-1}^{\perp*} - \omega_{i-1} \omega_{i-1} \mathbf{d}_{i,i-1}^* + 2\omega_i \mathbf{u}_i^{\perp*} \dot{\tau}_i + \mathbf{u}_i^* \ddot{\tau}_i \quad (22)$$

Define

$$\ddot{\mathbf{r}}_i^* = \mathbf{A}_i \ddot{\mathbf{r}}_i \quad (23)$$

Using the relative orientation matrix $\mathbf{A}_{i,i-1}$, and equation 23, the globally defined translational acceleration in equation 22 can be converted into the local translational acceleration in each local link coordinate as,

$$\ddot{\mathbf{r}}_i = \mathbf{A}_{i,i-1} \ddot{\mathbf{r}}_{i-1} + \dot{\omega}_{i-1} \mathbf{A}_{i,i-1} \mathbf{d}_{i,i-1}^\perp - \omega_{i-1} \dot{\omega}_{i-1} \mathbf{A}_{i,i-1} \mathbf{d}_{i,i-1} + 2\omega_i \mathbf{u}_i^\perp \dot{\tau}_i + \mathbf{u}_i \ddot{\tau}_i \quad (24)$$

Similar to the velocity recursion, equations 19 and 24 are combined in a matrix form as,

$$\begin{aligned} \begin{bmatrix} \ddot{\mathbf{r}}_i \\ \dot{\omega}_i \end{bmatrix} &= \begin{bmatrix} \mathbf{A}_{i,i-1} & \mathbf{A}_{i,i-1} \mathbf{d}_{i,i-1}^\perp \\ \mathbf{0} & 1 \end{bmatrix} \begin{bmatrix} \ddot{\mathbf{r}}_{i-1} \\ \dot{\omega}_{i-1} \end{bmatrix} + \begin{bmatrix} 0 & 0 \\ 1 & 0 \\ 0 & 1 \end{bmatrix} \begin{bmatrix} \dot{\tau}_i \\ \ddot{\phi}_i \end{bmatrix} \\ &+ \begin{bmatrix} -\omega_{i-1} \dot{\omega}_{i-1} \mathbf{A}_{i,i-1} \mathbf{d}_{i,i-1} + 2\omega_i \mathbf{u}_{i,i-1}^\perp \dot{\tau}_i \\ 0 \end{bmatrix} \end{aligned} \quad (25)$$

or written in symbolic form,

$$\ddot{\mathbf{z}}_i = \mathbf{E}_{i,i-1} \ddot{\mathbf{z}}_{i-1} + \mathbf{B}_i \ddot{\mathbf{q}}_i + \mathbf{R}_i \quad (26)$$

where

$$\ddot{\mathbf{z}}_i = \begin{bmatrix} \ddot{\mathbf{r}}_i \\ \dot{\omega}_i \end{bmatrix} \quad (27)$$

$$\mathbf{R}_i = \begin{bmatrix} -\omega_{i-1} \dot{\omega}_{i-1} \mathbf{A}_{i,i-1} \mathbf{d}_{i,i-1} + 2\omega_i \mathbf{u}_{i,i-1}^\perp \dot{\tau}_i \\ 0 \end{bmatrix} \quad (28)$$

Using equation 15, the virtual displacements recursion of the two bodies i and $i-1$ can be represented in matrix form as

$$\delta \mathbf{z}_i = \mathbf{E}_{i,i-1} \delta \mathbf{z}_{i-1} + \mathbf{B}_i \delta \mathbf{q}_i \quad (29)$$

where

$$\delta \mathbf{z}_i = \begin{bmatrix} \delta \mathbf{r}_i \\ \delta \theta_i \end{bmatrix} \quad (30)$$

where $\delta \theta_i$ is the virtual rotation of body i .

Recursive Dynamics

Consider a rigid body, shown in Figure 2-4, located in a plane by a position vector \mathbf{r}_i and a set of generalized coordinates that define the orientation of the local joint reference frame relative to the inertial reference frame. A differential mass $dm(P)$ at a typical point is located on the body vector \mathbf{s}_i .

The variational Newton-Euler equations of motion of a rigid body in the local joint reference frame is

$$\begin{aligned} & \delta \mathbf{r}_i^T \left\{ \ddot{\mathbf{r}}_i \int_m dm(P) + \delta \mathbf{r}_i^T (\mathbf{A}_i^T \mathbf{B}_i \ddot{\theta}_i - \dot{\theta}_i^2) \int_m \mathbf{s}_i dm(P) \right\} \\ & + \delta \theta_i^T \left\{ \ddot{\mathbf{r}}_i^T \mathbf{A}_i^T \mathbf{B}_i \int_m \mathbf{s}_i dm(P) + \ddot{\theta}_i \int_m \mathbf{s}_i^T \mathbf{s}_i dm(P) - \dot{\theta}_i \int_m \mathbf{s}_i^T \mathbf{B}_i^T \mathbf{A}_i \mathbf{s}_i dm(P) \right\} \\ & = \delta \mathbf{r}_i^T \int_m \mathbf{F}_i(P) dm(P) - \delta \theta_i^T \int_m \mathbf{s}_i^T \mathbf{B}_i^T \mathbf{A}_i \mathbf{F}_i(P) dm(P) \end{aligned} \quad (31)$$

for all $\delta \mathbf{r}_i$ and $\delta \theta_i$ that are consistent with constraints.

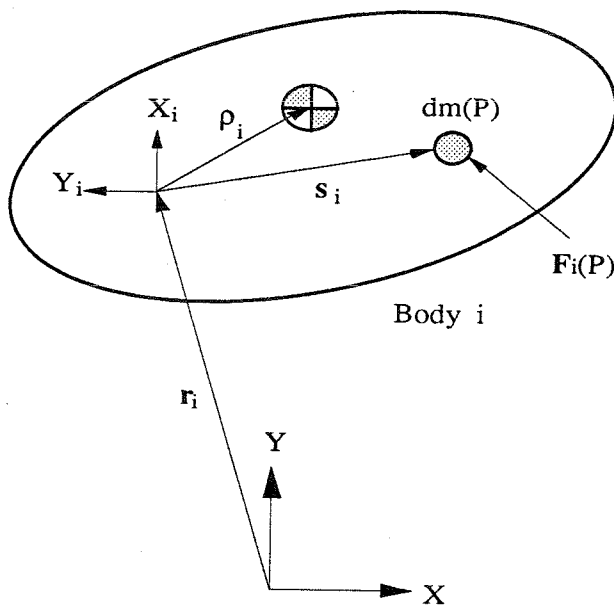


Figure 2-4
A Rigid Body in a Plane

Let a body-fixed reference frame be selected with its origin at the center of the joint reference frame (i.e., noncentroidal reference frame).

The total mass is

$$m_i = \int_m dm(p) \quad (32)$$

From the definition of the location of the center of mass of the i th body as

$$m_i \rho_i = \int_m \mathbf{s}_i dm(P) \quad (33)$$

The fourth integral in equation 31 may be written as

$$\mathbf{J}_i \equiv \int_m \mathbf{s}_i^T \mathbf{s}_i dm(P) \quad (34)$$

Note that \mathbf{J}_i is the moment of inertia of body i , relative to the noncentroidal joint reference frame.

Direct computation of the fifth integrand may be expressed as

$$\int_m \mathbf{s}_i^T \mathbf{B}_i^T \mathbf{A}_i \mathbf{s}_i dm(P) = 0 \quad (35)$$

where

$$\mathbf{B}_i^T \mathbf{A}_i = \begin{bmatrix} 0 & 1 \\ -1 & 0 \end{bmatrix}$$

The total external force acting on the body is

$$\mathbf{f}_i = \int_m \mathbf{F}_i(P) dm(P) \quad (36)$$

and the moment of the external forces with respect to the origin of the body reference frame is

$$\mathbf{n}_i \equiv \int_m \mathbf{s}_i^{\perp T} \mathbf{F}_i(P) dm(P) \quad (37)$$

where

$$\mathbf{s}_i^{\perp} = \mathbf{A}_i^T \mathbf{B}_i \mathbf{s}_i$$

Substituting equations 32 through 37 into equation 31 yields the variational Newton-Euler equations of motion for a rigid body with a noncentroidal joint fixed reference frame,

$$\delta \mathbf{r}_i^T (m_i \ddot{\mathbf{r}}_i + m_i \rho_i^{\perp} \ddot{\theta}_i - m_i \rho_i \dot{\theta}_i^2) + \delta \theta_i^T (m_i \rho_i^{\perp T} \ddot{\mathbf{r}}_i + \mathbf{J}_i \ddot{\theta}_i) = \delta \mathbf{r}_i^T \mathbf{f}_i + \delta \theta_i^T \mathbf{s}_i^{\perp T} \mathbf{n}_i \quad (38)$$

where

$$\rho_i^{\perp} = \mathbf{A}_i^T \mathbf{B}_i \rho_i$$

Rewriting equation 38 in a matrix form,

$$\delta \mathbf{z}_i^T (\mathbf{M}_i \ddot{\mathbf{z}}_i - \mathbf{Q}_i) = 0 \quad (39)$$

where

$$\mathbf{M}_i = \begin{bmatrix} m_i \mathbf{I} & -m_i \rho_i^{\perp} \\ m_i \rho_i & \mathbf{J}_i \end{bmatrix} \quad (40)$$

$$\mathbf{Q}_i = \begin{bmatrix} \mathbf{f}_i \\ \mathbf{n}_i \end{bmatrix} - \begin{bmatrix} m_i \rho_i \dot{\theta}_i^2 \\ 0 \end{bmatrix} \quad (41)$$

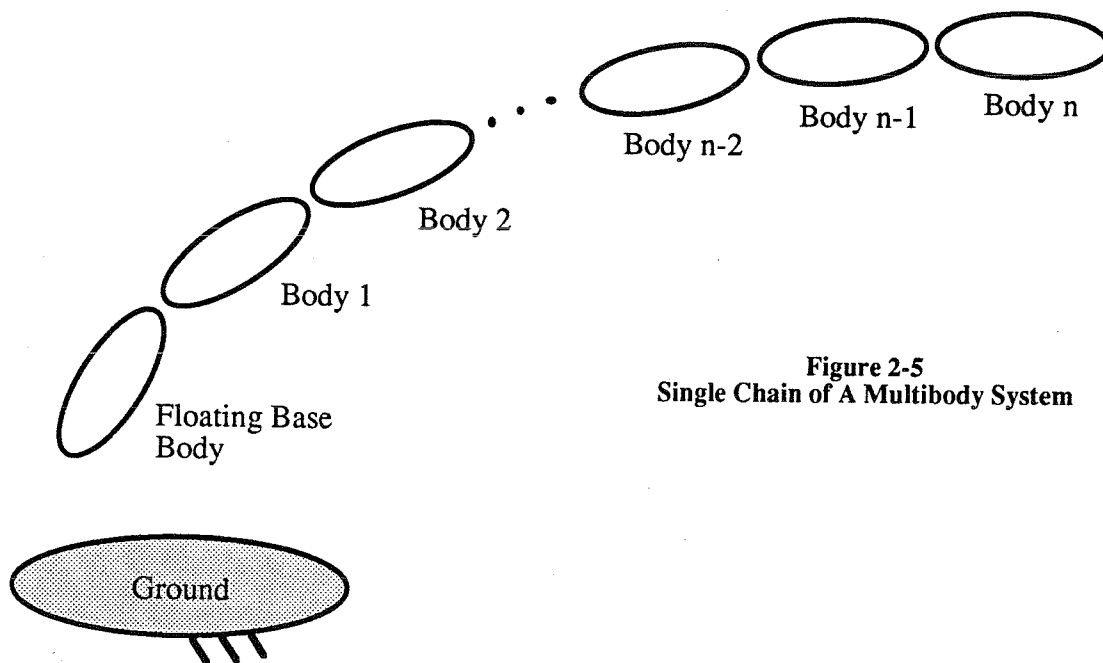


Figure 2-5
Single Chain of A Multibody System

The variational form of Newton-Euler equations of motion of a single chain containing n joints and $n+1$ bodies, as shown in Figure 2-5, is presented next. The equations of motion of the multibody system are

$$\sum_{i=0}^n \delta z_i^T (M_i \ddot{z}_i - Q_i) = 0 \quad (42)$$

which must hold for all kinematically admissible variational δz_i , $i=0, 1, 2, \dots, n$ (i.e., for all that satisfy kinematic constraints between bodies).

Using the kinematic recurrence relations of equations 26 and 29, differential equations of motion for a single chain will be constructed in a backward path sequence.

The virtual displacement δz_i of body i can be represented in terms of its inboard variation of relative generalized coordinates from equation 29 as

$$\delta z_i = E_{i,0} \delta z_0 + \sum_{j=1}^i E_{i,j} B_j \delta q_j \quad (43)$$

Note that the virtual displacement δz_i of the base body can be represented as $\delta z_0 = B_0 \delta q_0$, because the virtual displacement of a ground-fixed body is always zero. Therefore, equation 42 can have a simpler form as

$$\delta z_i = \sum_{j=0}^i E_{i,j} B_j \delta q_j \quad (44)$$

Substituting for δz_i from equation 44 into equation 42 and rewriting in an expanded form as,

$$\begin{aligned}
& \delta q_0^T \mathbf{B}_0^T (\mathbf{M}_0 \ddot{\mathbf{z}}_0 - \mathbf{Q}_0) \\
& + \sum_{i=0}^1 \delta q_i^T \mathbf{B}_i^T \mathbf{E}_{1,j}^T (\mathbf{M}_1 \ddot{\mathbf{z}}_1 - \mathbf{Q}_1) \\
& + \sum_{i=0}^2 \delta q_i^T \mathbf{B}_i^T \mathbf{E}_{2,j}^T (\mathbf{M}_2 \ddot{\mathbf{z}}_2 - \mathbf{Q}_2) \\
& \vdots \\
& + \sum_{i=0}^n \delta q_i^T \mathbf{B}_i^T \mathbf{E}_{n,j}^T (\mathbf{M}_n \ddot{\mathbf{z}}_n - \mathbf{Q}_n) \\
& = \sum_{i=0}^n \delta q_i^T \mathbf{B}_i^T \left\{ \sum_{j=i}^n \mathbf{E}_{j,i}^T (\mathbf{M}_j \ddot{\mathbf{z}}_j - \mathbf{Q}_j) \right\} = 0 \tag{45}
\end{aligned}$$

Since the variations of relative joint coordinates are arbitrary, each coefficient of δq_i must vanish, i.e.,

$$\mathbf{B}_i^T \sum_{j=i}^n \mathbf{E}_{j,i}^T (\mathbf{M}_j \ddot{\mathbf{z}}_j - \mathbf{Q}_j) = 0, \quad i = 0, 1, 2, \dots, n \tag{46}$$

Substituting for $\ddot{\mathbf{z}}_n$ from equation 26 into equation 46,

$$\mathbf{B}_i^T \left(\sum_{j=i}^{n-1} \mathbf{E}_{j,i}^T (\mathbf{M}_j \ddot{\mathbf{z}}_j - \mathbf{Q}_j) + \mathbf{E}_{n,i}^T (\mathbf{K}_n \mathbf{E}_{n,n-1} \ddot{\mathbf{z}}_{n-1} + \mathbf{K}_n \mathbf{B}_n \ddot{\mathbf{q}}_n - \mathbf{F}_n) \right) = \mathbf{0} \tag{47}$$

where $i=1, 2, \dots, n$ and

$$\mathbf{K}_n = \mathbf{M}_n \tag{48}$$

$$\mathbf{F}_n = \mathbf{Q}_n - \mathbf{K}_n \mathbf{R}_n \tag{49}$$

Rearranging equation 47 and substituting for $\ddot{\mathbf{z}}_{n-1}$ from equation 26 into equation 47,

$$\mathbf{B}_i^T \left\{ \sum_{j=i}^{n-2} \mathbf{E}_{j,i}^T (\mathbf{M}_j \ddot{\mathbf{z}}_j - \mathbf{Q}_j) + \mathbf{E}_{n-1,i}^T (\mathbf{K}_{n-1} \mathbf{E}_{n-1,n-2} \ddot{\mathbf{z}}_{n-2} + \mathbf{K}_{n-1} \mathbf{B}_{n-1} \ddot{\mathbf{q}}_{n-1} + \mathbf{E}_{n,n-1}^T \mathbf{K}_n \mathbf{B}_n \ddot{\mathbf{q}}_n - \mathbf{E}_{n-1,n-2}^T \mathbf{F}_{n-1}) \right\} = \mathbf{0} \quad (50)$$

where $i = 1, 2, \dots, n$ and

$$\mathbf{K}_{n-1} = \mathbf{M}_{n-1} + \mathbf{E}_{n,n-1}^T \mathbf{K}_n \mathbf{E}_{n,n-1} \quad (51)$$

$$\mathbf{F}_{n-1} = \mathbf{Q}_{n-1} - \mathbf{K}_{n-1} \mathbf{R}_{n-1} + \mathbf{E}_{n,n-1}^T \mathbf{F}_n \quad (52)$$

Repeating the backward substitutions and additions to the body i ,

$$\mathbf{B}_i^T \left(\mathbf{K}_i \ddot{\mathbf{z}}_i - \mathbf{F}_i - \mathbf{K}_i \mathbf{R}_i + \sum_{j=i+1}^n \mathbf{E}_{j,i}^T \mathbf{K}_j \mathbf{B}_j \ddot{\mathbf{q}}_j \right) = \mathbf{0} \quad (53)$$

where $i = 1, 2, \dots, n$ and

$$\mathbf{K}_i = \mathbf{M}_i + \mathbf{E}_{i+1,i}^T \mathbf{K}_{i+1} \mathbf{E}_{i+1,i} \quad (54)$$

$$\mathbf{F}_i = \mathbf{Q}_i - \mathbf{K}_i \mathbf{R}_i + \mathbf{E}_{i+1,i}^T \mathbf{F}_{i+1} \quad (55)$$

Using the recursive acceleration relations derived in equation 26, the result of sequential backward substitution from $\ddot{\mathbf{z}}_i$ to $\ddot{\mathbf{z}}_0$ is

$$\begin{aligned}
\ddot{\mathbf{z}}_i &= \mathbf{E}_{i,i-1}\ddot{\mathbf{z}}_{i-1} + \mathbf{B}_i\ddot{\mathbf{q}}_i + \mathbf{R}_i \\
&= \mathbf{E}_{i,i-2}\ddot{\mathbf{z}}_{i-2} + \mathbf{E}_{i,i-1}\mathbf{B}_{i-1}\ddot{\mathbf{q}}_{i-1} + \mathbf{B}_i\ddot{\mathbf{q}}_i + \mathbf{E}_{i,i-1}\mathbf{R}_{i-1} + \mathbf{R}_i \\
&\vdots \\
&= \mathbf{E}_{i,0}\ddot{\mathbf{z}}_0 + \sum_{j=1}^i \mathbf{E}_{i,j}(\mathbf{B}_j\ddot{\mathbf{q}}_j + \mathbf{R}_j) \\
&= \sum_{j=0}^i \mathbf{E}_{i,j}(\mathbf{B}_j\ddot{\mathbf{q}}_j + \mathbf{R}_j) \tag{56}
\end{aligned}$$

Substituting equation 56 into equation 53,

$$\mathbf{B}_i^T \left(\mathbf{K}_i \sum_{j=0}^i \mathbf{E}_{i,j} \mathbf{B}_j \ddot{\mathbf{q}}_j + \sum_{j=i+1}^n \mathbf{E}_{j,i}^T \mathbf{K}_j \mathbf{B}_j \ddot{\mathbf{q}}_j \right) = \mathbf{B}_i^T \left(\mathbf{F}_i - \mathbf{K}_i \sum_{j=0}^{i-1} \mathbf{E}_{i,j} \mathbf{R}_j \right) \tag{57}$$

where $i = 1, 2, \dots, n$

Truck Subsystem Models

A modular approach for model development of a full vehicle dynamic system by using subsystems enhances the user-friendliness and modeling flexibility, and simplifies model validation. This section describes the characteristics of vehicle subsystem models.

Spring Models

Suspension force elements are, in general, modeled as compliant connections between two bodies to provide a cushion between them. Generalized force computation for such compliant elements is required in Cartesian force terms of $\mathbf{g}_i^T = [\mathbf{f}_i^T, \mathbf{n}_i^T]^T$ as shown in equation 41. Typical models for coupling elements are linear springs and dampers that can be arranged in parallel or in series. The force law may be rather complex, described by nonlinear characteristics or differential equations. The mathematical models of spring damper force, leaf spring force, and air bag spring force are explained in this section.

Translational Spring Damper Force Model

This force element exerts equal and opposite forces on bodies i and j at point p_i and p_j , respectively, as shown in Figure 2-6. The force due to this element can be derived from direct use of the virtual work definition of generalized force. Defining tension in the compliant element as positive, the force acting in the element is written as

$$\mathbf{f}_t = k(l_0 - l) + c\dot{l} + F(l, \dot{l}, t) \tag{58}$$

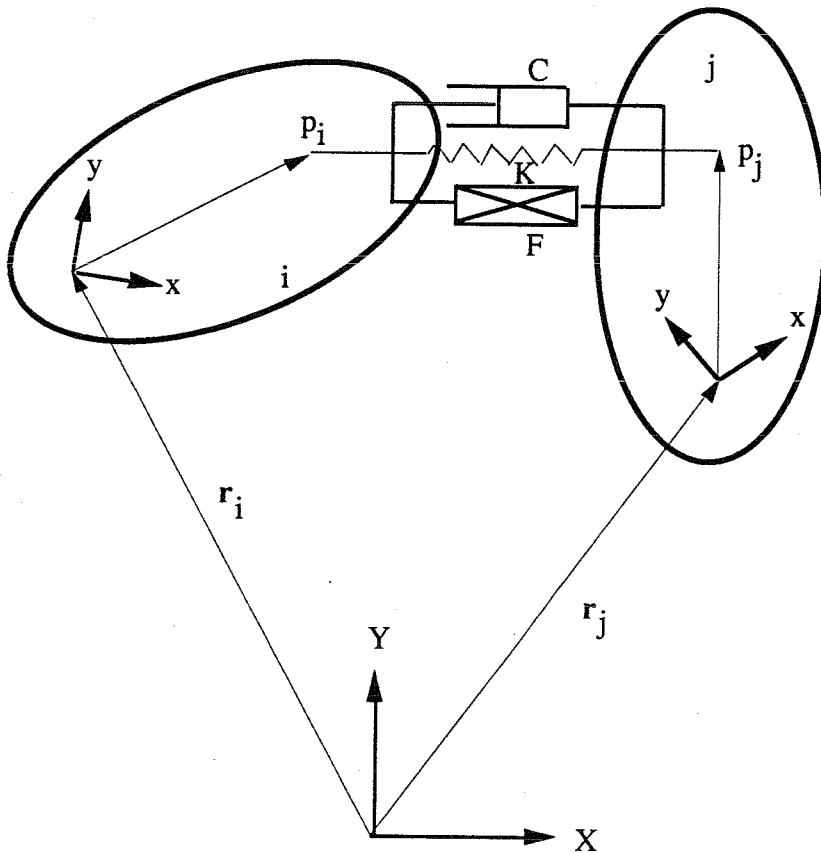


Figure 2-6
Translational Spring-Damper-Actuator Model

where k is the spring coefficient, l_0 is the free length of the spring, c is the damping coefficient, and F is a general actuator force that may depend on l , \dot{l} , or time t .

The Cartesian generalized force vector for each body can be written as

$$\mathbf{g}_i = -f_t \begin{bmatrix} \mathbf{u}_i \\ \mathbf{s}_i^{\perp T} \mathbf{u}_i \end{bmatrix} \quad (59)$$

$$\mathbf{g}_j = f_t \begin{bmatrix} \mathbf{u}_j \\ \mathbf{s}_j^{\perp T} \mathbf{u}_j \end{bmatrix} \quad (60)$$

where \mathbf{s}_i and \mathbf{s}_j are the position vectors to the point p_i and p_j in each joint-fixed reference frame. Detailed derivation of this element is given in Haug (1989).

Rotational Spring-Damper Force Model

The compliant element exerts torques of equal magnitude but opposite orientation on bodies i and j as shown in Figure 2-7 and is called a rotational spring-damper force model. A positive torque is one that acts counterclockwise on body i and clockwise on body j . The torque that acts between the bodies is

$$n = k_\theta(\theta_{ij} - \theta_0) + c_\theta \dot{\theta}_{ij} + N(\theta_{ij}, \dot{\theta}_{ij}, t) \quad (61)$$

where θ_{ij} is the current spring angle, θ_0 is the free angle of the spring, k_θ is the torsional spring coefficient, and c_θ is a torsional damping coefficient. N is a general actuator torque. If the revolute joint axis is defined by a unit vector \mathbf{u} , the Cartesian force for each body can be written as

$$\mathbf{g}_i = -n \begin{bmatrix} \mathbf{0} \\ \mathbf{u} \end{bmatrix} \quad (62)$$

$$\mathbf{g}_j = n \begin{bmatrix} \mathbf{0} \\ \mathbf{u} \end{bmatrix} \quad (63)$$

Leaf Spring Force Model

This model is a nonlinear spring damper element. The leaf spring is a highly nonlinear force/displacement device. Much of the complexity derives from the ability of the leaf spring to store and dissipate energy. Because of this hysteretic behavior of the leaf spring, representation of the spring rate and friction level as a constant or even as a single nonlinear curve is not valid for the dynamic load condition. An extensive study (MacAdam et al., 1980) of this behavior has yielded an equation to describe such force based on experimental data as follows:

$$f_i = f_{ENV_j} + (f_{i-1} - f_{ENV_j}) e^{-|\frac{\delta_i - \delta_{i-1}}{\beta_j}|} \quad (64)$$

using the following definitions:

- f_i suspension force at the current simulation time step
- f_{i-1} suspension force at the previous simulation time step
- δ_i suspension deflection at the current simulation time step
- δ_{i-1} suspension deflection at the previous simulation time step
- f_{ENV_j} force corresponding to the upper and lower boundaries of the envelope of the measured spring characteristics at the deflection, d_j . Subscript j indicates upper and lower boundaries
- β_j an input parameter used for describing the rate at which the suspension force within a hysteresis loop approaches the outer boundary of the envelope, f_{ENV_j}

For use in digital simulation, the upper and lower boundaries of the envelope of spring characteristics are entered into the computer code as function or table of spring

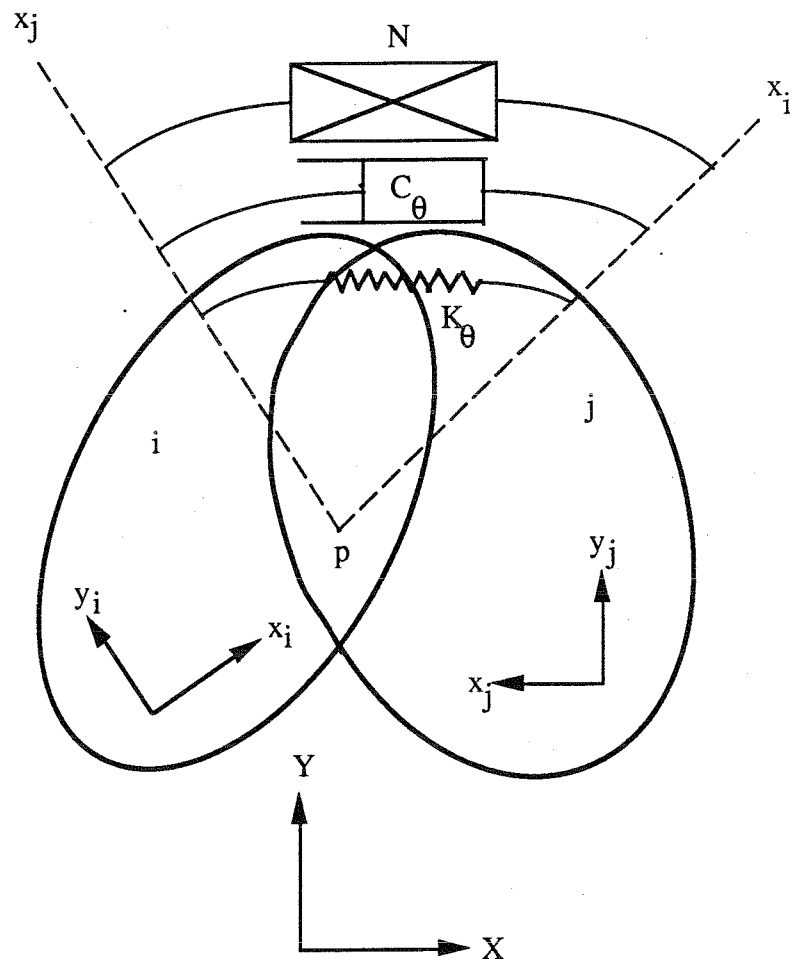


Figure 2-7
Rotational Spring-Damper-Actuator Model

deflection. These envelopes are then computed by cubic spline interpolation based on given data.

Once force f_i is computed, the computation of Cartesian force vector due to spring force for each body is the same as in the case of translational spring damper force model as shown in equations 59 and 60.

Air Bag Spring

The air bag spring is a nonlinear force model similar to the leaf spring model. The behavior of the entire suspension system can be described as two independent thermodynamic processes: a reversible polytropic constant mass process and a constant temperature process. The air bag spring force model is divided into two submodels: the air spring and the air delivery system. Detailed derivation of the air spring model is referred to in MacAdam et al. (1980).

Final equation of the change of spring vertical force is as follows:

$$f_i = f_{i-1} + A_L \Delta P_i - K_p \delta_i \quad (65)$$

where

$$\Delta P_i \equiv P_i - P_{i-1} = \left[P_a \left(\frac{V_0}{V_0 + A_V \delta_i} \right)^{1.38} - P_a \right] \quad (66)$$

using the following definitions:

- f_i suspension vertical force at the current simulation time step
- f_{i-1} suspension vertical force at the previous simulation time step
- d_i suspension deflection at the current simulation time step
- V_0 nominal air spring internal volume at operating point
- P_0 nominal air spring gauge pressure at the operating point
- P_a air spring absolute pressure
- A_L effective air spring area with respect to load
- A_V effective air spring area with respect to volume
- K_p air spring constant pressure spring rate

Note that operating point data such as V_0 and P_0 is assumed identical to static conditions. The values A_v , A_L , and K_p are determined from lookup table data, in turn based on the operating point data.

The air delivery system is designed to force air into or out of the air spring via the height regulator or through its interconnections with the tandem air suspension. Air flow through the height regulators is typically quite slow, but can have a significant load leveling effect which can be shown as

$$\Delta P_D = \frac{1}{V_{AV}} \left[\sum_{i=1}^n C_i (P_{ei} - P_{AV}) - (P_{AV} + P_{at}) \left(\frac{dV}{dt} \right)_{AV} \right] \Delta t \quad (67)$$

where subscript AV and D indicate an average value over the time step and “of the delivery system,” respectively, using the following definitions:

- C_i constant property of the flow path i
- P_{ei} gauge air pressure at the opposite end of flow path i
- P_{at} atmospheric pressure

By comparison with ΔP_i shown in equation 66, ΔP_D in equation 67 (the change in pressure due to the delivery system) will be very small for any given time step. The more important impact of this system will be its accumulative effect over a long period of time. Therefore, the total air spring pressure change may be written as $\Delta P_T = \Delta P_i + \Delta P_D$ and used in equation 65 instead of ΔP_i .

Once force f_i is computed, the computation of the Cartesian force vector due to air spring force for each body is the same as in the case of the translational spring damper force model as shown in equations 59 and 60.

Tire/Road Models

Because the motion of the vehicle is almost entirely dependent on force and moments applied to the vehicle from the road, the representation of the tire-road interface is of great importance in any realistic vehicle simulation. Computation of Cartesian force at the tire-road interface in pitch plane simulation is relatively simple compared to a three-dimensional steering simulation. In a pitch plane model, the tire force can be subdivided into three components: vertical force, longitudinal force, and rolling resistance torque.

The vertical force is due to the tire compression or ground penetration. The vertical force depends on the amount of tire compression. The bottom of the tire is located globally and a test is made to determine whether the point is below the road surface or not. If it is below the road surface, a vertical force is calculated and added to the tire force terms.

The longitudinal force is due to tire longitudinal slip, rolling resistance, and road obstructions. Longitudinal tire forces can be developed due to longitudinal slip created during acceleration or braking. Longitudinal force is equal to the torque divided by the radius (when this ratio is less than or equal to μ) times the normal load where the slip ratio μ is calculated from wheel spin dynamics.

The rolling resistance torque is due to these forces acting through distances from where they are applied, assuming the tire center is taken as the center of the local reference frame.

The purpose in tire/road modeling is to compute these forces and torque at the tire-road interface to the tire-road kinematics. There are several types of tire models depending on the vehicle maneuvers and road profiles: point follower model, fixed footprint model, and radial spring model. Also, if wheel rotation is to be considered, wheel spin dynamic equations

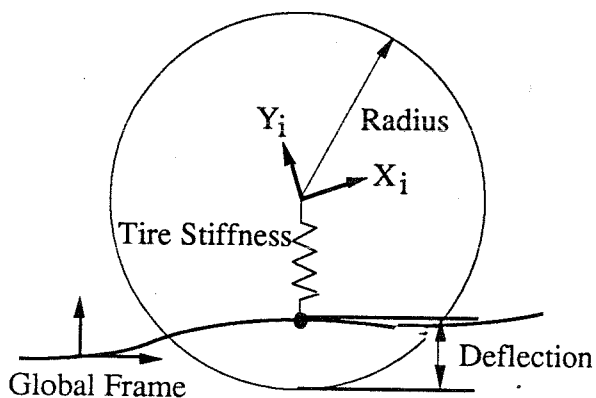


Figure 2-8
Point Follower Tire Model

should be included to decide the longitudinal forces between the tire and the road, especially for braking or loss of traction conditions.

Point Follower Tire Model

The point follower tire model, shown in Figure 2-8, is a simple but very effective model for a smooth road profile or for modeling vertical forces on a fault and smooth road profile. The tire is modeled as a spring and damper element.

The model can be improved by representing the force as a nonlinear function of tire penetration. Note that no longitudinal force is present in this model.

The Cartesian force vector calculated from the tire contact patch forces and moment is added to the generalized force.

Radial Spring Tire Model

This model computes the amount of interference between the tire and road at several points around the perimeter of the tire. This method is referred to as the radial spring tire model and is shown in Figure 2-9.

Tire forces are found by summing penetration and damping forces around the tire. This method requires an iterative method to solve for penetration depth. An outline of this method is referred to by Kading and Vanderploeg (1985).

The Cartesian force vector calculated from the tire contact patch forces and moment is added to the generalized force.

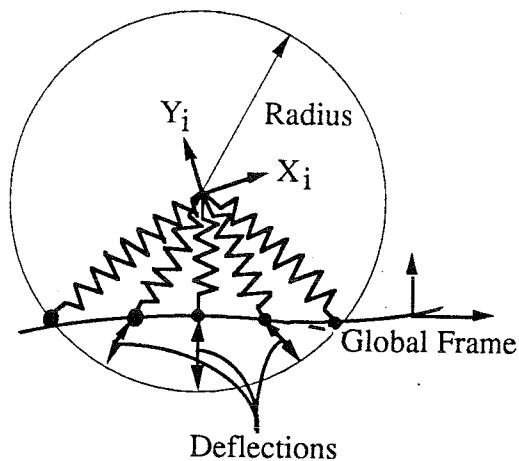


Figure 2-9
Radial Spring Tire Model

Suspension Models

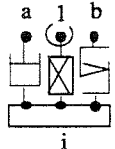
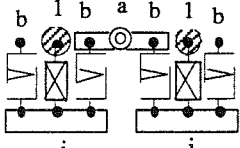
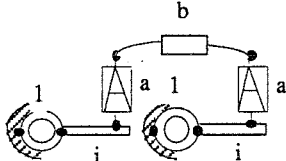

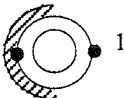
Vehicle suspensions are composed of several moving linkages, a wheel assembly, and compliant elements such as springs and dampers. Typical suspension types for an over-the-road truck are air bags, leaf springs, and a walking beam.

Multibody suspension modeling starts by identifying the connectivity of suspension components. Suspension links connect wheel and axle assemblies and the chassis by kinematic joints.

To enhance user-friendliness, a suspension is developed as a predefined model. This model is interpreted as a suspension subsystem composed of a set of links, instead of defining individual links separately. This will allow analysts to define suspension geometry in terms of vehicle data from chassis and suspension layout drawings.

Since topological data for each suspension type are invariant, it is possible to create a suspension library for a variety of suspension types, as shown in Table 2-1.

Table 2-1
Library of Truck Subsystem Models

Type of Subsystem	Model Configuration	Body and Joint Models	Force Models
Single Leaf Spring Suspension		i: Axle 1: Translational Joint	a: Translational Damper b: Leaf Spring
Four Leaf Spring Suspension		i: Axle 1: Translational Joint	a: Load Leveling System b: Leaf Spring
Four Air Bag Spring Suspension		i: Axle 1: Revolute Joint	a: Air Bag Spring b: Air Pressure Delivery System
Tire Model		—	a: Translational Spring Damper System
Hitch Model (Fifth Wheel and Dolly)		1: Revolute Joint	—

Structure of Truck Simulation Program

The structure of the truck simulation program, as shown in Figure 2-10, includes a preprocessor that accumulates vehicle input data from vehicle subsystem models. It also determines the solution scheme of multibody dynamic analysis. Finally, it defines the form of the dynamic performance measure as a postprocessing procedure, and the format of the input data for pavement analysis.

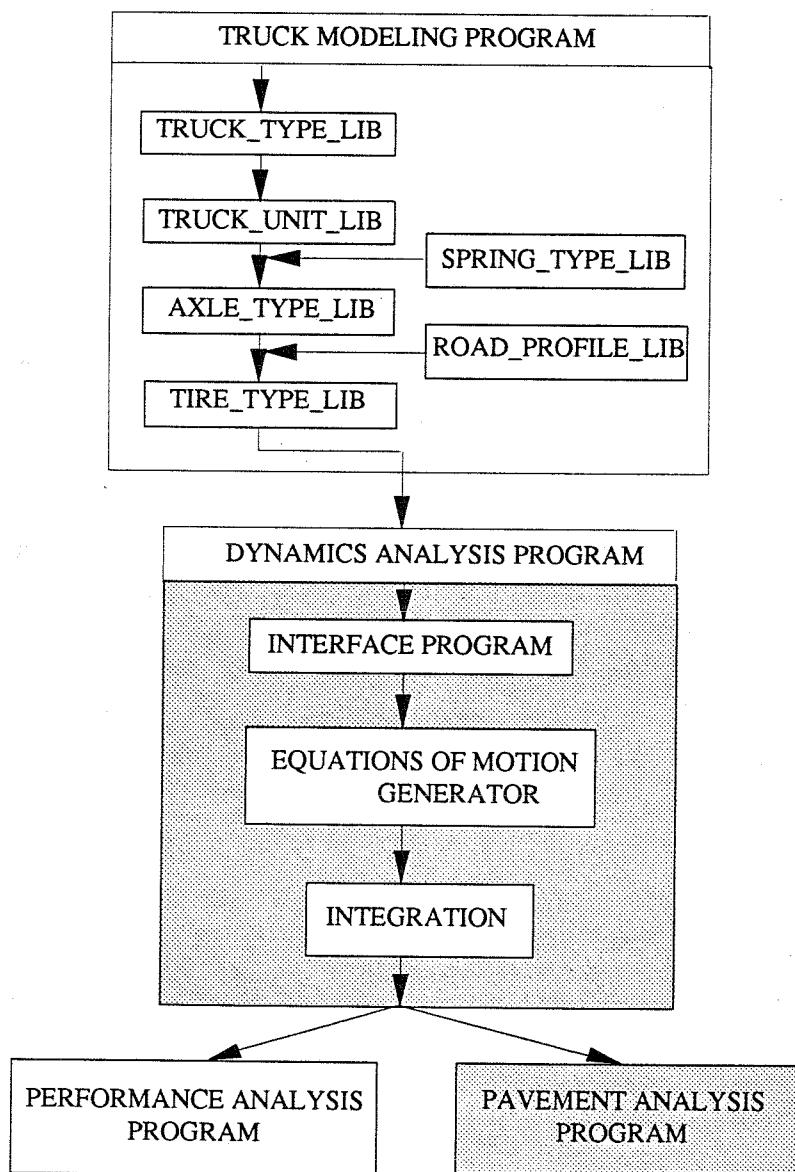


Figure 2-10
Structure of Truck Simulation Program

Truck Modeling Program

This program is written in a general fashion to accommodate a wide range of truck configurations. Initially, fundamental geometric and inertia data requirements and formats are established for easy use by those familiar with truck-oriented terminologies. Provision is made for parametric variation of suspension characteristics, axle configuration, axle spacing, wheelbase, fifth wheel position, and payload distribution.

Table 2-2 presents a list of libraries of truck types, truck units, and subsystems supported in this study. An extensive database of the libraries for use with the simulation is on file. Included in this database are values for suspension parameters, tires, and damping characteristics. The data flow of the truck modeling program as shown in Figure 2-10 is described as follows:

1. The type of truck is selected from TRUCK_TYPE_LIB shown in Table 2-2, and each unit of the truck and their couplings (e.g., fifth wheel) are selected from TRUCK_UNIT_LIB as shown in Table 2-2. Topological analysis using a graph theoretic method (Christofieds, 1986), determines the kinematic assembly of the truck units.
2. Suspension types are selected from the suspension library. First, the axle types are selected from AXLE_TYPE_LIB, as shown in Table 2-2. Then, spring types are

selected from SPRING_TYPE_LIB for each suspension type. Topological analysis is used to determine the kinematic assembly of the full truck model resulting from the selection from the suspension modeling library.

3. Tires are selected for each axle from TIRE_TYPE_LIB as shown in Table 2-2. The road profile for the simulation environment is selected from ROAD_TYPE_LIB.

**Table 2-2
Truck Subsystem Library and Parameters Considered**

Subsystems	Names	Types	Parameters
Trucks	TRUCK_TYPE_LIB	Straight Truck Tractor and Semitrailer Double Triple	Fifth Wheel Location Hitch Height and Locations
Truck Units	TRUCK_UNIT_LIB	Tractor: T2, T3, T4 Semitrailer: S1, S2, S3 Dolly: D1, D2	Mass and Inertia Geometric Characteristics
Axle Configuration	AXLE_TYPE_LIB	Single Axle Double Axle Tridem Axle	Axle Spacing Mass and Inertia Load Leveling Parameters
Spring Damper Types	SPRING_TYPE_LIB	Leaf Spring Air Bag Spring TSDA and RSDA*	Spring and Damping Characteristics
Tire Types	TIRE_TYPE_LIB	Single Dual	Spring and Damping Characteristics
Road Types	ROAD_PROFILE_LIB	Random Road Jointed Road	Height of Fault Slab Length of Warping
Suspension Types	SUS_TYPE_LIB	Single Leaf Spring Tandem Leaf Spring Tridem Leaf Spring Tandem Air Spring Tridem Air Spring	Combination of Axle Configurations and Spring Types

* Translational Spring-Damper and Actuator model, and Rotational Spring-Damper and Actuator model .

Dynamic Analysis Program

An interface program receives fundamental vehicle data from the truck modeling program and transforms it to parameters that are suitable for implementing the Dynamic Analysis Program.

This program automatically generates equations of motion in the form of a broadly applicable general purpose multibody system model, using the previously described recursive formulation. The computational flow of the dynamic analysis program is as follows:

1. Compute distance vector $\mathbf{d}_{i,j-1}$ from equation 4.
2. Compute relative transformation matrix $\mathbf{A}_{i,j-1}$ from equation 7 and $\mathbf{E}_{i,j-1}$ from equation 17.
3. Compute Cartesian positions and velocities from equations 7 and 13.
4. Compute mass matrix of each body \mathbf{M}_i and augmented mass matrix \mathbf{K}_i from equations 40 and 54.
5. Compute Cartesian forces from equations 36 and 37. All spring and tire forces are added to each body as explained previously.
6. Compute velocity couplings \mathbf{R}_i from equation 28.
7. Compute force vector of each body \mathbf{Q}_i and augmented force vector \mathbf{F}_i from equations 41 and 55.
8. Compute a system mass matrix and system force vectors from equation 57.
9. Assemble the equations of motion (and solve for accelerations) that are integrated to predict the motion of the dynamic system. Go to step 1.

Performance Analysis Program

This program is the interface between the vehicle simulation and pavement analysis segments. Tire forces are computed at a given simulation time and saved in the required format for use in pavement analysis.

Although the output of the analysis program gives detailed vehicle dynamic response, it is necessary to interpret these responses as a dynamic impact factor in order to predict pavement loading and deformation. Two distinct methods are used to measure the dynamic response: aggregated force (Markow et al., 1988) and dynamic load coefficient (Hu, 1988).

Aggregated Force

Concise measures of vehicle forces make it easier to display the sensitivity of dynamic loading to pavement and vehicle parameters. These measures embody the effects of the overall vehicle, rather than any specific axle combination. The aggregated force at a particular point k is

$$\mathbf{F}_k = \sum_{j=1}^{N_a} \mathbf{P}_{jk} \quad \text{for } k = 1, 2, \dots, N_s \quad (68)$$

using the following definitions:

- N_a number of vehicle axles j
- P_{jk} force imposed by axle j at slab location k
- N_s local number of stations k along the slab length

Dynamic Load Coefficient

The total load that a wheel set exerts on the pavement at any time is equal to the static load plus a dynamic component equal to the axle load at that time. For continuous operation over a given segment of road, a statistic called the dynamic load coefficient (DLC) is commonly used as an indicator of the level of dynamic load. In Phase II, all parametric studies are performed using one form of the DLC, given as

$$\text{DLC} = \frac{\text{Standard Deviation of Axle Loads}}{\text{Mean Axle Loads}}$$

$$= \sqrt{\frac{1}{N-1} \sum_{j=1}^N \left(1 - \frac{X_j}{\bar{X}}\right)^2} \quad (69)$$

$$\text{where } \bar{X} = \frac{1}{N} \sum_{j=1}^N X_j$$

using the following definitions:

- X_j axle force of vehicle axles j
- N total number of stations along a given segment of road

Simulations and Discussions

Program Validation

This section presents program validation and performance evaluation of the general purpose recursive code truck simulation program developed in Phase II by comparing the results with those obtained with a mainframe version of DADS. Total elapsed CPU time will be used to measure relative performance.

Two types of truck models are tested: a simplified quarter truck model, and both full tractor and trailer combination models. The quarter truck model is used to validate truck subsystems such as tire, leaf spring, and TSDA (Translational Spring-Damper and Actuator) modules. Full truck models (tractor/semitrailer and double) are simulated to determine generalizability of the recursive code and for the performance evaluation.

The recursive code is executed on a Macintosh IIfx, 68030 CPU running at 40 MHz clock rate. As previously mentioned, DADS is not available for this personal workstation. Thus, a practical performance comparison was obtained using the VAX 11/780.

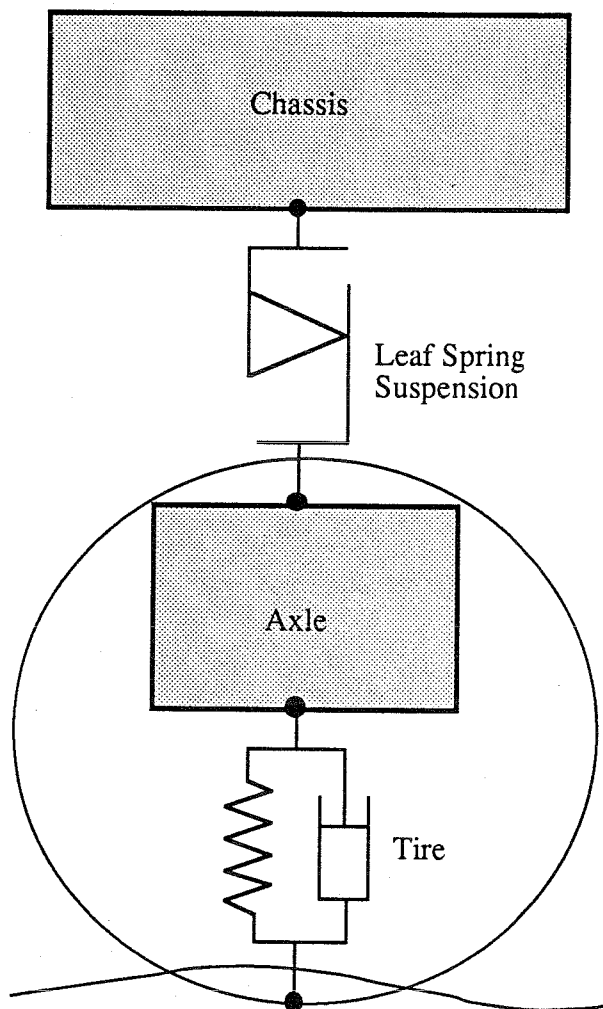


Figure 2-11
Prototype of Quarter Truck Model

Quarter Truck Model

Figure 2-11 shows a schematic configuration of a quarter truck. The chassis and axle are connected by a translational joint. A leaf spring or TSDA is attached as a compliance model.

The truck is assumed to start in an equilibrium condition. The step excitation (faulting) theoretically excites all of the truck frequencies and provides a simplified method for assessing parameter variation. In order to excite all the dynamic characteristics, a half-inch continuous fault road profile is used, shown in Figure 2-14.

Figure 2-17 shows a comparison of simulation results using a TSDA suspension model. The recursive code is well matched with those obtained from DADS, indicating that the tire and TSDA subsystems are reasonable.

Figure 2-18 shows a comparison of the simulation results using a leaf spring suspension model. Results from DADS deviate slightly from those derived from the recursive code because the leaf spring model depends on the values of the previous time step shown in equation 21. Note that integration methods of DADS and the recursive code are different. DADS

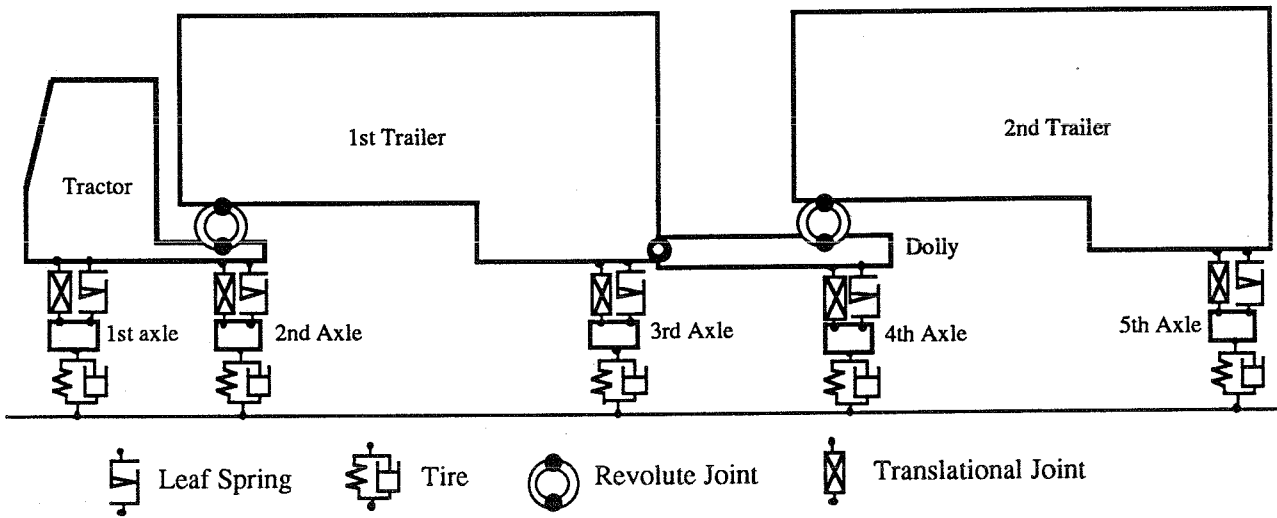


Figure 2-12
Multibody Configuration of 27-Foot Doubles Combination

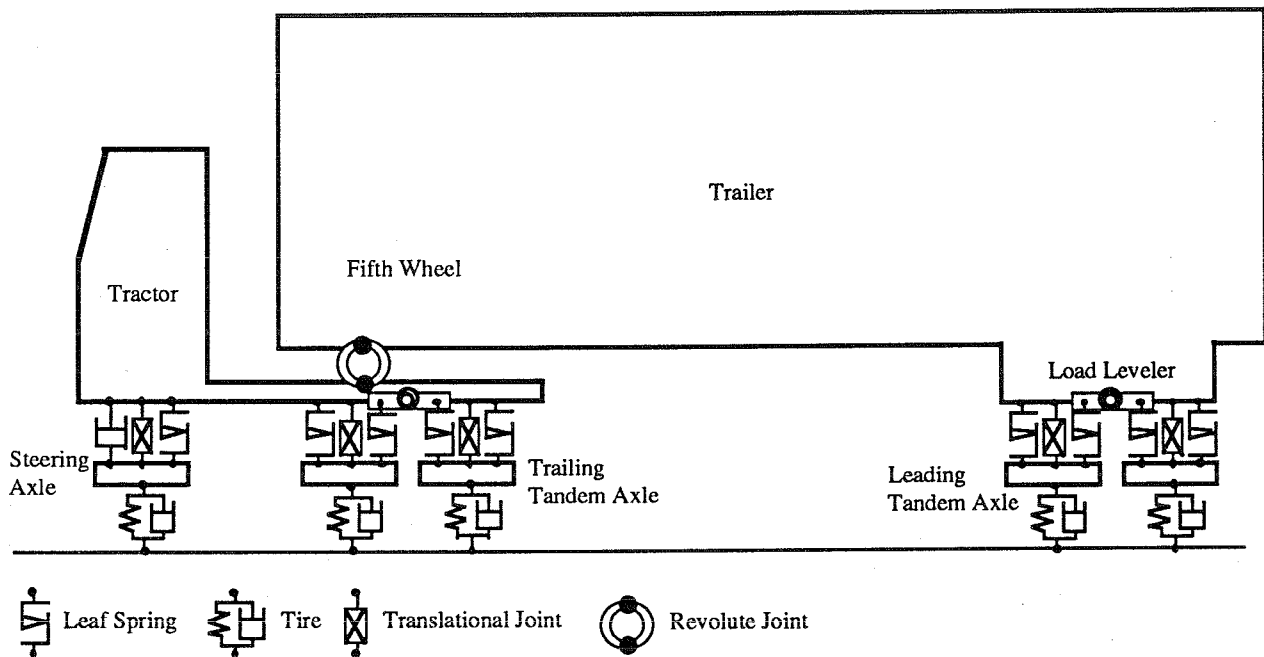


Figure 2-13
Multibody Configuration of Eighteen Wheeler Tractor and Semitrailer Combination

uses a DE integration method, which is an Adam Bashford predictor-corrector method and controls the integration step size and order internally. The recursive code uses a third order Adam Bashford integration method with constant step size.

Double Truck Model

Figure 2-12 illustrates a multibody configuration for a 27-foot doubles combination. This is a nine-body and ten-degree-of-freedom system, consisting of a tractor with two single axles; two semitrailers, each with two single axles; and a dolly with a single axle. Two fifth wheels are attached: one between the tractor and the other between the first trailer, and the first and second trailer. TSDA models are used for the single axle suspension models.

The truck is simulated on a random rough road profile as shown in Figure 2-15. Figures 2-19 and 2-20 show a comparison of the dynamic axle loads of the second axle attached to the tractor and the fourth axle attached to the dolly. The results from the recursive code are almost the same as those from DADS. Table 2-3 shows CPU time comparison between two simulation codes.

Table 2-3
CPU Time Comparison Between DADS and Recursive Code
For Five-Second Simulation
(seconds)

	DADS	Recursive Code
VAX 11/780	3,374	207
Apple Macintosh IIfx	Not Available	87

The recursive code is about sixteen times faster than DADS on the VAX780 series. It takes approximately one minute for a five-second simulation on a MAC IIfx, which computation speed is quite acceptable for the interactive truck simulation.

Parametric Studies

The drastic speedup of the dynamics simulation using the recursive code will enable analysts to perform interactive parametric studies. The effect of several truck parameters on pavement are tested to illustrate this capability.

An eighteen-wheeler tractor and semitrailer was used for this parametric study. Geometric and dynamic data of this model are the same for the 3S2 model used in Phase I of this study. Figure 2-13 shows a multibody configuration of the tractor and semitrailer model.

Truck parameters including tire spring stiffness, leaf spring stiffness, and payload, are tested by varying truck speed (between 45 mph and 65 mph) on two road profiles (rough profile shown in Figure 2-15, and smooth profile shown in Figure 2-16).

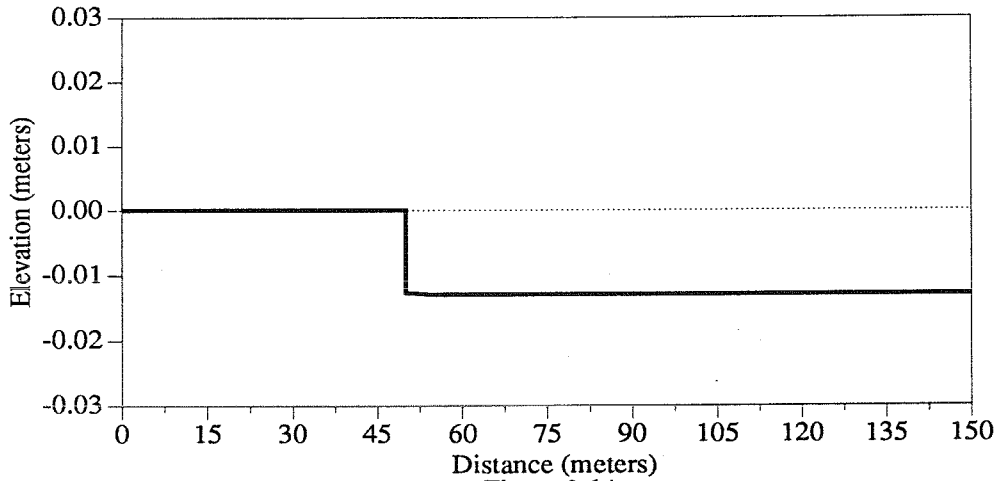


Figure 2-14
Half-Inch Faulting Road Profile

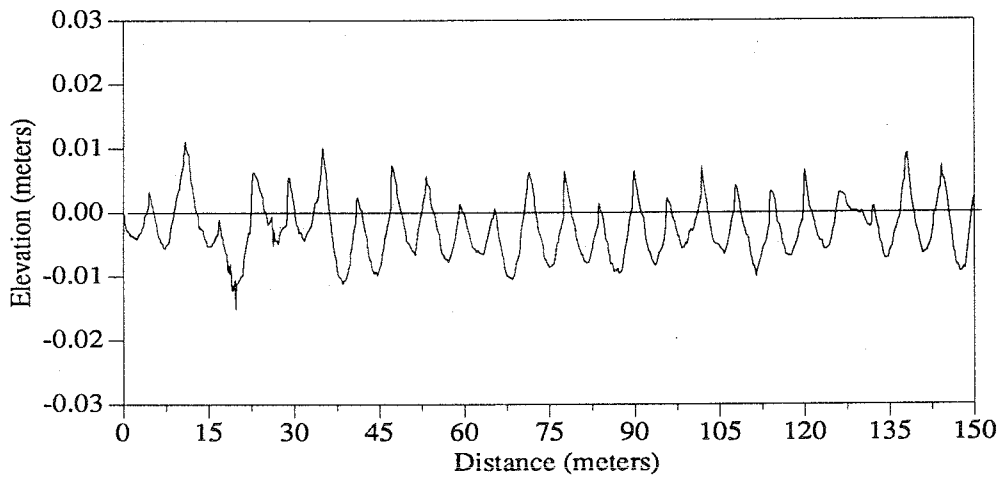


Figure 2-15
Random Rough Road Profile

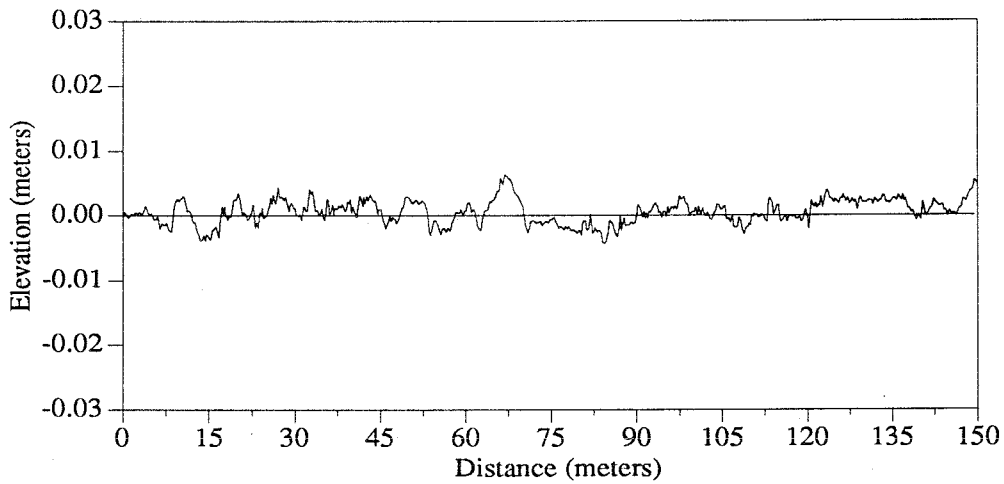


Figure 2-16
Random Smooth Road Profile

Figures 2-21 and 2-22 are comparisons of leading tandem axles of the eighteen wheeler tractor and semitrailer for the smooth and rough profile, respectively.

The results of parametric studies are shown in Tables 2-4, 2-5, and 2-6, showing that a reduction or increase of tire spring stiffness and leaf spring stiffness from the nominal values has a small effect on truck dynamics, and therefore a small effect on rigid pavement damage for the conditions tested in these studies. As shown in Tables 2-4, 2-5, and 2-6, dynamic axle loads are heavily dependent on the change of speed, payload, and road roughness.

Table 2-4
Dynamic Load Coefficients for Varying Tire Spring Stiffness

Tire Spring Stiffness	Road	Steering Axle		1st Tandem Axle of Tractor		1st Tandem Axle of Trailer	
		45 mph	65 mph	45 mph	65 mph	45 mph	65 mph
20% Reduction	smooth	3.6	6.3	7.6	9.5	6.2	13.7
	rough	9.5	12.2	17.9	14.9	52.8	32.8
10% Reduction	smooth	3.6	7.2	7.5	10.9	8.2	18.3
	rough	9.2	12.3	20.3	16.0	49.2	28.9
Full	smooth	3.7	6.8	7.9	10.4	9.0	19.7
	rough	10.9	13.3	20.2	19.7	58.4	27.8

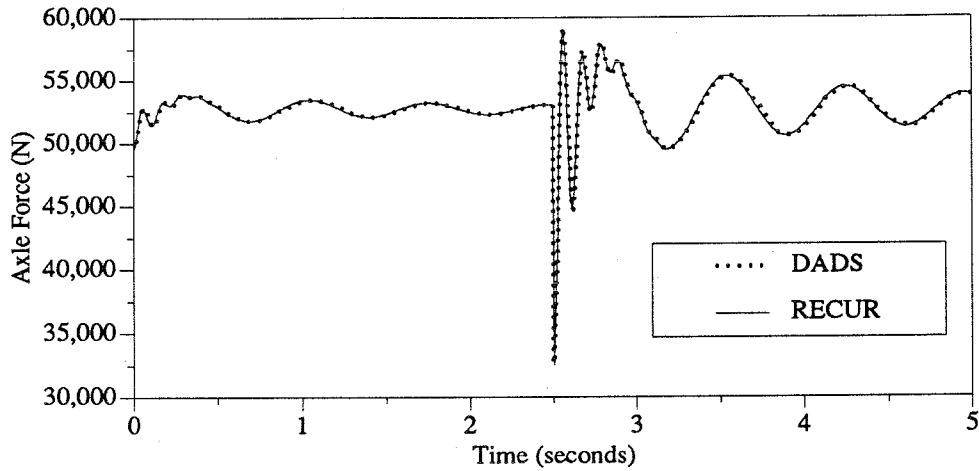


Figure 2-17
Comparison of Axle Load of Quarter Truck, With TSDA Spring

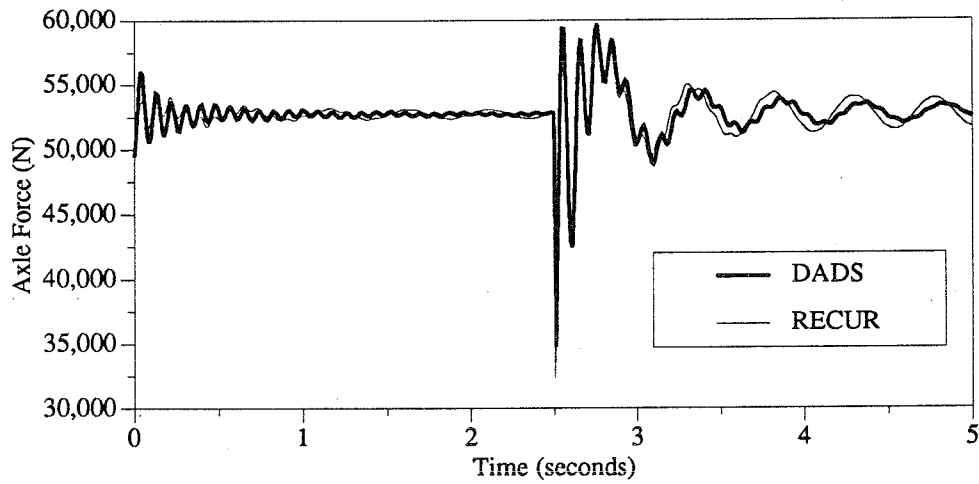


Figure 2-18
Comparison of Axle Load of Quarter Truck, With Leaf Spring

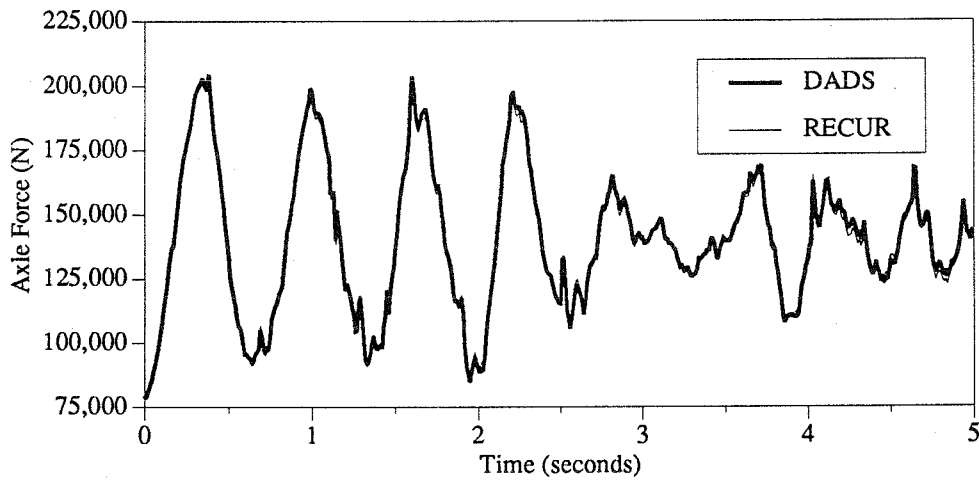


Figure 2-19
Comparison of Second Axle Load of Double Truck, With TSDA Spring

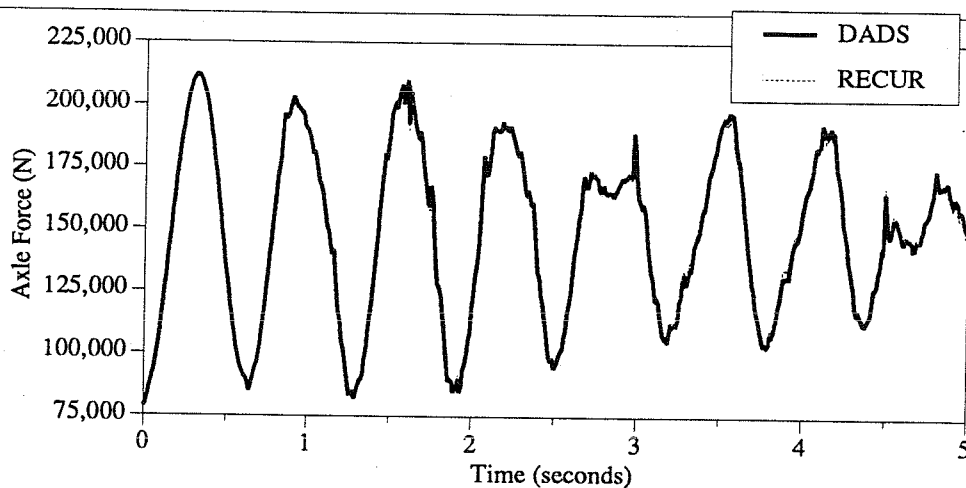


Figure 2-20
Comparison of Fourth Axle Load of Double Truck, With TSDA Spring

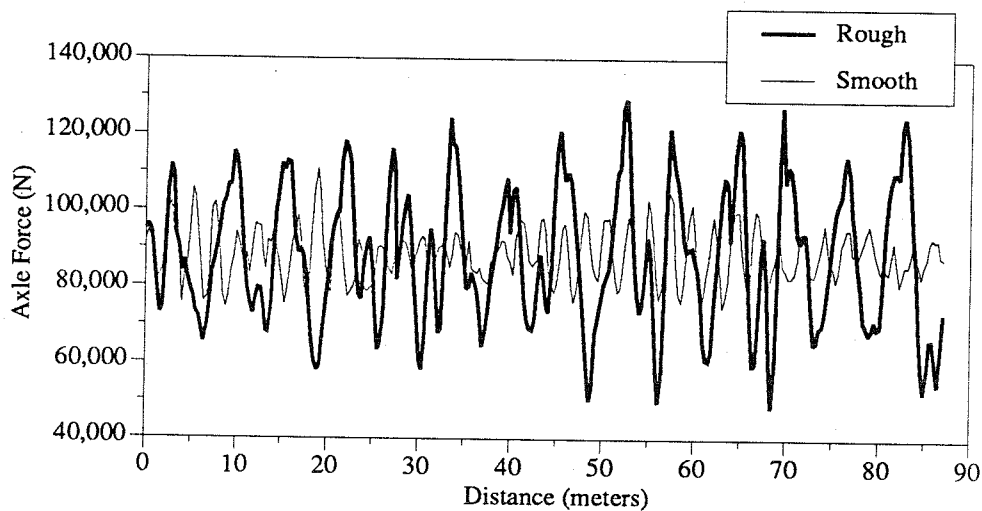


Figure 2-21
Comparison of Axle Load of Leading Tandem Axle of Tractor

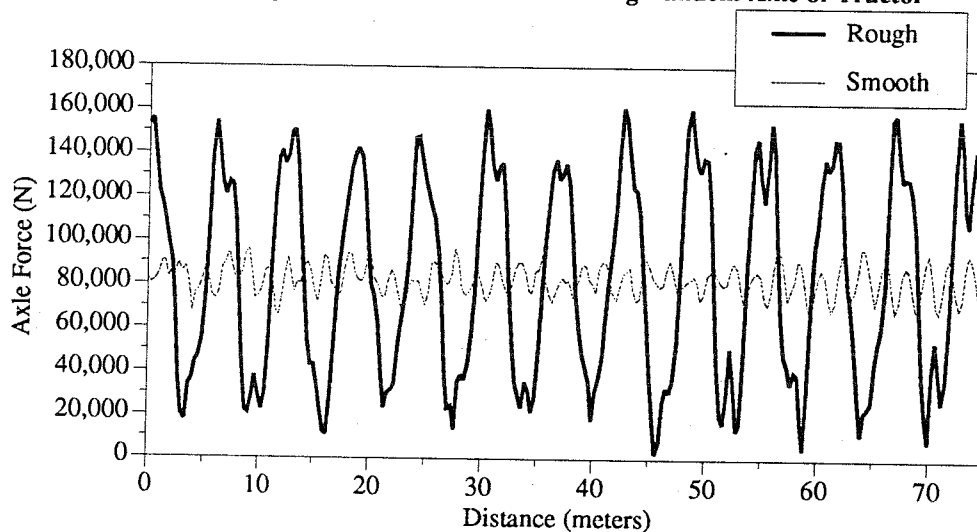


Figure 2-22
Comparison of Axle Load of Leading Tandem Axle of Semitrailer

Table 2-5
Dynamic Load Coefficients for Varying Leaf Spring Stiffness

Leaf Spring Stiffness	Road	Steering Axle		1st Tandem Axle of Tractor		1st Tandem Axle of Trailer	
		45 mph	65 mph	45 mph	65 mph	45 mph	65 mph
20% Reduction	smooth	3.6	5.8	7.7	9.8	8.9	18.7
	rough	9.5	13.6	14.3	21.1	36.6	28.5
10% Reduction	smooth	3.6	6.5	7.8	10.0	8.8	19.1
	rough	9.5	13.4	16.3	20.4	47.8	28.2
Full	smooth	3.7	6.8	7.9	10.4	9.0	19.7
	rough	10.9	13.3	20.2	19.7	58.4	27.8
10% Increase	smooth	4.0	7.6	8.0	11.0	9.2	21.0
	rough	12.0	13.6	19.0	19.6	49.1	28.0
20% Increase	smooth	4.4	8.4	8.1	11.4	9.5	22.1
	rough	15.0	14.5	22.0	20.0	46.6	29.3

Table 2-6
Dynamic Load Coefficients for Varying Payload (Full Payload = 2,884 N)

Payload	Road	Steering Axle		1st Tandem Axle of Tractor		1st Tandem Axle of Trailer	
		45 mph	65 mph	45 mph	65 mph	45 mph	65 mph
1/3	smooth	8.6	9.4	27	28	61	64
	rough	16.5	13.1	32	34	63	71
2/3	smooth	4.6	5.2	7.9	9.4	48.6	51.2
	rough	12.7	11.8	15.6	19.2	50.8	70.9
Full	smooth	3.7	6.8	7.9	10.4	9.0	19.7
	rough	10.9	13.3	20.2	19.7	58.4	27.8

3. PAVEMENT MODELING

PAVEMENT EVALUATION

A two-dimensional plate bending model supported on a representation of the subgrade is used to model rigid pavements. In this representation, it is assumed that the subgrade behaves as a Winkler foundation, i.e., that the reaction at any point of the base is proportional only to the deflection of the slab at that point.

A finite element model (FEM) is used for analysis of rigid pavements in which the slab is represented by plate elements and the foundation by a series of vertical springs located at different nodes. The same model was used by Stoner et al. (1990); the only difference is that a more refined finite element discretization is used.

Pavement Response Analysis Procedure

The procedure followed in the linear elastic analysis of the pavement model is similar to the one used by Stoner et al. (1990). This procedure is divided in two parts:

Dynamic Force Estimates at Tire-Pavement Contact Points

Forces are estimated by simulation of a vehicle with a known characteristics traveling over a pavement with known or assumed profile. For the purpose of this simulation the pavement is assumed to be rigid (i.e., the interaction between pavement response and the vehicle is neglected).

The end result of the dynamic simulation process is a set of dynamic forces as functions of time at tire-pavement contact points.

Pavement Response Analysis Calculations

The process of determining the pavement response is based on the principle of superposition and consists of the two following steps:

Generation of Influence Curves

Influence curves for selected nodes, on the finite element model are constructed. These curves represent response (pavement deflection) at a specific node as a unit load travels along a wheel path. A description of this process can be found in Stoner et al. (1990).

Response Curve for a Particular Node

A response curve for a specific point shows the deflection at that point as a vehicle travels over a segment of the pavement.

In order to determine the response at particular nodes the dynamic forces for each axle (forces versus time data) obtained from the vehicle simulation are first converted into forces versus distance along the pavement. The response at that point due to a single axle is then computed by multiplying the ordinate of the influence curve at that particular point with the force at that point from the force versus distance profile. This process is repeated for each axle separately. The superposition of these curves, taking into account the distance between the axles, then provides the response curve due to all vehicle axles. In these response curves, the steering axle is taken as reference (i.e., its position characterizes the vehicle position).

Parametric Study

The parametric study is performed using a five-axle tractor-trailer, with geometric characteristics as shown in Figure 2-13, and other characteristics such as mass distribution and suspension characteristics described in Chapter 2 of this report.

The pavement model for the parametric study consists of eight 20' long and 24'10" wide segments. Only the middle two segments (called test segments) are monitored for analysis results. The remaining segments are needed to provide continuity of the pavement. The discretized finite element model is shown in Figure 3-1. The pavement characteristics are similar to those of the Iowa DOT test site on I-80 near Avoca, Iowa.

Deflections are computed and plotted for nodes under the wheel closest to the edge of the pavement (nodes 52 to 85) as shown in Figure 3-2.

Results of Parametric Studies

The effects of different vehicle characteristics, vehicle speeds and pavement roughness on the deflection response were investigated. Numerical results are included for the following cases:

1. Nominal case
2. One-third payload
3. Two-thirds payload
4. Reduction of tire stiffness by 10 percent
5. Reduction of tire stiffness by 20 percent
6. Increase of leaf spring stiffness by 10 percent
7. Decrease of leaf spring stiffness by 10 percent

All of these cases were analyzed for two different vehicle speeds, 45 mph and 65 mph, and two different road profiles, rough and smooth, giving a total of 28 load cases.

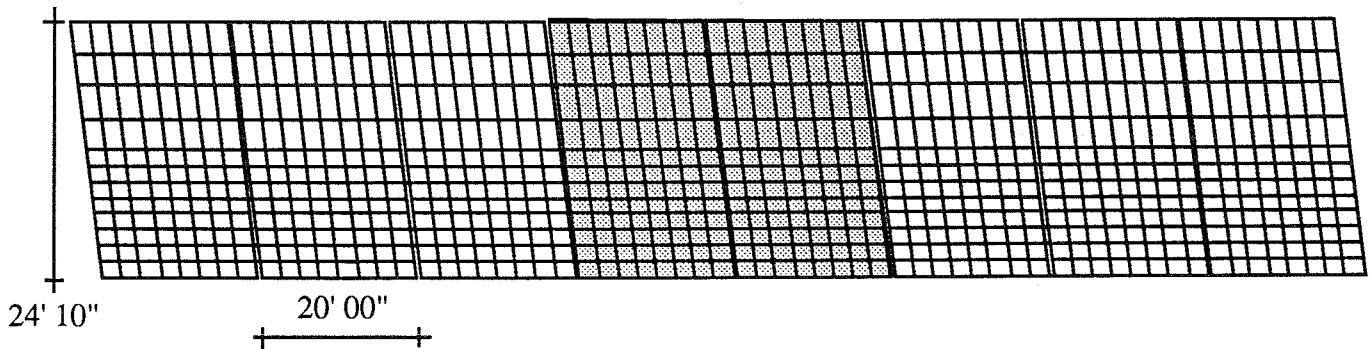


Figure 3-1
Pavement Model for Parametric Study

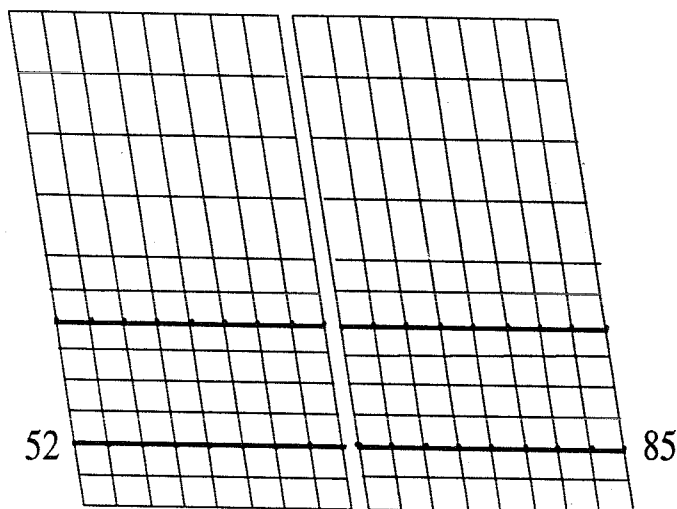


Figure 3-2
Travelling Path on Test Slabs

Presentation of Response Results for Each Case

For each case listed above, plots are provided showing the following results:

1. *Plots of axle forces as functions of distance from the start of the pavement model.* The distance axis (x-axis) is labeled from 0 to 160 feet (8 slabs, each 20 feet long). Note that the response results are monitored for the middle two slabs only. Thus forces between 60 feet and 100 feet will have the greatest influence on the response. Figures 3-3, 3-4, and 3-5 show some of these plots corresponding to the nominal case for 65 mph, on rough profile.
2. *The envelopes of maximum deflections (displacements) at nodes along the travel path.* These maxima are obtained from the nodal response curves. The x-axis of the envelopes represent distance of a point from the start of the pavement model. Thus the range is from 60 feet to 100 feet (test segments). The vertical axis gives the maximum deflection (in inches) at a point as the vehicle travels over the entire pavement segment. Figure 3-6 shows the envelope of maximum deflection for the nominal case, at 65 mph, on rough profile.

Nominal Case

The largest dynamic forces are generated at a speed of 45 mph for the rough profile, with the largest forces being experienced by the fifth and fourth axles (in that order). These axles show a low frequency response, while the same axles at the same speed, on smooth profile show a higher frequency response. The 45 mph case is clearly dominant on rough profile while the 65 mph case is the predominant one on a smooth profile. The maximum displacement envelopes show that the slab joints have the largest absolute displacements. The center points of the slabs do not deflect as much. On rough profile, 45 mph produces higher deflection; while 65 mph produces higher deflection on smooth profile. The maximum deflection is reached at the junction of the two test segments for the 45 mph cases while, for the 65 mph cases, maximum deflection is reached either at the start or at the end of these segments.

One-Third Payload

All axles reached higher forces on rough profile. The 45 mph case shows maximum forces on rough profile (third axle) while the 65 mph case shows maximum forces on smooth profile (second axle). The fifth axle shows higher dynamic effects at 65 mph on rough profile. Again the maximum displacements are reached at the slab joints. The 45 mph case produces higher deflections on both rough and smooth profiles. The rough profile cases produce the maximum at the junction of the two segments; whereas the smooth profile cases produce the maximum at the start of the first segment.

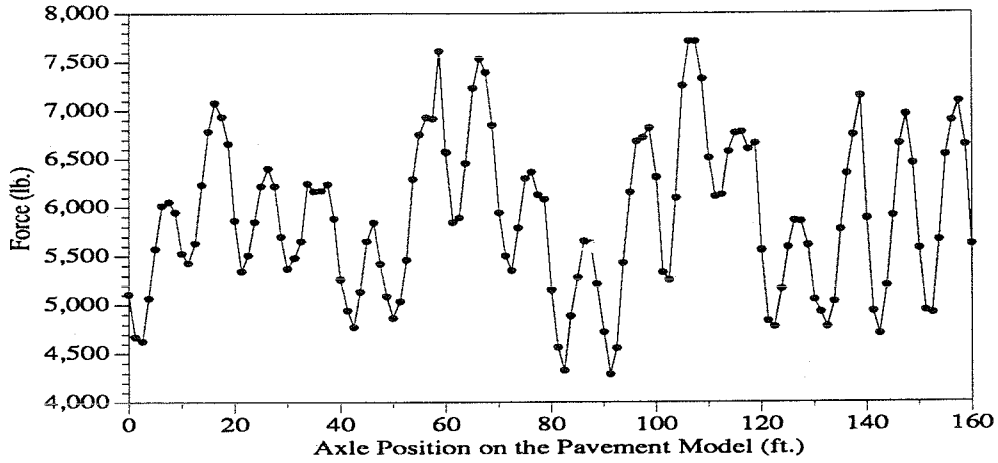


Figure 3-3
First Axle Forces (65 mph, nominal case, rough profile)

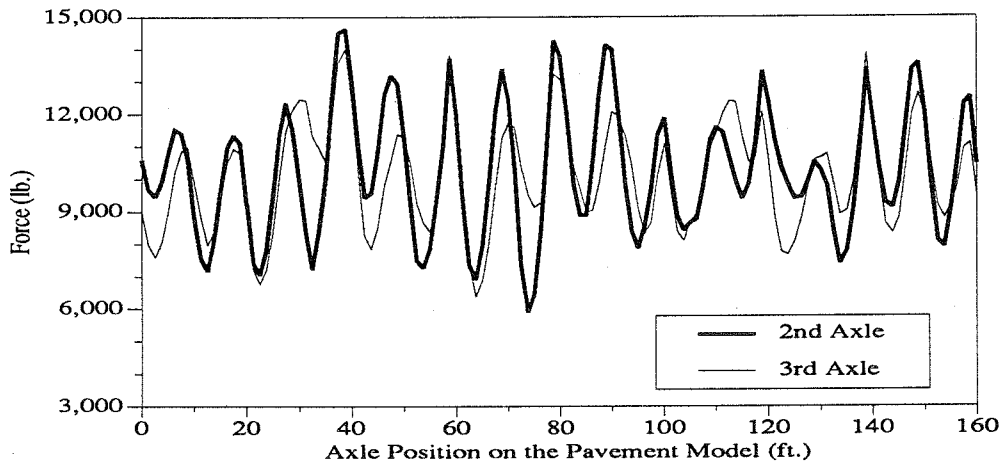


Figure 3-4
Second and Third Axle Forces (65 mph, nominal case, rough profile)

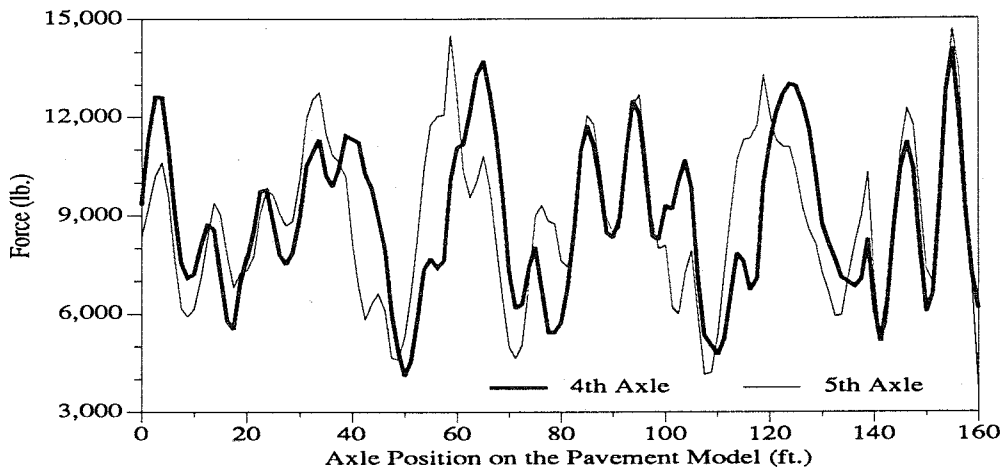


Figure 3-5
Fourth and Fifth Axle Forces (65 mph, nominal case, rough profile)

Two-Thirds Payload

Again the rough profile case is dominant for all axles at both speeds. The third axle shows the highest forces in all cases. The maximum force is produced by the 45 mph case. The fourth and fifth axles show higher dynamic influence on rough profile. Maximum displacements

are reached at the slab joints. Again the highest deflection is produced by the rough profile, but this time at the 65 mph speed. In most of the cases the maximum deflection is reached at the start of the test slabs.

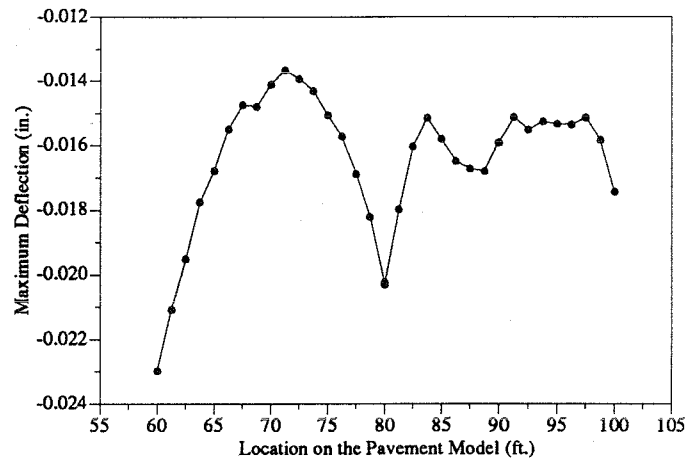


Figure 3-6
Maximum Pavement Displacement
(65 mph, nominal case, rough profile)

Reduction of Tire Stiffness by 10 Percent

The 45 mph case on rough profile is dominant. The maximum forces correspond to the second axle. The 65 mph case produces higher forces on smooth profile. At 45 mph, the fourth and fifth axles show the highest and lowest dynamic influence on rough and smooth profiles, respectively. Once again, maximum displacements are reached at the slab joints. At 65 mph on smooth profile, however, there are midspan deflections larger than the corresponding joint deflections for one of the test slabs. The 45 mph case on rough profile is dominant, given the maximum deflection.

Reduction of Tire Stiffness by 20 Percent

Once again the rough profile produces higher forces than those produced by the smooth profile. The second axle shows the highest forces on smooth profile, while the fourth axle (65 mph), and the fifth axle (45 mph) do the same on rough profile. The 65 mph speed on rough profile is the dominant case. Maximum deflections are found at slab joints (at the start of test slabs for 45 mph and at the end for 65 mph).

Increase of Leaf Spring Stiffness by 10 Percent

The 65 mph case gives the highest forces on both rough and smooth profiles, with the second axle on rough profile producing the highest values. The fourth and fifth axles show the highest dynamic influence at 45 mph on rough profile. Again the largest absolute displacements are found at the slab joints. The dominant case is 65 mph on rough profile. The rough profile produces the maximum deflection for both speeds.

Decrease of Leaf Spring Stiffness by 10 Percent

Just as in most of the previous cases, the forces for 65 mph truck speed are greater than those for the 45 mph speed. Furthermore, the rough profile produces the highest forces under the fourth and fifth axles, especially for the 45 mph speed on rough profile. These cases show displacement characteristics similar to the others.

For all cases studied, the dynamic forces at the axles are taken from the steady state section of the results of the dynamic simulation process.

Comparative Analysis

Results from all cases are compared in the following plots:

1. *Maximum pavement displacements for 45 mph.* Figure 3-7a shows the maximum deflections for all cases at 45 mph. In all cases, the rough profile gives the maximum values. The nominal case is the critical one, followed by reduction of tire stiffness by 10 percent.
2. *Maximum pavement displacements for 65 mph.* Figure 3-7b shows the maximum deflections for all cases at 65 mph. Again the rough profile is dominant. Increase of leaf spring stiffness by 10 percent is the critical case, followed by the nominal case.
3. *Maximum pavement displacements for rough profile.* Figure 3-8a shows the maximum deflections for all rough profile cases. There are four cases in which 45 mph is the dominant speed. The two most critical cases are the nominal case, followed by reduction of tire stiffness by 10 percent.
4. *Maximum pavement displacements for smooth profile.* Figure 3-8b shows the maximum deflections for all smooth profile cases. In this set, 65 mph is dominant for four cases. Increase of leaf spring stiffness by 10 percent is the critical case, followed closely by the nominal case, reduction of tire stiffness by 20 percent, and decrease of leaf spring stiffness by 10 percent.
5. *Envelopes of maximum deflection for payload cases.* Figures 3-9 to 3-12 show the envelopes of maximum displacements for reduction of

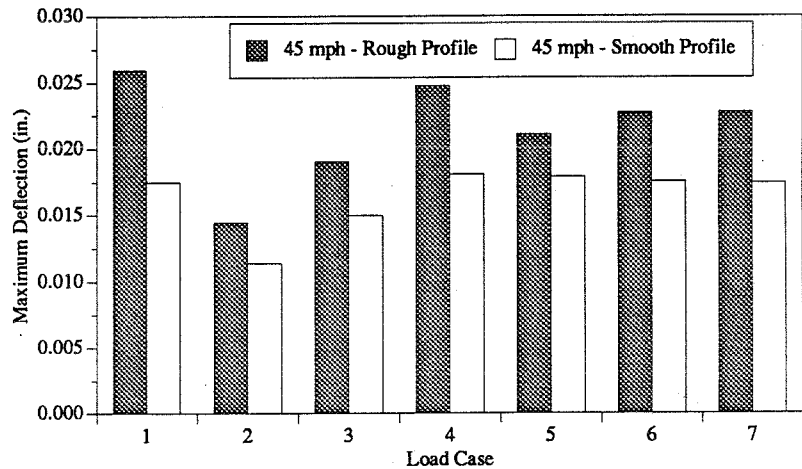


Figure 3-7a
Maximum Pavement Displacements for 45 mph

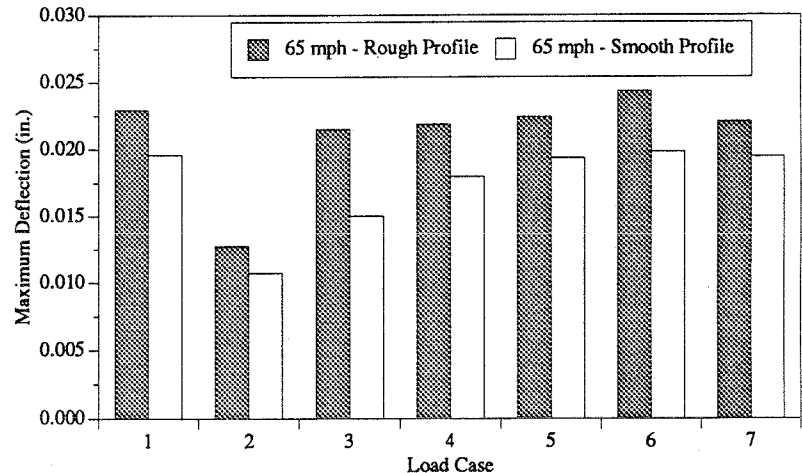


Figure 3-7b
Maximum Pavement Displacements for 65 mph

Load Cases:

1. Nominal
2. Reduction of Payload to One-Third
3. Reduction of Payload to Two-Thirds
4. Reduction of Tire Stiffness by 10 Percent
5. Reduction of Tire Stiffness by 20 Percent
6. Increase of Leaf Spring Stiffness by 10 Percent
7. Decrease of Leaf Spring Stiffness by 10 Percent

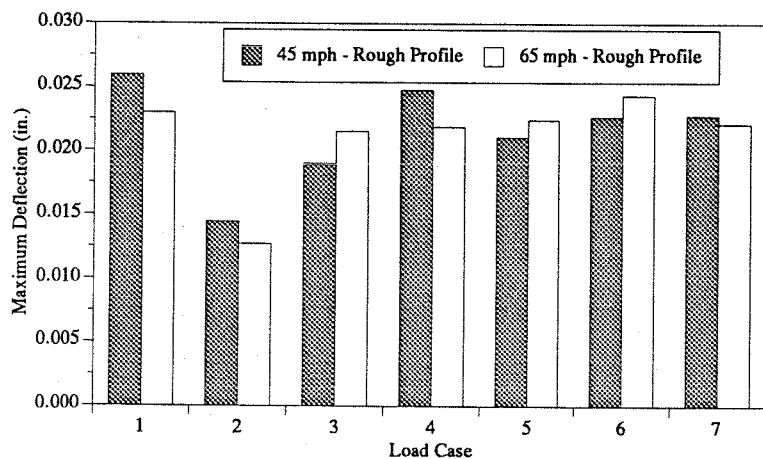


Figure 3-8a
Maximum Pavement Displacements for Rough Profile

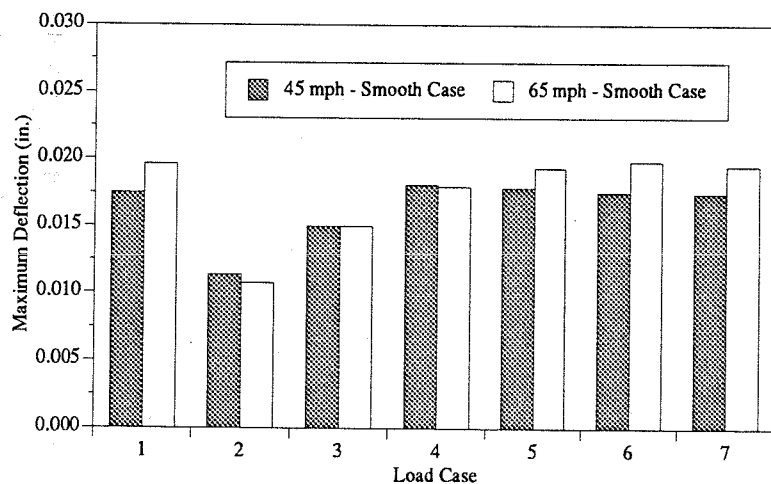


Figure 3-8b
Maximum Pavement Displacements for Smooth Profile

Load Cases:

1. Nominal
2. Reduction of Payload to One-Third
3. Reduction of Payload to Two-Thirds
4. Reduction of Tire Stiffness by 10 Percent
5. Reduction of Tire Stiffness by 20 Percent
6. Increase of Leaf Spring Stiffness by 10 Percent
7. Decrease of Leaf Spring Stiffness by 10 Percent

payload, compared with the nominal case (full payload). As might be intuitively expected, the deflections for these cases are approximately proportional to the reduction of payload, so the maximum deflections are always reached by the nominal case. Deflections for rough profile cases are larger than those for smooth profile cases. The dominant speed is 45 mph on rough profile and 65 mph on smooth profile. Thus the critical case is the nominal case on rough profile at 45 mph. If considering only the reduced payload cases, however, two-thirds payload on rough profile at 65 mph is the critical case.

6. *Envelopes of maximum deflection for reduction of tire stiffness.* Figures 3-13 to 3-16 show the envelopes of maximum displacements for reduction of tire stiffness. Again the rough profile produces the largest deflections. The critical speed for these cases is 45 mph. There is almost no influence of the tire stiffness reduction on smooth profile at 45 mph, and a very small influence at 65 mph. The critical case for this set is the nominal case on rough profile at 45 mph, or 10 percent reduction of tire stiffness for the same conditions.
7. *Envelopes of maximum deflection for variation of leaf spring stiffness.* Figures 3-17 to 3-20 show the envelopes of maximum displacements for variations of leaf spring stiffness. As with the previous set, the critical conditions are rough profile and 45 mph. The nominal case is the worst case, followed by an increase of leaf spring stiffness by 10 percent which is critical at 65 mph.

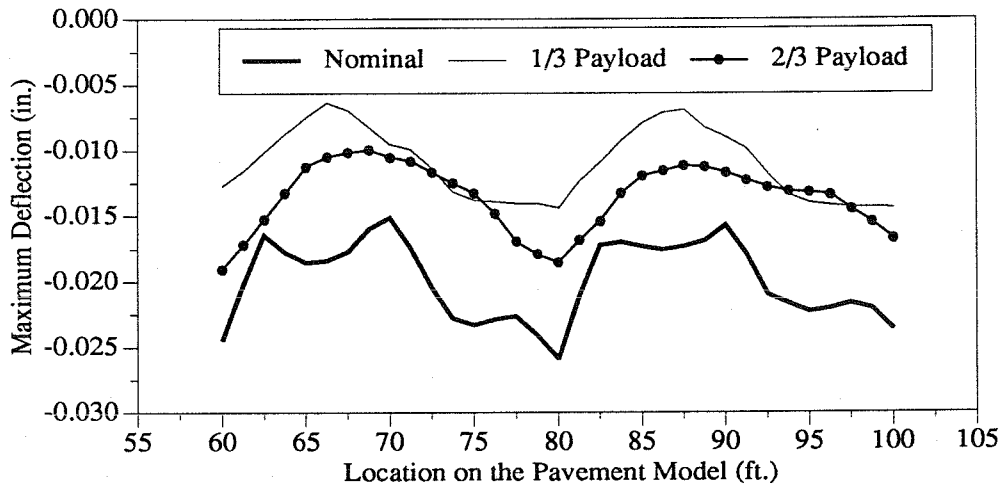


Figure 3-9
Envelopes of Maximum Pavement Displacements for 45 mph
on Rough Profile With Reduction of Payload

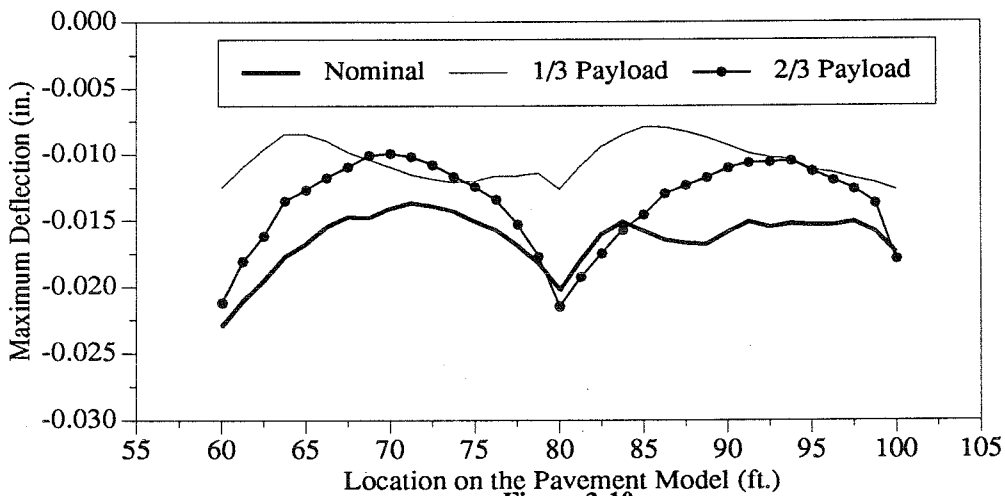


Figure 3-10
Envelopes of Maximum Pavement Displacements for 65 mph
on Rough Profile With Reduction of Payload

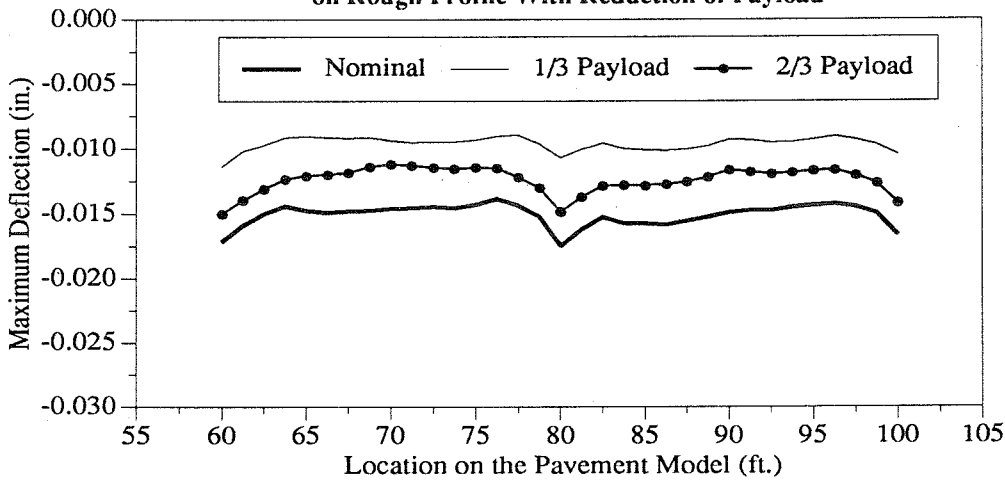


Figure 3-11
Envelopes of Maximum Pavement Displacements for 45 mph
on Smooth Profile With Reduction of Payload

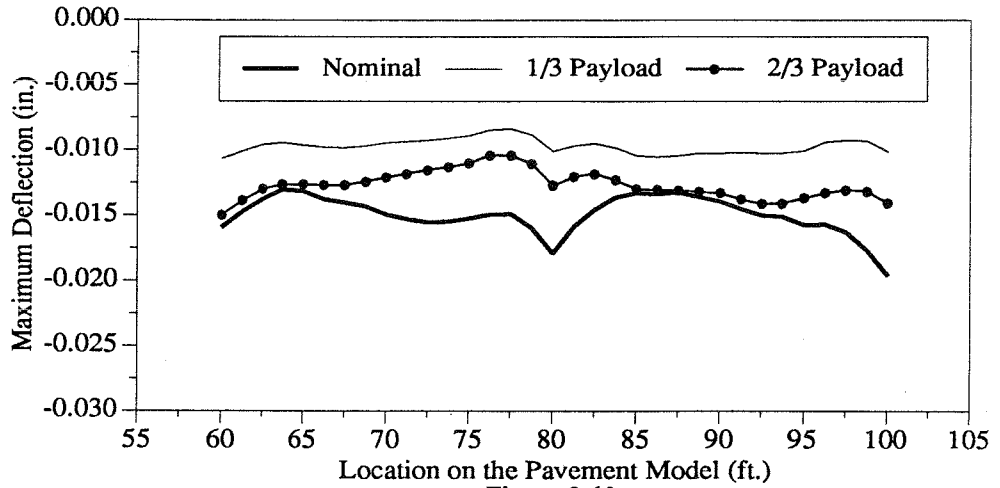


Figure 3-12
Envelopes of Maximum Pavement Displacements for 65 mph
on Smooth Profile With Reduction of Payload

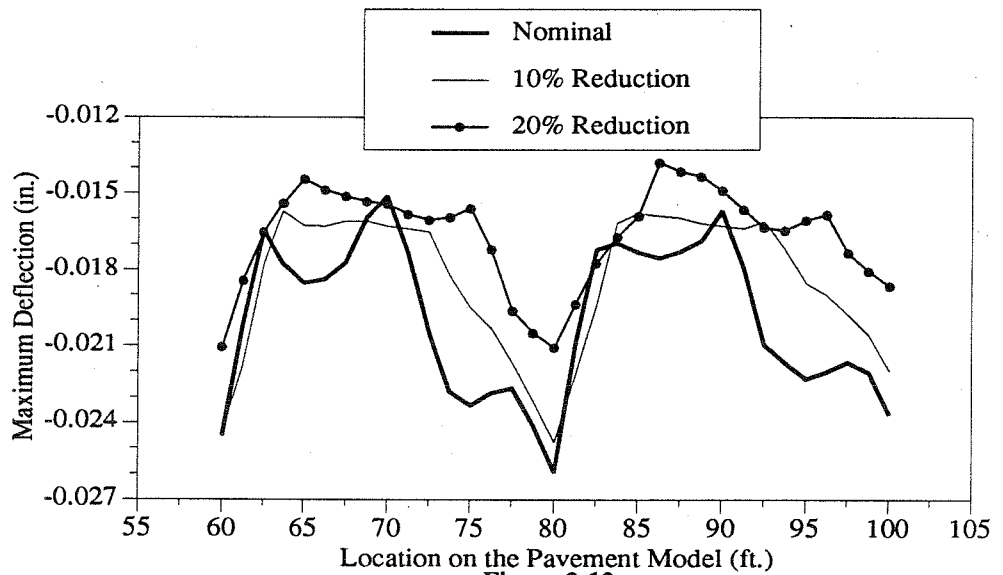


Figure 3-13
Envelopes of Maximum Pavement Displacements for 45 mph
on Rough Profile With Reduction of Tire Stiffness

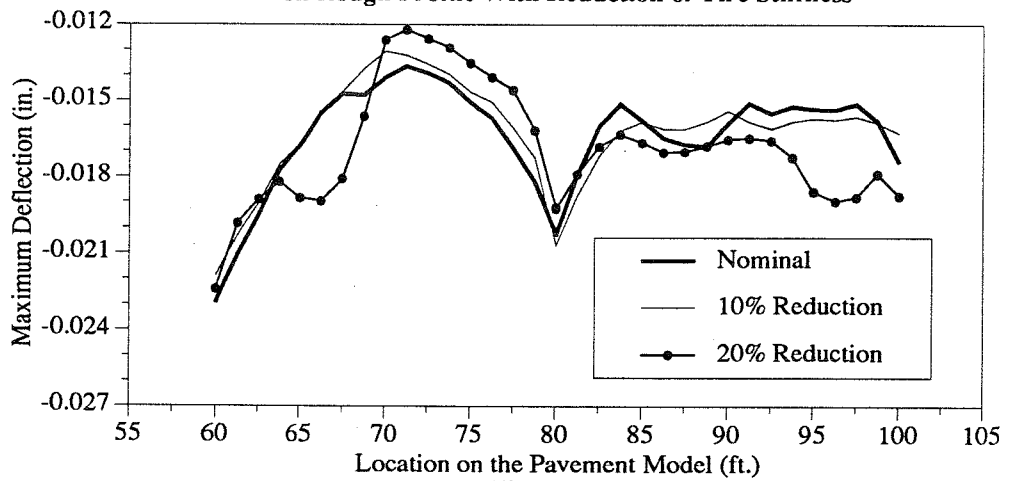


Figure 3-14
Envelopes of Maximum Pavement Displacements for 65 mph
on Rough Profile With Reduction of Tire Stiffness

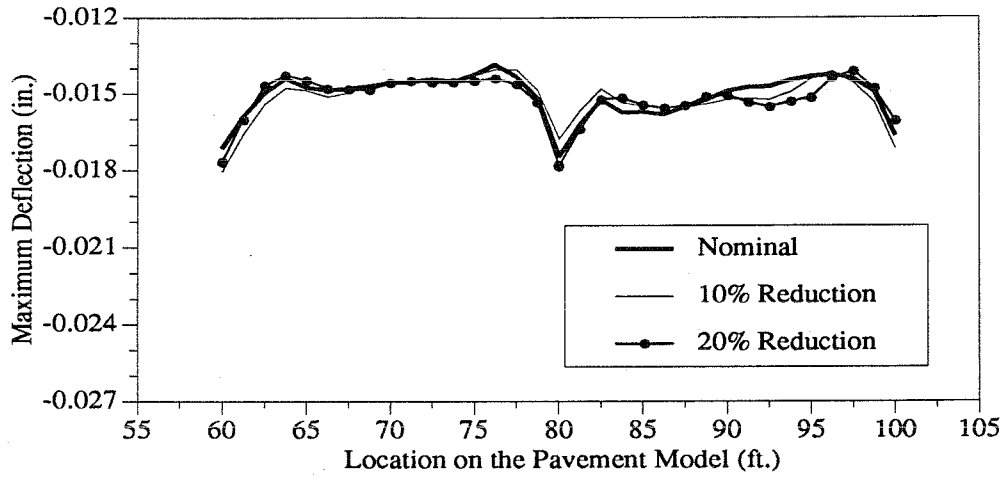


Figure 3-15
Envelopes of Maximum Pavement Displacements for 45 mph
on Smooth Profile With Reduction of Tire Stiffness

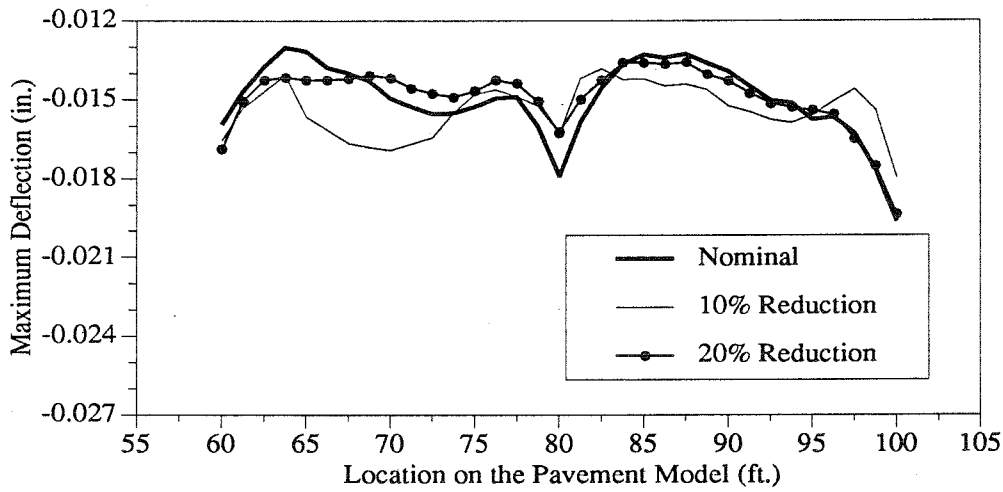


Figure 3-16
Envelopes of Maximum Pavement Displacements for 65 mph
on Smooth Profile With Reduction of Tire Stiffness

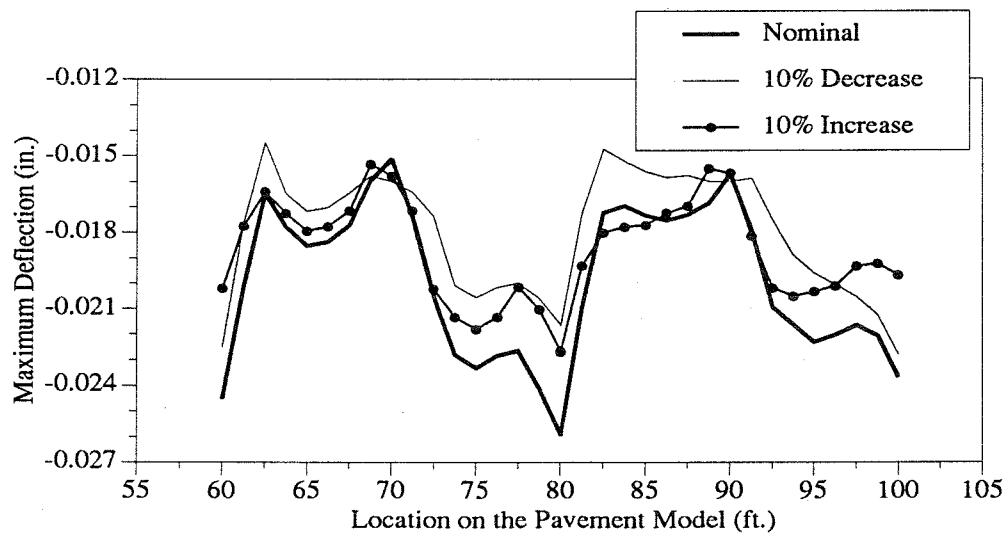


Figure 3-17
Envelopes of Maximum Pavement Displacements for 45 mph
on Rough Profile With Changes in Leaf Spring Thickness

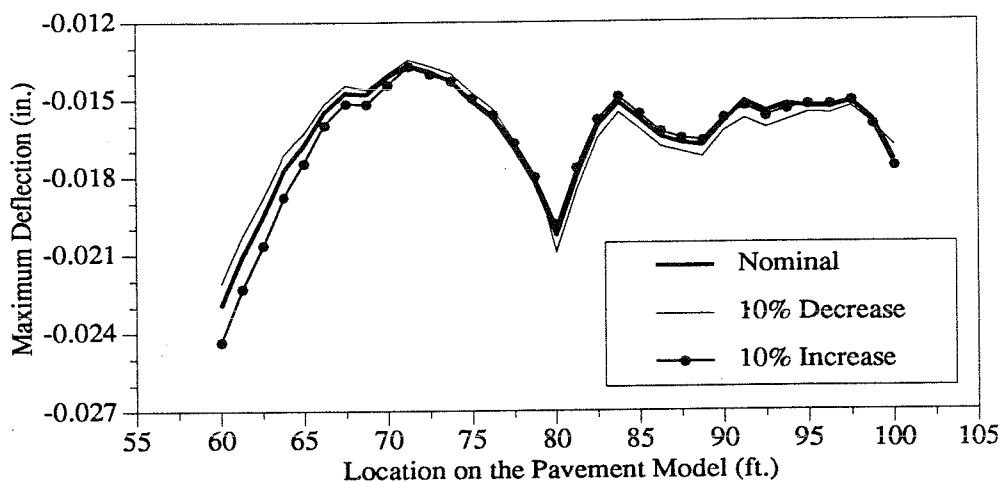


Figure 3-18
Envelopes of Maximum Pavement Displacements for 65 mph
on Rough Profile With Changes in Leaf Spring Thickness

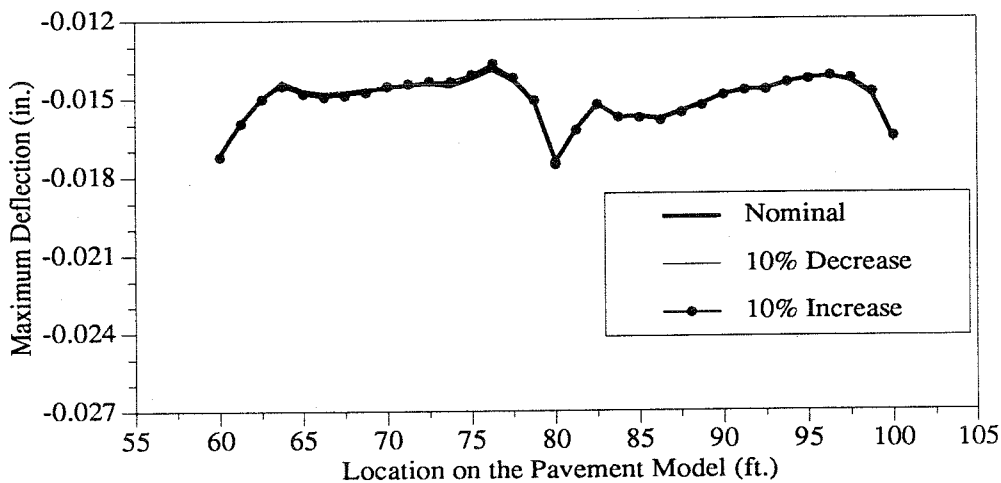


Figure 3-19
Envelopes of Maximum Pavement Displacements for 45 mph
on Smooth Profile With Changes in Leaf Spring Thickness

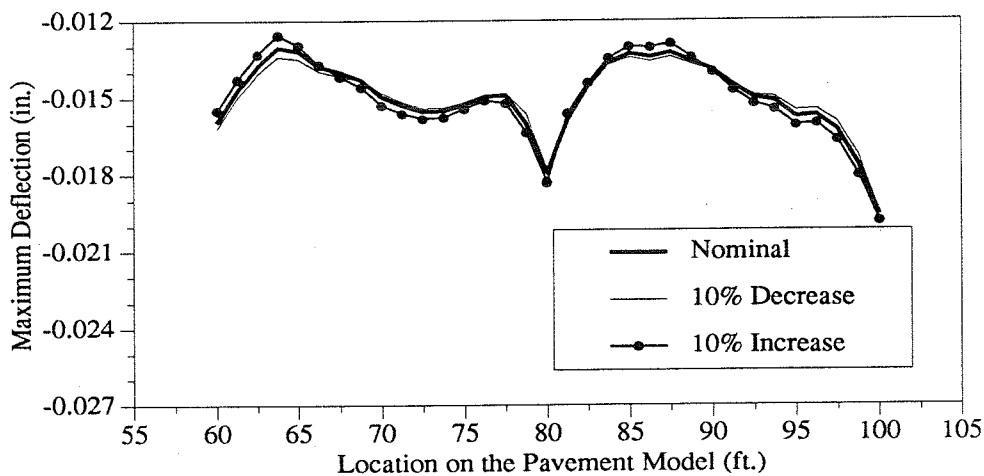


Figure 3-20
Envelopes of Maximum Pavement Displacements for 65 mph
on Smooth Profile With Changes in Leaf Spring Thickness

Axles Causing Maximum Deflections

Table 3-1 identifies the axle causing maximum deflection in each case.

Table 3-1
Axles Causing Maximum Deflections for Different Load Conditions

Load Case	Speed-Road Conditions	Maximum Deflection ¹	Node Position ²	Axle No. ³
Nominal	45 mph - rough profile	0.02595	80.025	4
	65 mph - rough profile	0.02297	60.025	5
	45 mph - smooth profile	0.01747	80.025	3
	65 mph - smooth profile	0.01961	100.033	3
One-Third Payload	45 mph - rough profile	0.01444	80.025	2
	65 mph - rough profile	0.01273	100.033	5
	45 mph - smooth profile	0.01137	60.025	2
	65 mph - smooth profile	0.01072	60.025	3
Two-Thirds Payload	45 mph - rough profile	0.01905	60.025	<u>2-3</u>
	65 mph - rough profile	0.02151	80.025	5
	45 mph - smooth profile	0.01499	60.025	3
	65 mph - smooth profile	0.01498	60.025	3
Reduction of Tire Stiffness by 10%	45 mph - rough profile	0.02476	80.025	<u>4-5</u>
	65 mph - rough profile	0.02190	60.025	<u>4-5</u>
	45 mph - smooth profile	0.01808	60.025	3
	65 mph - smooth profile	0.01796	100.025	3
Reduction of Tire Stiffness by 20%	45 mph - rough profile	0.02106	60.025	<u>4-5</u>
	65 mph - rough profile	0.02241	60.025	<u>4-5</u>
	45 mph - smooth profile	0.01786	80.025	3
	65 mph - smooth profile	0.01935	100.025	3
Increase of Leaf Spring Stiffness by 10%	45 mph - rough profile	0.02269	80.025	4
	65 mph - rough profile	0.02434	60.025	5
	45 mph - smooth profile	0.01754	80.025	3
	65 mph - smooth profile	0.01983	100.025	3
Decrease of Leaf Spring Stiffness by 10%	45 mph - rough profile	0.02278	100.025	4
	65 mph - rough profile	0.02211	60.025	5
	45 mph - smooth profile	0.01744	80.025	3
	65 mph - smooth profile	0.01947	100.025	3

Note: In those cases where two axles are indicated the maximum occurs between these axles, closest to the axle that is underlined.

¹ Maximum deflection for the load case (inches).

² Node position where the maximum occurs (feet from model origin).

³ Axle causing maximum deflection.

Rigid Pavement Representation

Concrete pavements are typically analyzed by means of closed form solutions (Westergaard, 1947) or charts derived from them (Pickett and Ray, 1951). The basic assumptions of these methods are full contact between slab and subgrade and continuity of the slab. The continuing application of computers has allowed the finite element method to be used to model concrete structures, allowing for a better representation of the material behavior.

Improved finite element representations of concrete pavements have been used to model characteristics such as non-linear properties of the concrete and subgrade, discontinuities in the slab, fatigue of the structural elements, and pumping of the subgrade.

In this section, a finite element formulation for jointed concrete pavement is presented. This formulation was modified to allow for non-linear behavior of the structure.

This pavement model is capable of including characteristic behavior of concrete in compression and tension and the impacts of cyclic loading. Dowels are represented so that the relative deformation of the bars with respect to the concrete slab is accounted for, and dowel and joint fatigue are also estimated in the model. The subgrade model can represent pumping of the fine material with repetitious load.

Concrete Modeling

Concrete in Compression

The matrix formulation for elasto-plastic materials presented by Nayak and Zienkiewicz (1972a, 1972b—see Appendix), allows the failure criteria to be readily expressed in a correct form for computer implementation.

The Yield Surface and Flow Rule

The yield surface can be seen as an extended Von Mises criteria accounting for the influence of hydrostatic pressure on the loading function. This function (Figueiras and Owen, 1984a, 1984b) can be written as:

$$f(I_1, J_2) = \left[\beta(3J_2) + \alpha I_1 \right]^{\frac{1}{2}} - \bar{\sigma} = 0 \quad (1)$$

where

- I_1 first invariant of the stress tensor
- J_2 second invariant of the stress tensor
- $\bar{\sigma}$ equivalent effective stress
- α, β material parameters

The material parameters α and β can be found empirically by curve-fitting of experimental results. Figueiras and Owen (1984b) calculated their values based on the results of Kupfer, Hilsdorf, and Rusch (1969) as:

$$\alpha = 0.355 \bar{\sigma} \quad (2a)$$

$$\beta = 1.355 \quad (2b)$$

A comparison with the experimental data in biaxial stress space is presented in Figure 3-21a. The flow rule can be expressed by the values of C_1 , C_2 and C_3 , as defined in the Appendix, as:

$$C_1 = 0.1775 \quad (3a)$$

$$C_2 = \frac{4.065 \sqrt{J_2}}{[\beta (3J_2) + \alpha I_1]^{(1/2)}} \quad (3b)$$

$$C_3 = 0.0 \quad (3c)$$

The Crushing Condition

Crushing failure is controlled by an expression similar to the yield function, but in strain space. This expression can be written as:

$$f(I'_1, J'_2) = [\beta (3J'_2) + \alpha I'_1]^{(1/2)} - \epsilon_u = 0 \quad (4)$$

where

- I'_1 first invariant of the strain tensor
- J'_2 second invariant of the deviatoric strain tensor
- ϵ_u ultimate total strain from a uniaxial compression test
- α, β material parameters

The material parameters α and β can be found empirically by curve-fitting of experimental results (see Figure 3-21b). Figueiras and Owen (1984b) calculated their values based on the results of Kupfer, Hilsdorf, and Rusch (1969) as:

$$\alpha = 0.355 \epsilon_u \quad (5a)$$

$$\beta = 1.355 \quad (5b)$$

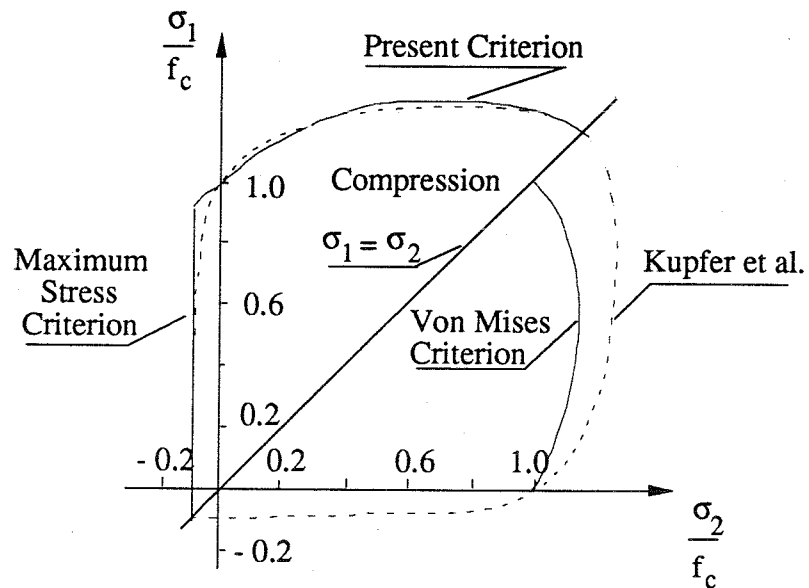


Figure 3-21a
Concrete Behavior Idealization:
Comparison with Data from Kupfer, Hilsdorf, and Rusch (1969)

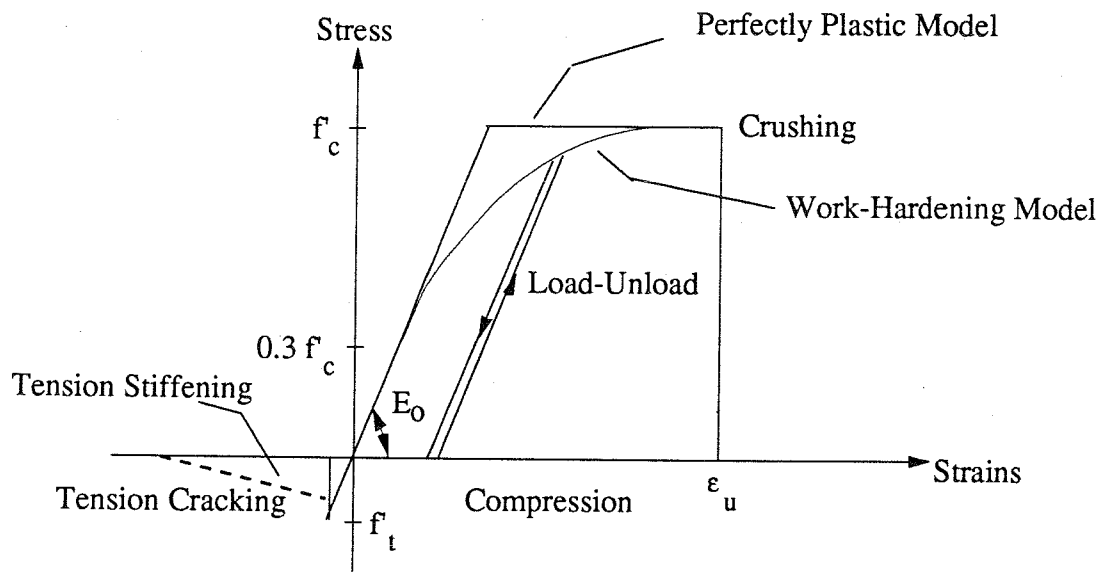


Figure 3-21b
Concrete Behavior Idealization:
Uniaxial Stress-Strain Representation

Concrete in Tension

Stress-Strain Relations for Cracked Systems

The response of concrete in tension is assumed to be elastic until the maximum tensile stress reaches the value of the concrete tensile strength, f_t . A crack then forms perpendicular to the maximum tensile stress.

The material is assumed to behave orthotropically after cracking has occurred, with the principal axes of orthotropy parallel and normal to the crack. The Young's modulus and Poisson's ratio in the direction normal to the crack are set to zero and a reduced shear modulus is employed.

If 1 and 2 are the principal directions, 1 being normal to the crack, the stress-strain relation for a point that has cracked in one direction is

$$\begin{Bmatrix} \sigma_1 \\ \sigma_2 \\ \tau_{12} \\ \tau_{13} \\ \tau_{23} \end{Bmatrix} = \begin{bmatrix} 0 & 0 & 0 & 0 & 0 \\ 0 & E & 0 & 0 & 0 \\ 0 & 0 & G_{12}^c & 0 & 0 \\ 0 & 0 & 0 & G_{13}^c & 0 \\ 0 & 0 & 0 & 0 & \frac{5}{6}G \end{bmatrix} \begin{Bmatrix} \epsilon_1 \\ \epsilon_2 \\ \gamma_{12} \\ \gamma_{13} \\ \gamma_{23} \end{Bmatrix} \quad (6)$$

where

$$G_{12}^c = 0.25 * G \left(1.0 - \frac{\epsilon_1}{0.004} \right), \text{ or } G_{12}^c = 0.0, \text{ if } \epsilon_1 \geq 0.004 \quad (7a)$$

$$G_{13}^c = G_{12}^c \quad (7b)$$

ϵ_1 tensile strain in the direction 1

When the principal stress in direction 2 reaches the value of f_t , a second crack forms perpendicular to the first one. The stress strain relation becomes

$$\begin{Bmatrix} \sigma_1 \\ \sigma_2 \\ \tau_{12} \\ \tau_{13} \\ \tau_{23} \end{Bmatrix} = \begin{bmatrix} 0 & 0 & 0 & 0 & 0 \\ 0 & 0 & 0 & 0 & 0 \\ 0 & 0 & G_{12}^c/2 & 0 & 0 \\ 0 & 0 & 0 & G_{13}^c & 0 \\ 0 & 0 & 0 & 0 & G_{23}^c \end{bmatrix} \begin{Bmatrix} \epsilon_1 \\ \epsilon_2 \\ \gamma_{12} \\ \gamma_{13} \\ \gamma_{23} \end{Bmatrix} \quad (8)$$

where

$$G_{13}^c = 0.25 * G \left(1.0 - \frac{\epsilon_1}{0.004} \right), \text{ or } G_{13}^c = 0.0, \text{ if } \epsilon_1 \geq 0.004 \quad (9a)$$

$$G_{23}^c = 0.25 * G \left(1.0 - \frac{\epsilon_2}{0.004} \right), \text{ or } G_{23}^c = 0.0, \text{ if } \epsilon_2 \geq 0.004 \quad (9b)$$

$$G_{12}^c = 0.5 * G_{13}^c, \text{ or } G_{12}^c = 0.5 * G_{23}^c \text{ if } G_{23}^c < G_{13}^c \quad (9c)$$

ϵ_1 tensile strain in the direction 1

ϵ_2 tensile strain in the direction 2

Tension Stiffening

Due to the bond effect between steel reinforcement and the surrounding concrete, a certain amount of tensile stress can be carried across the crack by the concrete. In this work, a gradual release of the concrete stress component normal to the cracked plane is adopted. The process of unloading and reloading is assumed to follow a linear elastic behavior with a fictitious modulus E_i . A graphical representation of the stress-strain relation for concrete is presented in Figure 3-22. It can be determined from this figure that the value of E_i is given by

$$E_i = \alpha f_t \left[\frac{\left(1.0 - \frac{\epsilon_i}{\epsilon_m} \right)}{\epsilon_i} \right], \quad \epsilon \leq \epsilon_i \leq \epsilon_m \quad (10)$$

using the following definitions:

α, ϵ_m material parameters

ϵ_i maximum value reached by the tensile strain

The stresses normal and parallel to the crack are obtained from

$$\sigma_i = \alpha f_t \left(1.0 - \frac{\epsilon_i}{\epsilon_m} \right), \quad \epsilon \leq \epsilon_i \leq \epsilon_m \quad (11)$$

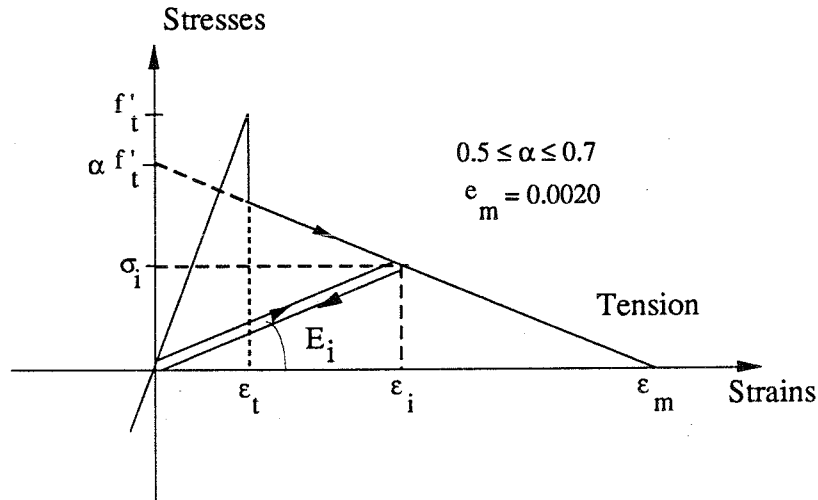


Figure 3-22
Tension Stiffening Idealization

Steel in Compression and in Tension

The reinforcing steel is considered a sequence of layers of equivalent thickness, representing unidirectional behavior by resisting forces only in the direction of the bars. An elasto-plastic representation of the material is assumed and the hardening parameter is calculated based on the plastic Young's Modulus as

$$H = \left(\frac{E_{ep}}{1 + \frac{E_{ep}}{E}} \right) \quad (12)$$

Fatigue of Concrete in Tension

As in many other materials, the mechanical properties of concrete are altered when subjected to cyclic loading. This fact has been recognized since the early 1920s; and yet, at the present time, a complete model for fatigue behavior of concrete is not available.

Because structural concrete is typically used under static rather than dynamic cyclic loading, knowledge of fatigue behavior of concrete paving has fallen behind when compared with other materials, such as metals. In the area of highway and airfield pavement design, however, such behavior characteristics become important.

Concrete pavement slabs are subjected to many types of repeated stress during their service life. The most noticeable of these are produced by traffic loading. Stresses due to moisture and temperature gradients can also induce cyclic stress. These stresses act upon the structure simultaneously and are additive in nature. Their effects can act in the same or opposing directions. It is evident that critical types of stress are produced by flexural moments, therefore data on fatigue due to flexural stresses are most often used for concrete pavement design.

During the last 40 years, several investigations on the fatigue behavior of plain concrete have been carried out. These studies have focused on a wide range of variables, such as the rate of loading (Kesler, 1953), range of stresses (Murdock and Kesler, 1958; Ballinger, 1972), the effect of rest periods and variable loading (Hilsdorf and Kesler, 1966) and the effect of air content and type of aggregate (Klaiber, Thomas, and Lee, 1979).

Various forms of fatigue tests have been used to investigate concrete's behavior under direct compression, direct tension, and indirect tension and flexure. The fatigue behavior in flexure is of particular importance.

It was concluded from these studies that although the rate of loading has a marked influence on the compression and flexural strength of concrete, fatigue performance does not seem to be affected in the same proportion (Raithby and Galloway, 1974). Also, experimental results show that rest periods between loading cycles seem unlikely to affect the fatigue behavior of concrete in a significant way.

It has also been suggested that the various factors that affect the static strength of concrete can also affect the fatigue strength in a similar way (Kesler, 1953; Neville, 1973; Nordby, 1958; Raithby and Galloway, 1974). Critical factors include the aggregate type, moisture condition, type of loading, specimen size and curing condition.

The existence of a stress limit below which no fatigue damage occurs, does not seem to exist, at least up to ten million cycles of load application (Troxell, Davis, and Kelly, 1968). Nevertheless, Clemer (1922) found that for up to two million cycles of load application, the endurance limit for concrete was based on loads of between 51 and 54 percent of the static modulus of rupture.

Results of concrete behavior under variable amplitude loading are scarce. These results would be representative of the behavior of a rigid pavement subjected to repeated traffic loading. Nevertheless, in view of the lack of experimental results, the behavior of a concrete specimen subject to a constant amplitude load is usually taken as representative of typical behavior.

It is important to notice that fatigue tests in compression have shown the importance of the order of application of the loading in the final value of the fatigue damage (Holmen, 1982). The test results show that the fatigue damage caused by one load cycle is governed by the effects of the preceding cycle or a sequence of preceding cycles.

Fatigue performance is generally expressed in terms of an "endurance curve." This curve represents the relation, under a particular loading condition, between the magnitude of the cycling stress and the mean value of the number of load cycles until failure. Figure 3-23 represents a typical endurance curve.

Measures of fatigue damage are rather subjective quantities. They are used to follow the progress of damage under certain conditions of loading and in relation to other structures (i.e., they are best suited to perform a parametric study of the performance of a given set of structures subject to similar conditions).

In order to analyze the effect of traffic consisting of different types of vehicle configurations, the following assumptions are made.

1. All traffic can be classified into a finite number of vehicle types.
2. Damage caused by different types of vehicles is cumulative and independent of the order in which the vehicle travels over the pavement.

3. When a vehicle passes over the pavement, all components of the structure (i.e., slabs, subbase, subgrade, LTD) suffer some fatigue damage. The damage suffered by each structural element depends upon the relative magnitude of stresses or strains in that element, and on the fatigue characteristics of the particular element.
4. An endurance curve is known for the concrete and a minimum stress ratio exists, below which no fatigue damage occurs.
5. Fatigue damage due to one application is independent of the previous history of load application (i.e., Miner's law applies—see Miner, 1945).

The fatigue in concrete is commonly quantified by the decay in stiffness of concrete and the amount of cracking. The value of the modulus of elasticity of concrete is modified in accordance with the level of stress and the number of load repetitions, assuming that a flexural endurance curve is known. Also, the relation between the modulus of elasticity, the compressive strength and the flexural strength of concrete are known.

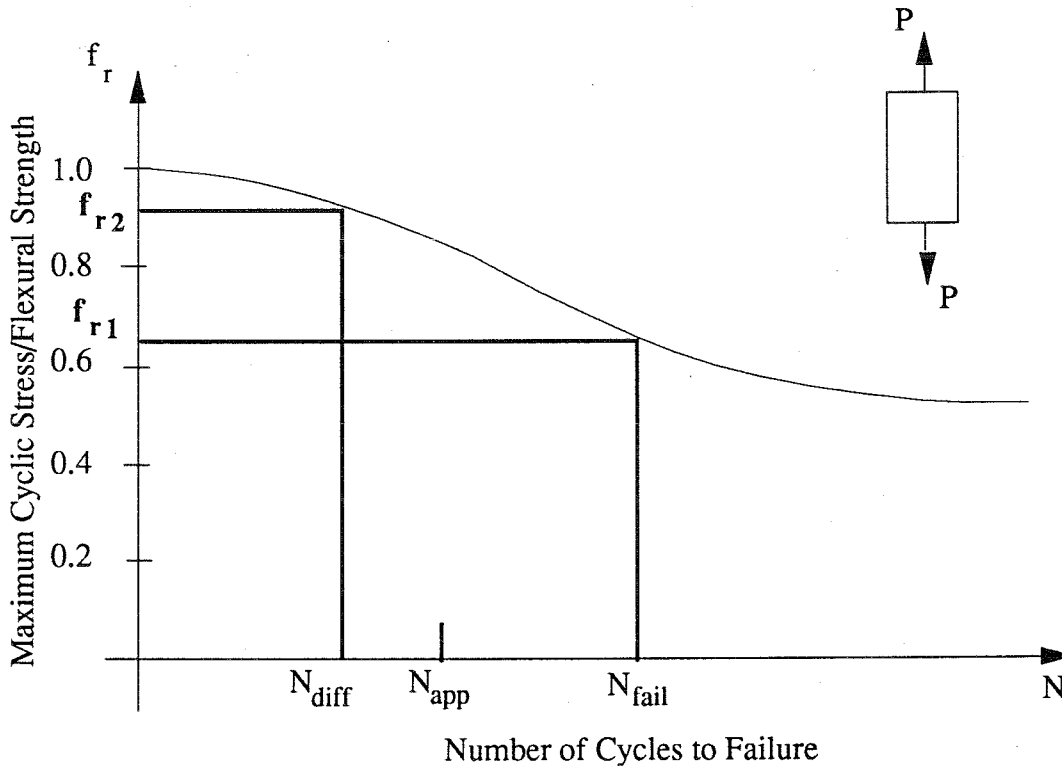


Figure 3-23
Endurance Curve for Concrete in Tension Under Cyclic Loading

Let us assume that the endurance curve of a concrete specimen under constant cyclic load is known, as shown in Figure 3-23. For simplicity let us assume that the specimen consists of an axially loaded concrete cylinder.

Given that the relative stress f_r (which is equal to σ_{max}/σ_r) is the damage parameter, where σ_r is the tensile strength of concrete, three cases are possible:

1. If $f_r \geq 1.0$, then cracking occurs.
2. If $f_{min} \leq f_r \leq 1.0$, then fatigue damage takes place.
3. If $f_r \leq f_{min}$, then no damage takes place.

Let N_{app} be the applied number of repetitions of the load and f_{r1} the applied stress level. The fatigue damage calculation consists of two stages:

1. Check whether the specimen is capable of resisting N_{app} repetition of loads, with a relative stress of f_{r1} , without failure.
2. If no failure has occurred with N_{app} , and if $f_{r1} \geq f_{min}$, calculate the stiffness decay of the material, which is measured as the variation in the value of the modulus of elasticity of concrete.

With the value of f_{r1} , calculate from the endurance curve the number of load repetitions necessary to bring the specimen to failure (i.e., N_{fail}) as shown in Figure 3-23. If the number $N_{fail} \leq N_{app}$, then the material has reached failure due to fatigue and is not able to sustain any further load. Otherwise, the specimen undergoes fatigue damage if $f_{r1} \geq f_{min}$; or if $f_{r1} < f_{min}$, then no fatigue damage occurs. Here:

$$f_{min} \leq f_{r1} \leq 1.0 \text{ and } N_{app} \leq N_{fail}$$

Since Miner's Law applies, the number of load repetitions to cause failure must be the same, disregarding the sequence in which these cycles are applied. To account for this, a value of relative stress corresponding to N_{diff} is calculated from the endurance curve, being N_{diff} —the difference between the cycles necessary to bring the specimen to failure with a relative stress of f_{r1} and the applied number of cycles (i.e., $N_{diff} = N_{fail} - N_{app}$).

With this new value of the relative stress (f_{r2}), and assuming that the maximum stress (σ_{max}) applied to the specimen remains constant, an updated value of the tensile strength of concrete is calculated as

$$\sigma_r' = \frac{\sigma_{max}}{f_{r2}} \quad (13)$$

and with σ_r' a new value of the modulus of elasticity is obtained as

$$E_c' = E_c'(\sigma_r') \quad (14)$$

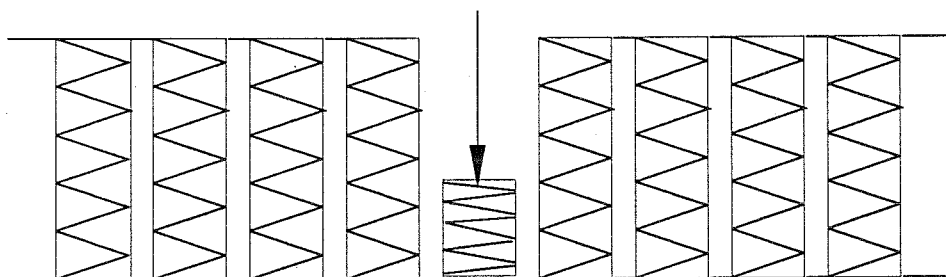
By updating the value of the tensile strength of concrete, we are assuring that the material will fail when an additional N_{diff} cycles are applied, under the assumption that the maximum stress remains constant. The initial maximum number of cycles that the structure can receive does not change.

Subgrade Model

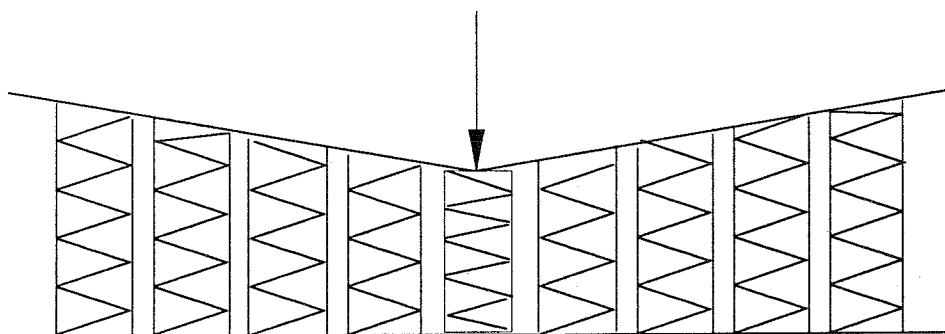
Finite Element Model

There are two ways of representing the subgrade: as an elastic liquid foundation, also known as a Winkler foundation; or as an elastic half space. The Winkler subgrade is unable to transfer shear stresses. This means that the reaction at any point of the base (vertical pressure) is proportional only to the deflection of the slab at that point. This is different from the elastic solid representation of the foundation, where the subgrade is capable of transferring shear stresses. In the latter case, the reaction at a point on the base depends not only on the deflection of the slab at that point, but also on the deflection of adjacent points. Figure 3-24 illustrates the two representations of the subgrade.

These soil representations assume that only compressive stresses are resisted, whereas no resistance is offered under tensile stress. The values of the modulus of subgrade reaction are deflection dependent (i.e., they are resilient values).



a) Winkler Foundation



b) Elastic Solid Foundation

Figure 3-24
Types of Subgrade Representation

This study assumes that the subgrade behaves as a Winkler foundation. The constant of proportionality between the slab deflection and the reaction is known as the modulus of subgrade reaction k , defined as the pressure necessary to produce a unit deformation of the subgrade determined through plate loading with a standard plate radius of 15 inches (Ullidtz, 1987).

Pumping Representation

Pumping is defined as decay in the subgrade support due to the ejection of fine material, with water, as traffic loads are applied. The pumping of fine material produces zones of low bearing capacity underneath the concrete slab, modifying the support conditions. After severe pumping, voids are created with consequent loss of subgrade support.

Water can be accumulated in initial voids and ejected through cracks and joints when loading is applied. The initial voids can be a consequence of temperature effects, or plastic deformation of the subgrade.

The amount of material pumped depends on factors such as structural properties of the pavement, magnitude and number of load applications, climatic conditions, and type of material used in the subgrade.

Field observations indicate that the initial pumping is most severe at the edges of the pavement and along the joints (Gulden, 1983; Yoder and Witzak, 1975). Cracks form once the support condition has deteriorated beyond a critical limit, providing additional sites for pumping to occur.

A pumping model developed at Purdue University (Larralde, 1984) is used. This model accounts for the effects of structural properties of the concrete pavement and the amount and type of traffic imposed. Climatic conditions and granular composition of the subgrade are not accounted for. Additional data on pumping development could provide the necessary information to account for such factors. It is important to mention that the subgrade material used at the AASHO Road Tests were non-treated, with a high percentage of fine material.

The pumping model is defined in terms of the total energy of deformation imposed on the pavement and a normalized Pumping Index. The energy of deformation is defined as

$$E = \sum_{i=1}^n k_i A_i \omega_i^2 \quad (15)$$

using the following definitions:

- E energy of deformation due to one application of loading (inches-pounds)
- ω_i vertical deflection in excess of ω_{\min} (inches)
- ω_{\min} minimum vertical deflection necessary to induce pumping; in this model it is taken as 0.020 inches (20 mils)
- A_i area of the slab associated with ω_i
- k_i subgrade modulus associated with location of ω_i
- n number of the location at which $\omega_i > \omega_{\min}$

The Pumping Index is defined as the volume of material pumped out per unit length of pavement. To account for the fact that different lengths of slabs were used during the AASHO Road Test (ASSHO, 1962), the pumping indices were normalized by dividing their values by the number of joints per 100 feet.

The relation between the applied total deformation energy, after a given number of load repetitions, and the normalized pumping index is given by

$$\text{NPI} = e^\alpha \quad (16a)$$

where

$$\alpha = 1.652 \log_{10} \left(\frac{E_t}{10000} \right) - 2.884 \quad (16b)$$

using the following definitions:

- NPI normalized Pumping Index (inches²)
- E_t total deformation energy (inches-pounds)
 = $E * (\text{number of load applications})$
- E energy of deformation due to one application of load

Dowel Bar Model

Dowel Representation

The basic representation of the dowel bars is that of a thick beam, allowing for shear deformation of the beam. The beam is assumed to have two degrees of freedom per node, a vertical displacement and a rotation. A graphical representation of the model is shown in Figure 3-25.

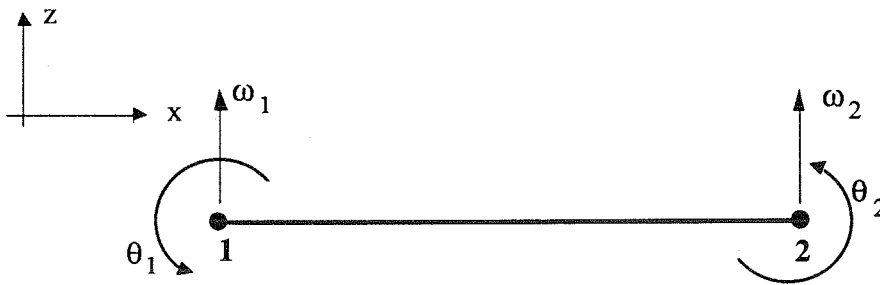


Figure 3-25
Beam Element: Local Node Numbering and Degrees of Freedom

The beam stiffness matrix is evaluated through the use of an isoparametric finite element formulation. For this stiffness matrix, the bending contribution is fully integrated, whereas the shear contribution is under-integrated to avoid shear-locking problems. The resulting stiffness matrix is

$$[K] = \begin{bmatrix} \beta & \beta \frac{L}{2} & -\beta & \beta \frac{L}{2} \\ \beta \frac{L}{2} & (\alpha + \beta \frac{L^2}{4}) & -\beta \frac{L}{2} & (-\alpha + \beta \frac{L^2}{4}) \\ -\beta & -\beta \frac{L}{2} & \beta & -\beta \frac{L}{2} \\ \beta \frac{L}{2} & (-\alpha + \beta \frac{L^2}{4}) & -\beta \frac{L}{2} & (\alpha + \beta \frac{L^2}{4}) \end{bmatrix} \quad (17)$$

where

$$\alpha = \frac{EI}{L} \quad (18a)$$

$$\beta = \frac{kGA}{L} \quad (18b)$$

using the following definitions:

- E modulus of elasticity
- I moment of inertia
- L length
- A cross sectional area
- G shear modulus, given by

$$G = \frac{E}{2(1 + \nu)} \quad (19)$$

- ν Poisson's ratio

Further modifications have to be performed on the above stiffness matrix in order to model the behavior of a dowel bar embedded in the concrete slab. When load is applied to the dowel bar there exists a relative deformation between the dowel bar and the surrounding concrete slab, which further increases displacements that would be obtained with the beam stiffness matrix alone. Figure 3-26 represents these additional deformations.

Timoshenko and Lessels (1925) modeled the embedded portion of the dowels as a beam resting on an elastic foundation. Based on these results, Bradbury (1938) and Frieberg (1940) presented mathematical analysis of dowel design. Hetenyi (1946) gives a rather complete development of the theory of beams supported on elastic foundations.

When the embedded portion of the dowel bar is considered as a beam on an elastic foundation and a shear loading is applied as shown in Figure 3-27a, it can be shown (Hetenyi, 1946) that the deflection and rotation at the face of the slab are given by:

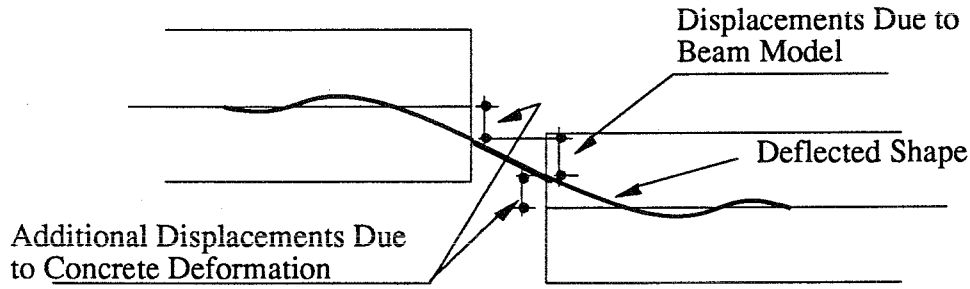


Figure 3-26
Relative Deformations Between Dowel Bar and Concrete Slab

$$\omega_o^p = \frac{P}{2 \eta^3 EI} \quad (20a)$$

$$\theta_o^p = -\frac{P}{2 \eta^2 EI} \quad (20b)$$

where

ω_o^p deflection of dowel bar at concrete slab due to applied shear loading

θ_o^p rotation of dowel bar at concrete slab face due to applied shear loading
using the following definitions:

P applied shear loading

η modulus of relative stiffness between concrete slab and dowel bar, given by

$$\eta = \sqrt[4]{\frac{H \phi}{4 E I}} \quad (21)$$

H modulus of concrete-dowel interaction

ϕ dowel diameter

E modulus of elasticity of dowel bar

I moment of inertia of dowel bar

In the same way, it can be shown that when a moment loading is applied on the dowel bar, the deflection and rotation at the face of the concrete slab (see Figure 3-27b) are given by

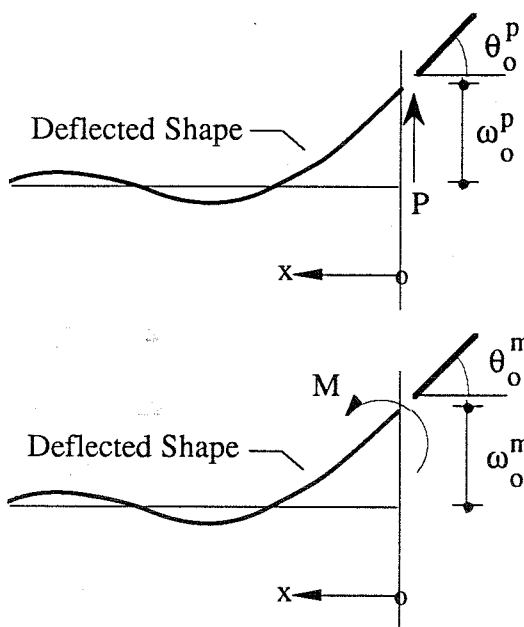
$$\omega_o^m = \frac{M}{2 \eta^3 EI} \quad (22a)$$

$$\theta_o^m = -\frac{M}{2 \eta^2 EI} \quad (22b)$$

using the following definitions

- ω_o^m deflection of dowel bar at concrete slab due to applied moment loading
- θ_o^m rotation of dowel bar at concrete slab face due to applied moment loading
- M applied moment loading

Therefore, the relative deformation between the dowel bar and the concrete slab can be represented by a lengthless "spring" element, where the stiffness matrix is given by:



$$[K]_{\text{spring}} = 2 \eta E I \begin{bmatrix} 2\eta^2 & \eta & -2\eta^2 & -\eta \\ \eta & 1 & -\eta & -1 \\ -2\eta^2 & -\eta & 2\eta^2 & \eta \\ -\eta & -1 & \eta & 1 \end{bmatrix} \quad (23)$$

Finally, the dowel bar can be represented by an element composed of a beam element (to account for the behavior across the joint) and two generalized springs (as described above) attached to the ends of the beam. This model is represented in Figure 3-28.

Figure 3-27
Relative Deformation Between Dowel and Concrete Slab:
(a) Under Shear Loading; and
(b) Under Moment Loading

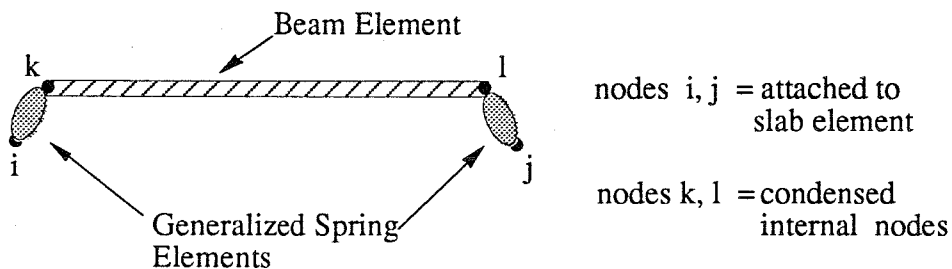


Figure 3-28
Finite Element Idealization of Dowel Bars

Effect of Repetitive Loading

The effect of repetitive loading on the load transfer efficiency of dowels has not been subject to extensive research. Nevertheless, past research has been able to characterize some of the variables affecting load transfer efficiency (Teller and Sutherland, 1938; Sutherland and Cashell, 1945).

The most comprehensive study was carried out by Teller and Cashell (1958) where the effects of different variables such as joint width, dowel diameter, dowel length, and number of load repetitions were studied. From these results it was concluded that there exists an exponential relation between dowel diameter and load-transfer capacity; that the decrease in joint width increases the load-transfer capacity. But the most relevant result is that the load transfer efficiency of the bars is in direct relation to the initial dowel looseness, which increases with the number of load applications.

Based on the results of Teller and Cashell, Larralde (1984) developed an equation using linear regression analysis and including several of the variables affecting the load transfer efficiency. The expression is given by

$$R_f = \frac{0.0457 \log_{10}(N)}{0.268 + 1.123 f_{rb}} \quad (24)$$

using the following definitions:

- R_f reduction factor
- N number of load repetitions
- f_{rb} relative loading acting on the dowel, and given by

$$f_{rb} = \frac{P_d}{P_c} \quad (25)$$

- P_d shear load acting on dowel
- P_c cracking load (Marcus, 1951), given by

$$P_c = \frac{3}{2} \frac{\phi (h - \phi)}{1 + \frac{w}{l_\phi}} f_t \quad (26)$$

- ϕ dowel diameter
- l_ϕ embedded length of dowel
- h thickness of the slab
- f_t tensile strength of concrete

The reduction factor affects the value of η , or modulus of relative stiffness between concrete slab and dowel bar, as shown in equation 21.

Examples of Pavement Model Formulation

Example 1

This example demonstrates the effects of the different components of the pavement model. It consists of a single slab, with dimensions as specified in Figure 3-29a, which has been discretized using elements with a configuration similar to the one presented in Figure 3-29b. Two point loads are applied at the edge representing the joint. The magnitude of the load is taken as 22,000 pounds, representing the equivalent effect of a rear tandem axle.

The example is divided in two parts. In the first, only fatigue effects are considered; pumping and temperature gradient are neglected. The second accounts for only the effects of pumping of the subgrade, whereas fatigue and temperature effects are neglected.

The analysis is performed for a series of tandem axle load replications. The response is evaluated after 1, 1×10^5 , 2.5×10^5 , 5.0×10^5 , 7.5×10^5 , 1×10^6 , 1.25×10^6 , 1.50×10^6 , and 1.75×10^6 tandem axle load replications.

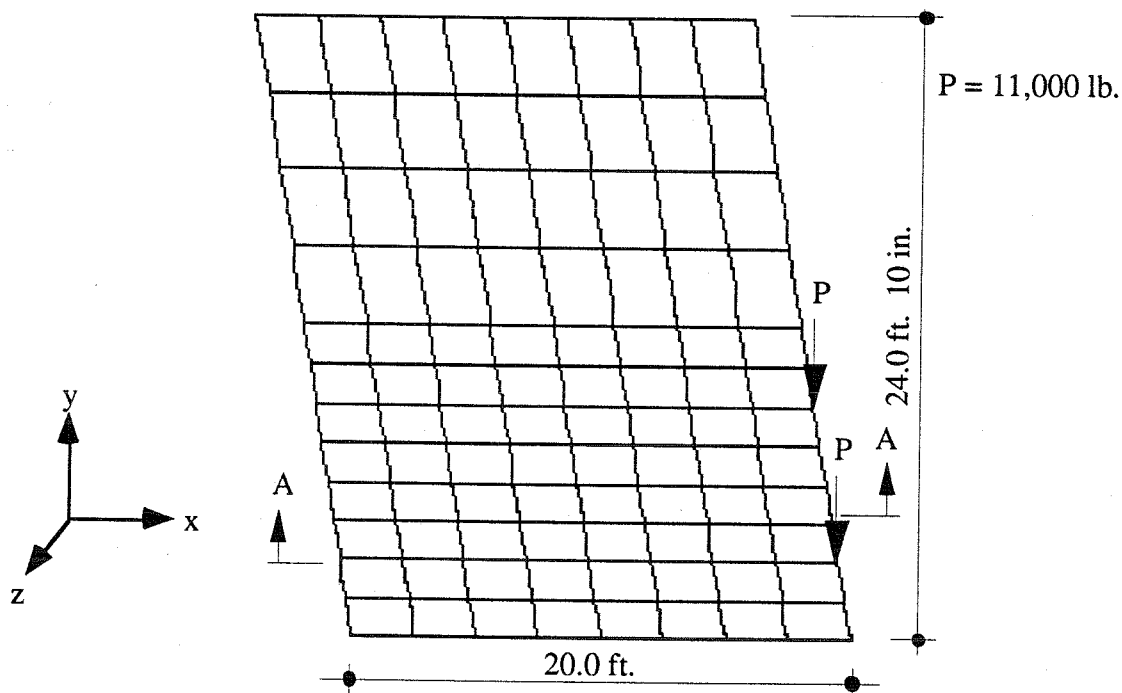


Figure 3-29a
Slab Geometry and Loads Used in Example 1

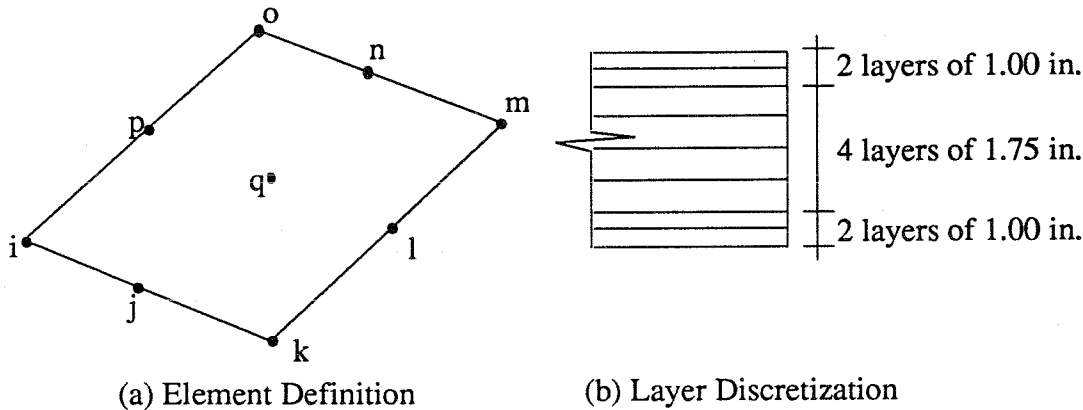


Figure 3-29b
Element Configuration and Layer Discretization for Example 1

Results

Fatigue Damage

Figure 3-30 presents a plot of the displacement along a selected path along the slab, A-A in Figure 3-29a, for five different levels of tandem axle load replications. The actual values of the displacements do not differ greatly between cases, even though the range of the levels of tandem axle load replications is significantly large.

Figure 3-31 presents a plot of the same displacements, but is normalized with respect to values obtained after one load application. Here it can be observed that the relative increase in deflection due to fatigue damage only is very small. Nevertheless, the model predicts the beginning of slab cracking after 1.5×10^5 load applications.

Figures 3-32 to 3-35 present the stress distribution in the x- and y-directions after 1×10^5 and 1.75×10^5 load applications. It can be observed that, for this particular example, the stresses do not seem to differ significantly.

Pumping Damage

Figure 3-36 presents the distribution of deflections along path A-A, for different levels of tandem axle load replications. It can be observed that pumping has a large influence on the displacement values. After 750,000 load replications, the relative value of the displacement under the point of application is approximately six times the deflection observed after one application.

Figure 3-37 shows a plot of the volume of material pumped from underneath the slab versus the level of axle load replications. It should be emphasized that the slab fails when the load is applied with the support conditions that would prevail after 1,000,000 load repetitions. This implies that the maximum number of load replications that this structure would support lies between 750,000 and 1,000,000.

Figures 3-38 to 3-42 present a plot of the void depth distribution, caused by pumping, after different levels of load replications. The model predicts a void propagation which is consistent with field observations.

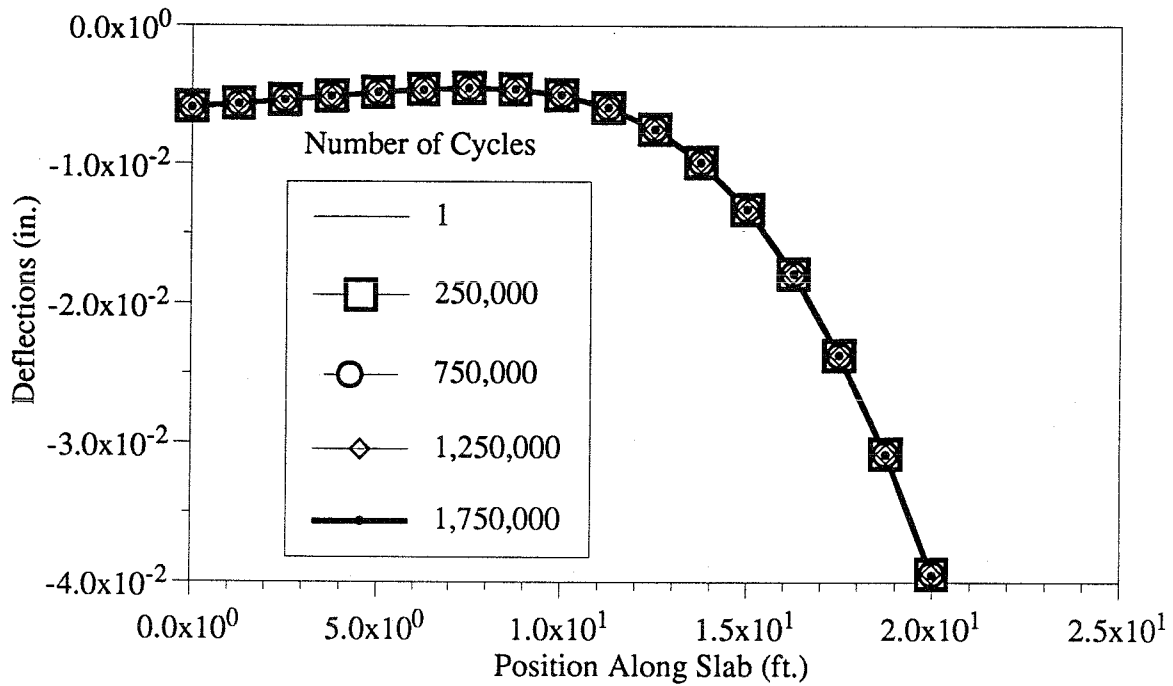


Figure 3-30
Displacement Along Path A-A
for Different Numbers of Cycles (Fatigue Only)

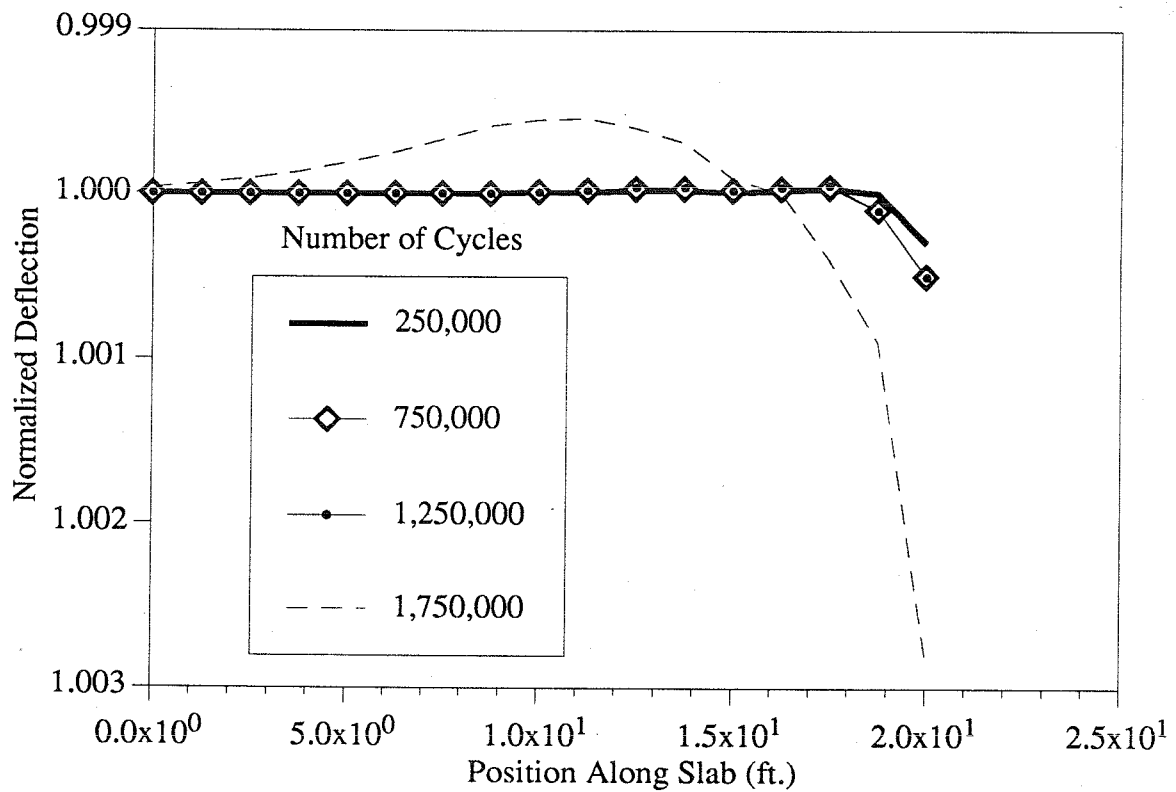


Figure 3-31
Normalized Displacements Under Fatigue Analysis

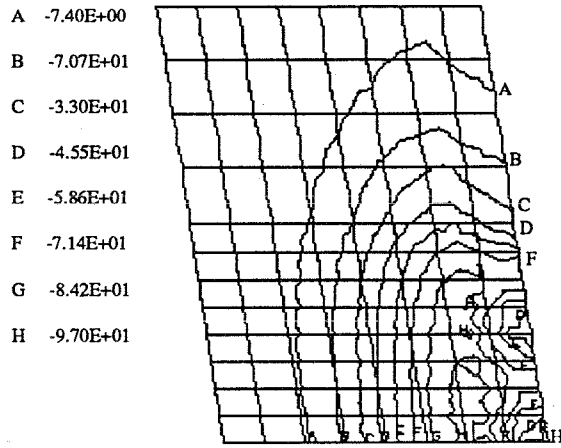


Figure 3-32a
Stress Distribution, in X-Direction,
At Bottom of Slab After One Load Repetition:
Fatigue Damage Only

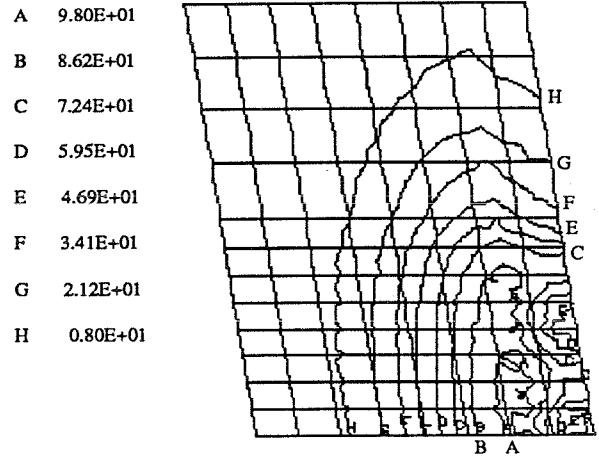


Figure 3-32b
Stress Distribution, in X-Direction,
At Top of Slab After One Load Repetition:
Fatigue Damage Only

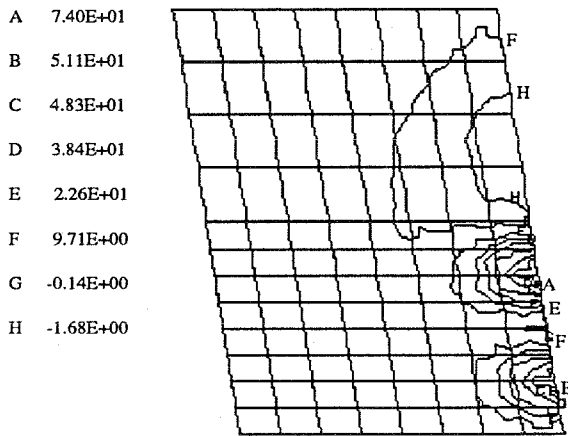


Figure 3-33a
Stress Distribution, in Y-Direction,
At Bottom of Slab After One Load Repetition:
Fatigue Damage Only

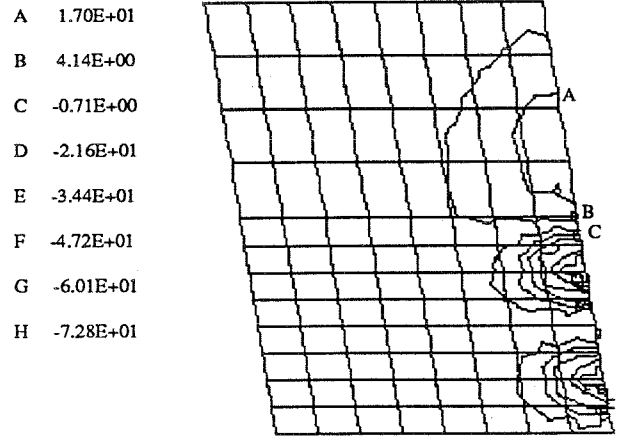


Figure 3-33b
Stress Distribution, in Y-Direction,
At Top of Slab After One Load Repetition:
Fatigue Damage Only

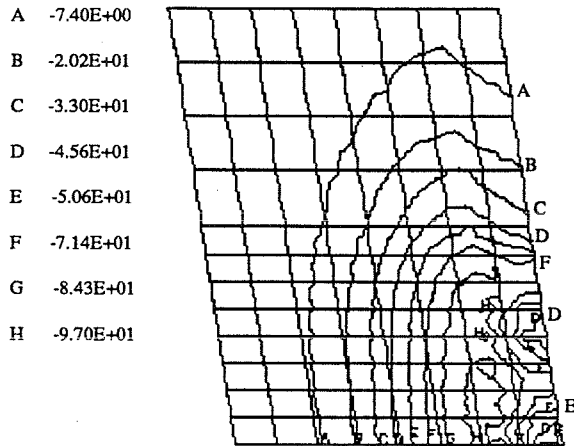


Figure 3-34a
Stress Distribution, in X-Direction,
At Bottom of Slab After 1,250,000 Load Repetitions:
Fatigue Damage Only

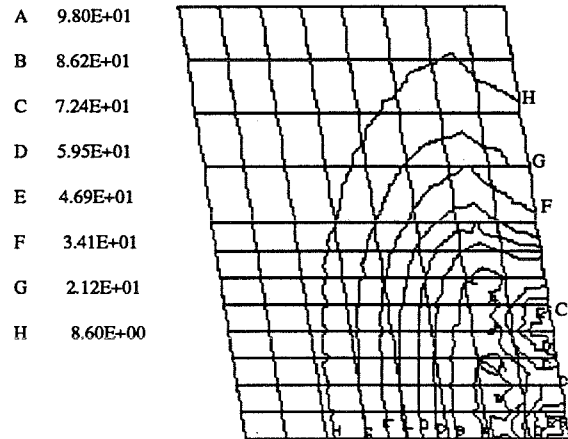


Figure 3-34b
Stress Distribution, in X-Direction,
At Top of Slab After 1,250,000 Load Repetitions:
Fatigue Damage Only

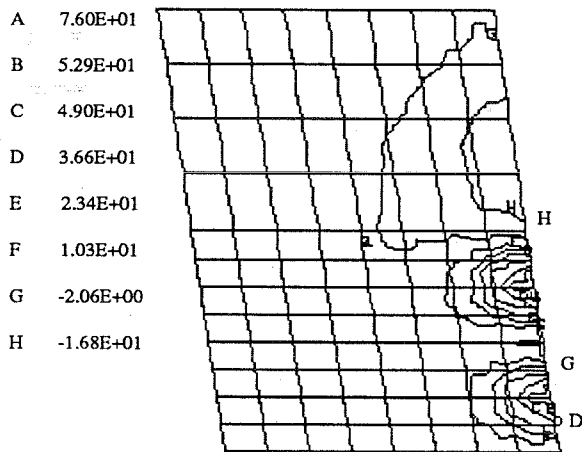


Figure 3-35a
Stress Distribution, in Y-Direction,
At Bottom of Slab After 1,250,000 Load Repetitions:
Fatigue Damage Only

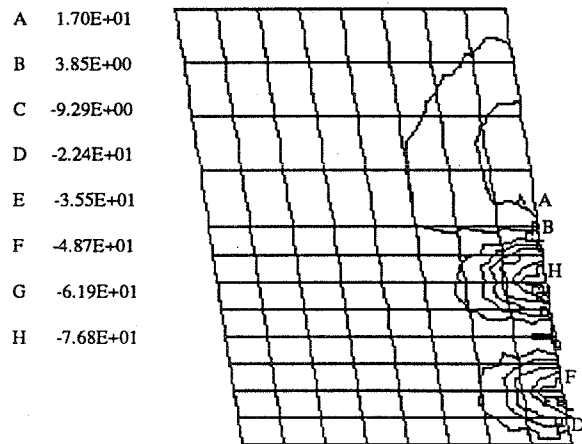


Figure 3-35b
Stress Distribution, in Y-Direction,
At Top of Slab After 1,250,000 Load Repetitions:
Fatigue Damage Only

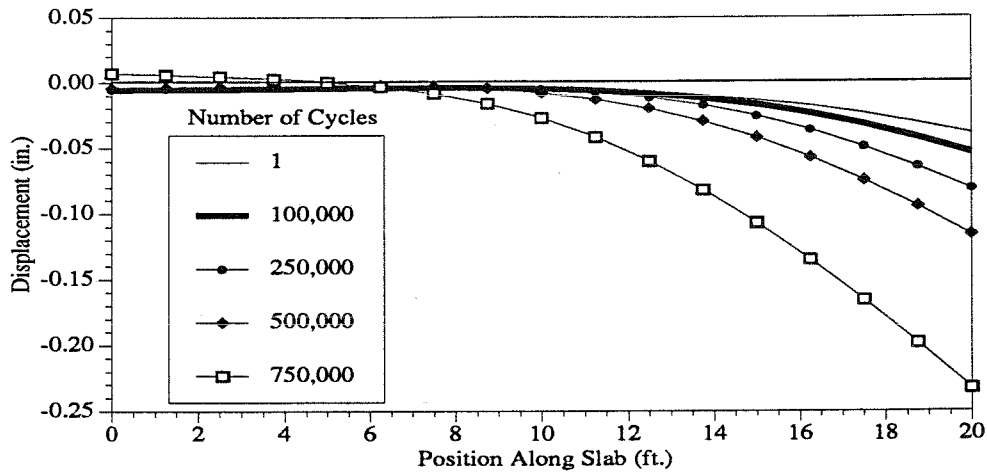


Figure 3-36
Displacements Along Path A-A for Different Numbers of
Load Applications For Pumping Damage Analysis

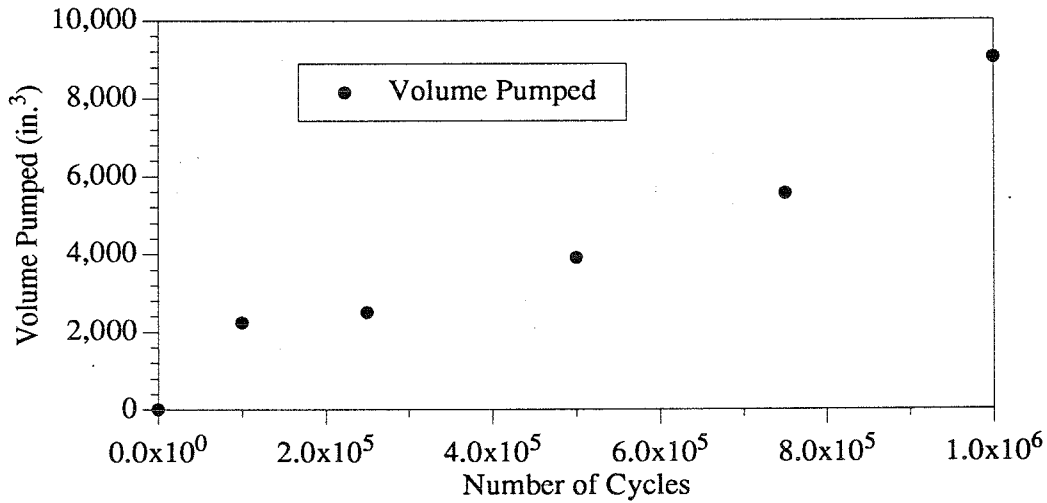


Figure 3-37
Volume of Material Ejected For Different
Numbers of Load Applications During Pumping Damage Analysis

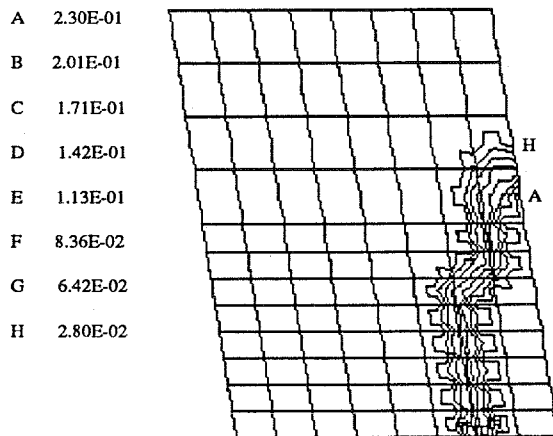


Figure 3-38
Void Distribution Due to Pumping
After 100,000 Load Repetitions

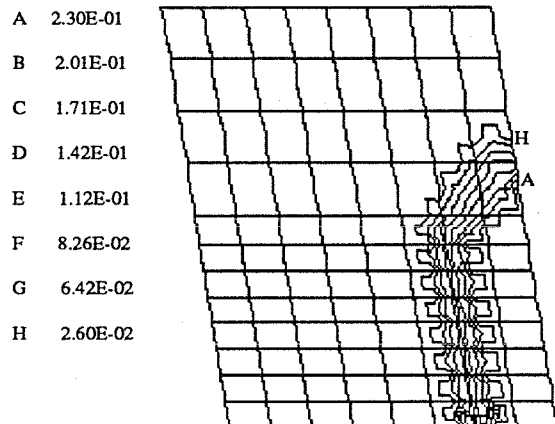


Figure 3-39
Void Distribution Due to Pumping
After 250,000 Load Repetitions

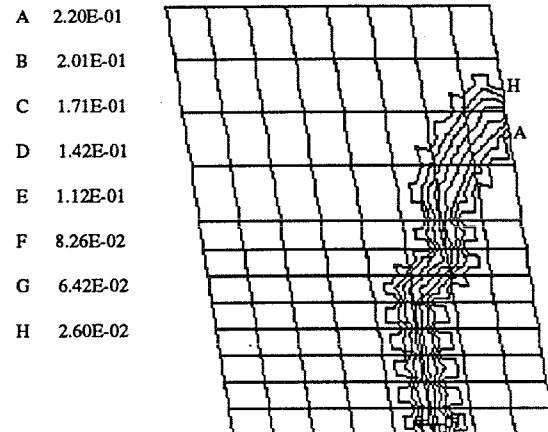


Figure 3-40
Void Distribution Due to Pumping
After 500,000 Load Repetitions

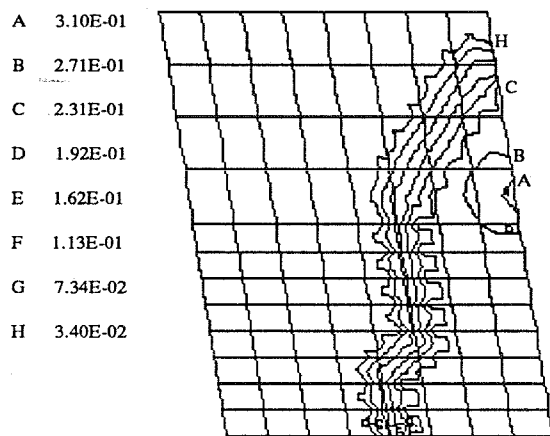


Figure 3-41
Void Distribution Due to Pumping
After 750,000 Load Repetitions

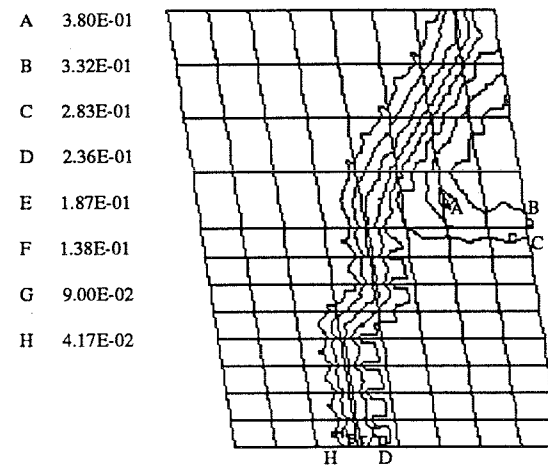


Figure 3-42
Void Distribution Due to Pumping
After 1,000,000 Load Repetitions

Figures 3-43 to 3-48 represent the distribution for the maximum and minimum principal stresses, at top and bottom of the slab, for different levels of tandem axle load replications.

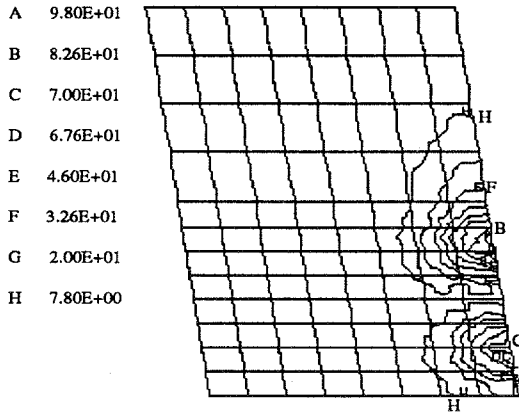


Figure 3-43a
Maximum Principal Stress Distribution
At Bottom of Slab After One Load Repetition:
Pumping Damage Only

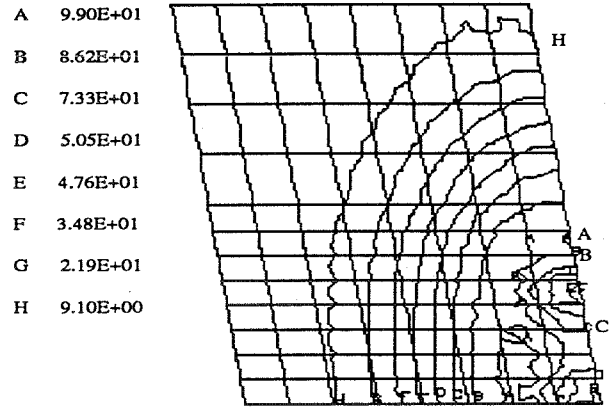


Figure 3-43b
Maximum Principal Stress Distribution
At Top of Slab After One Load Repetition:
Pumping Damage Only

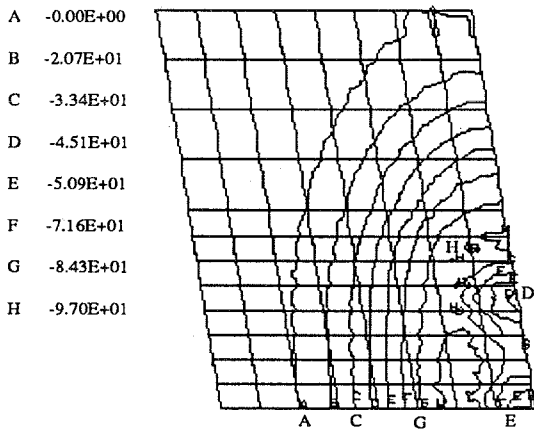


Figure 3-44a
Minimum Principal Stress Distribution
At Bottom of Slab After One Load Repetition:
Pumping Damage Only

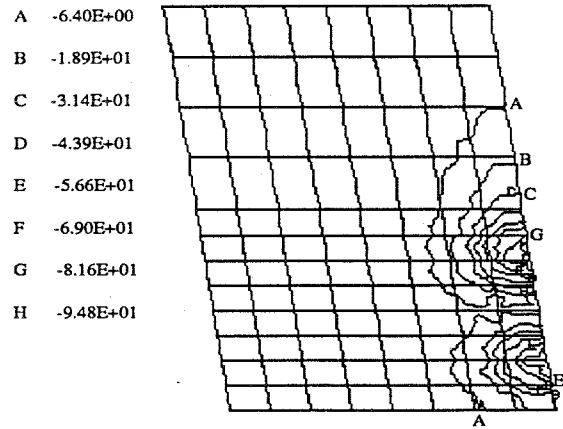


Figure 3-44b
Minimum Principal Stress Distribution
At Top of Slab After One Load Repetition:
Pumping Damage Only

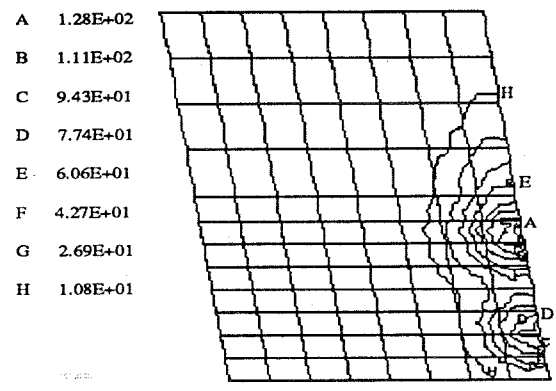


Figure 3-45a
Maximum Principal Stress Distribution
At Bottom of Slab After 250,000 Load Repetitions:
Pumping Damage Only

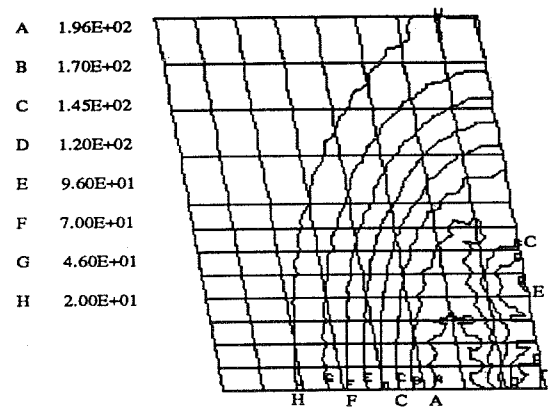


Figure 3-45b
Maximum Principal Stress Distribution
At Top of Slab After 250,000 Load Repetitions:
Pumping Damage Only

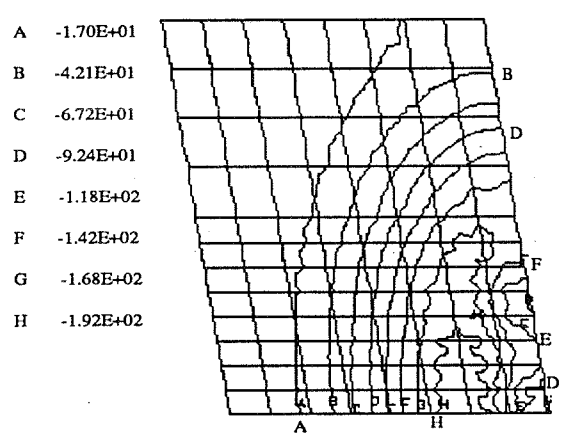


Figure 3-46a
Minimum Principal Stress Distribution
At Bottom of Slab After 250,000 Load Repetitions:
Pumping Damage Only

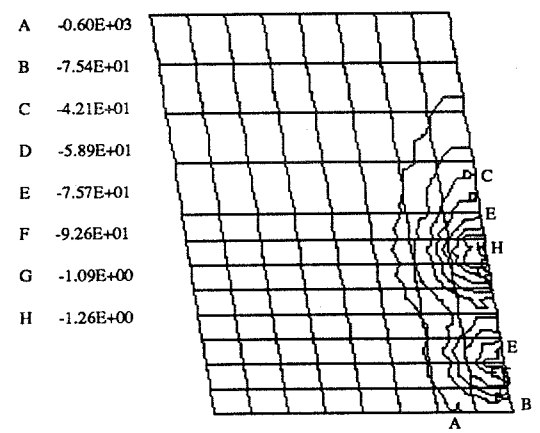


Figure 3-46b
Minimum Principal Stress Distribution
At Top of Slab After 250,000 Load Repetitions:
Pumping Damage Only

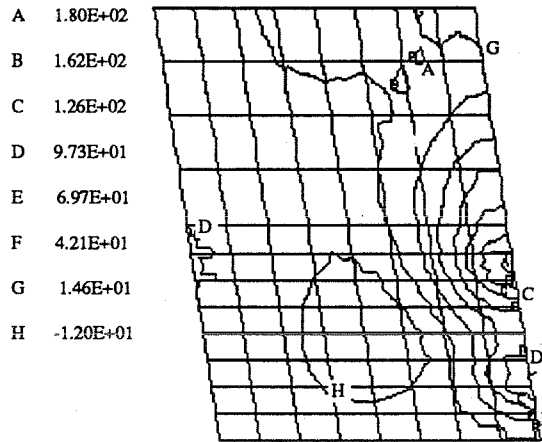


Figure 3-47a
Maximum Principal Stress Distribution
At Bottom of Slab After 750,000 Load Repetitions:
Pumping Damage Only

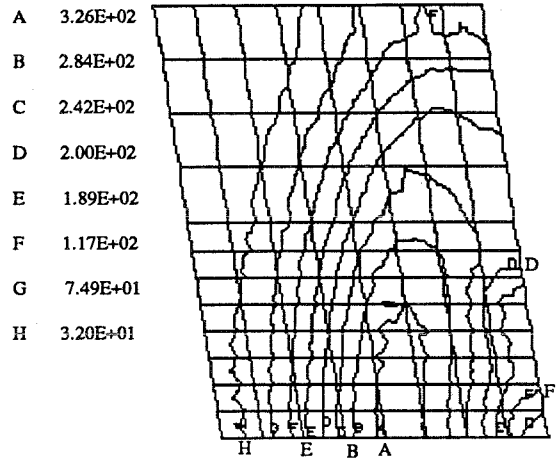


Figure 3-47b
Maximum Principal Stress Distribution
At Top of Slab After 750,000 Load Repetitions:
Pumping Damage Only

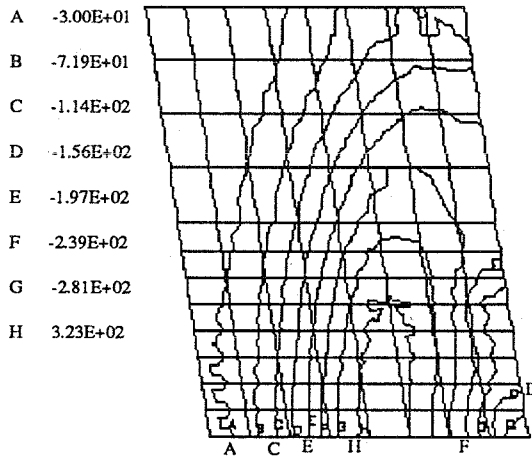


Figure 3-48a
Minimum Principal Stress Distribution
At Bottom of Slab After 750,000 Load Repetitions:
Pumping Damage Only

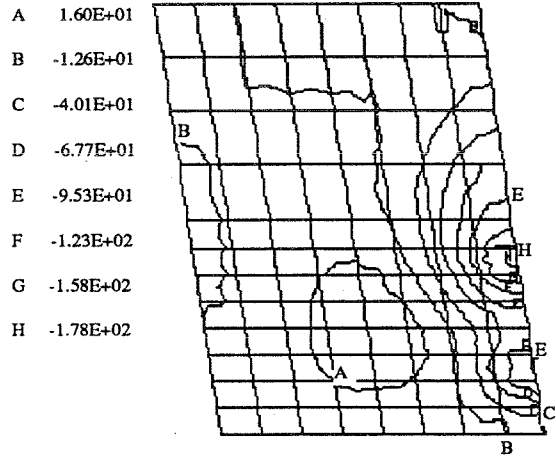


Figure 3-48b
Minimum Principal Stress Distribution
At Top of Slab After 750,000 Load Repetitions:
Pumping Damage Only

Example 2

This problem presents the effects on displacements of different gradients of temperature through the slab pavement. The pavement configuration selected for this problem is shown in Figure 3-49 and consists of two slabs connected by dowel bars. The slabs are of similar dimensions and characteristics as the one used in Example 1. The dowel consists of steel bars of 1.5 inches in diameter and placed every 12.0 inches along the joint.

Three temperature gradients were selected: 1.5, 0.0 and -1.5 degrees Fahrenheit per inch of thickness of slab (F/in). Again, a total load of 22,000 pounds was applied at two nodal points, representing the equivalent effect of a tandem axle. Analysis is performed for a series of load applications. The response is evaluated after $1, 1 \times 10^5, 2.5 \times 10^5, 5.0 \times 10^5, 7.5 \times 10^5, 1 \times 10^6$ and 1.25×10^6 load applications.

Results

Figure 3-50 presents a plot of the displacements which were obtained after the slabs were submitted to temperature gradients of value +1.5 and -1.5 F/inch. If more than two slabs were used, the upward deflections observed under a temperature gradient of -1.5 F/inch would not exist due to continuity.

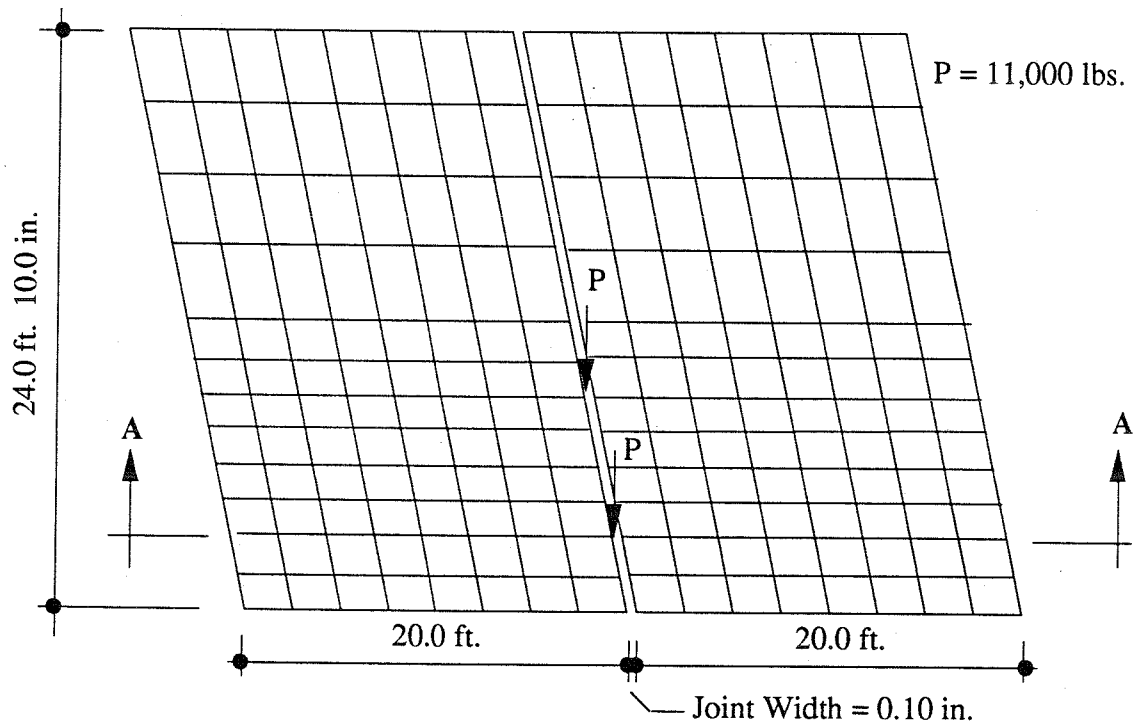


Figure 3-49
Slab Configuration Used in Example 2

Figures 3-51 to 3-53 present plots of the displacements that were calculated for different numbers of load applications and a fixed value of the temperature gradient. For a temperature gradient of value 0.0 F/inch and +1.5 F/inch the large increase in deflections is due to pumping of the subgrade material. The negative temperature gradient had no material pumped and the difference in deflections is due to fatigue damage.

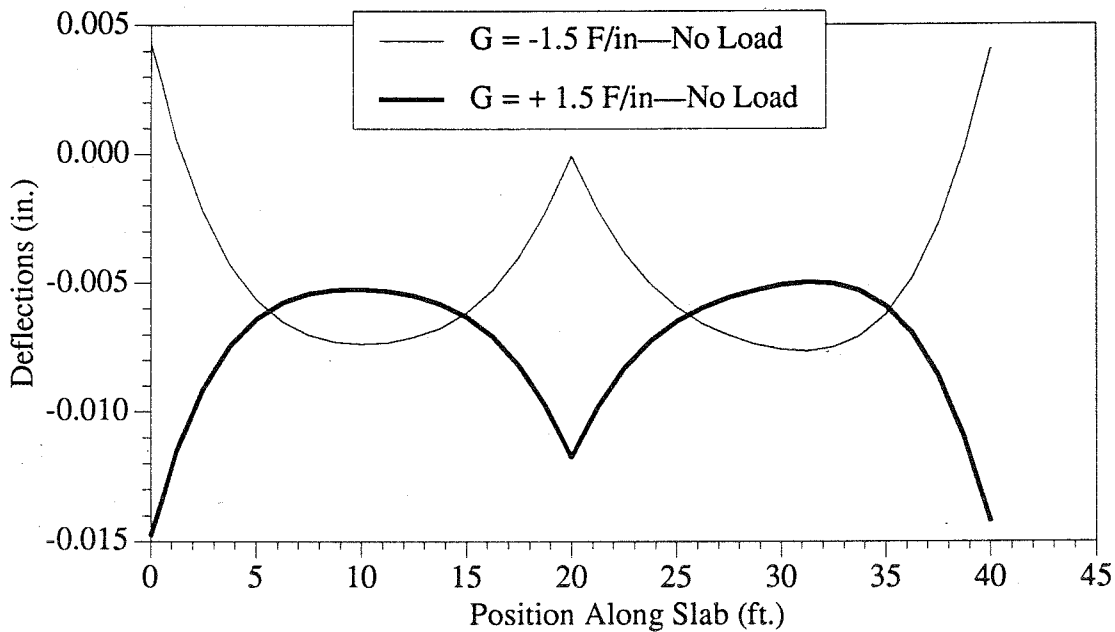


Figure 3-50
Calculated Deflection for Different Gradients of Temperature

The effects of temperature variation, pumping of subgrade material, and fatigue of concrete and dowel can be further observed in Figures 3-54 to 3-57. Each of these figures presents a plot of displacements after a given number of load applications and for the three different temperature gradients.

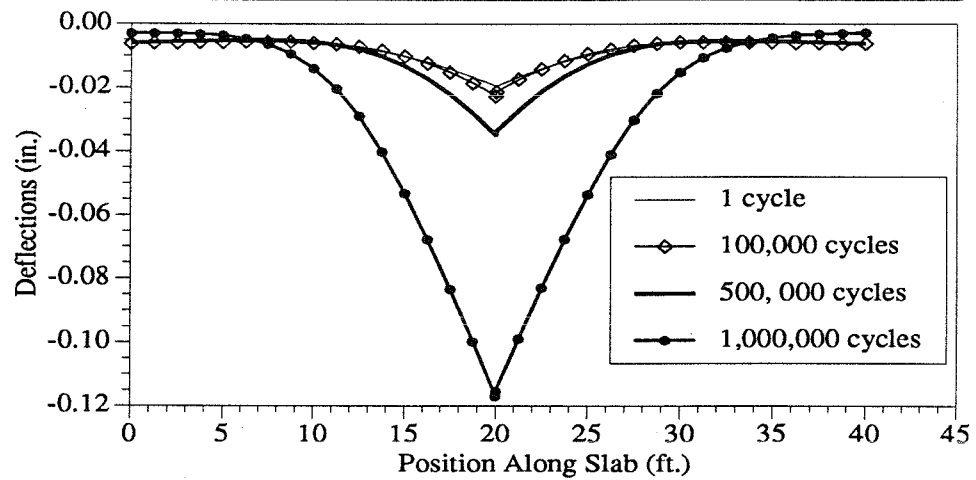


Figure 3-51
Displacements Calculated with a Temperature Gradient of 0.0 F/in.

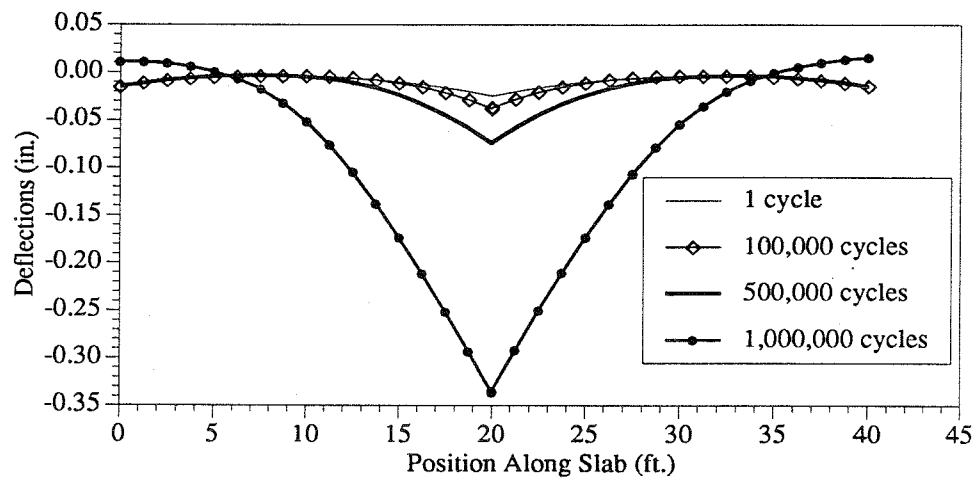


Figure 3-52
Displacements Calculated with a Temperature Gradient of +1.5 F/in.

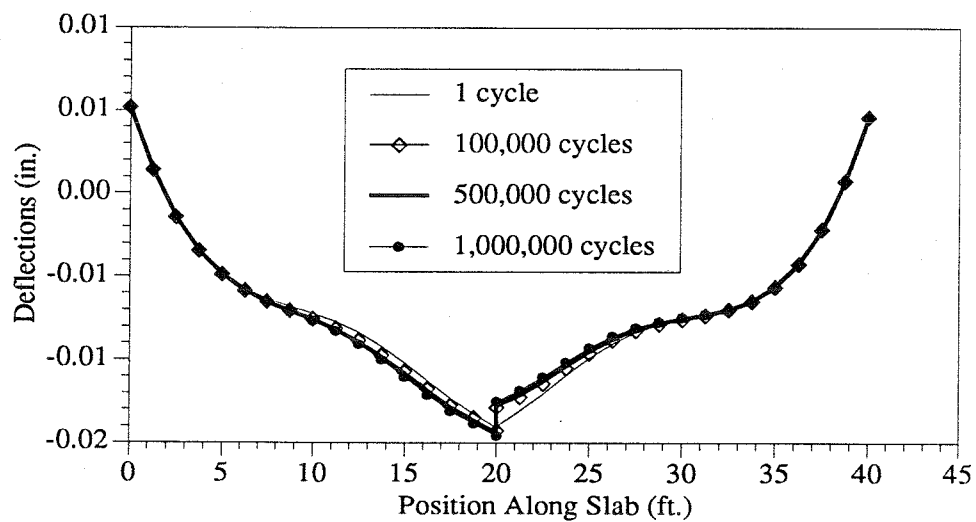


Figure 3-53
Displacements Calculated with a Temperature Gradient of -1.5 F/in.

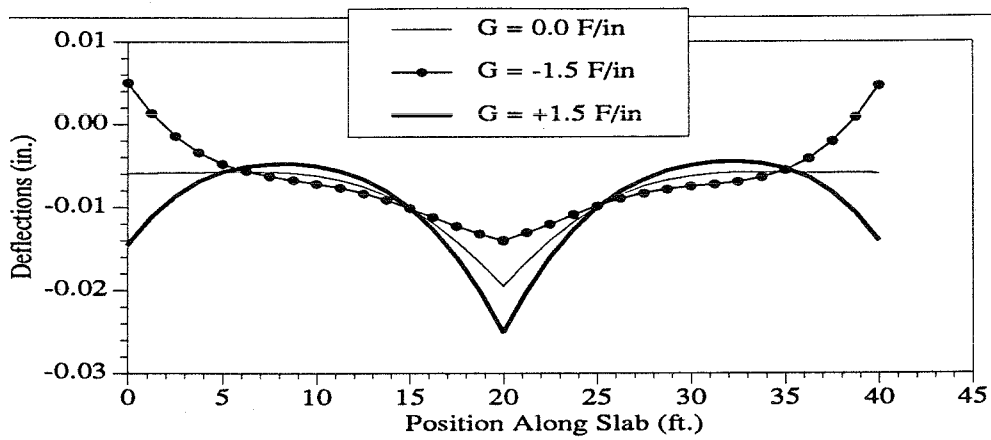


Figure 3-54
Effect of Temperature Gradient on Displacements
After One Load Application

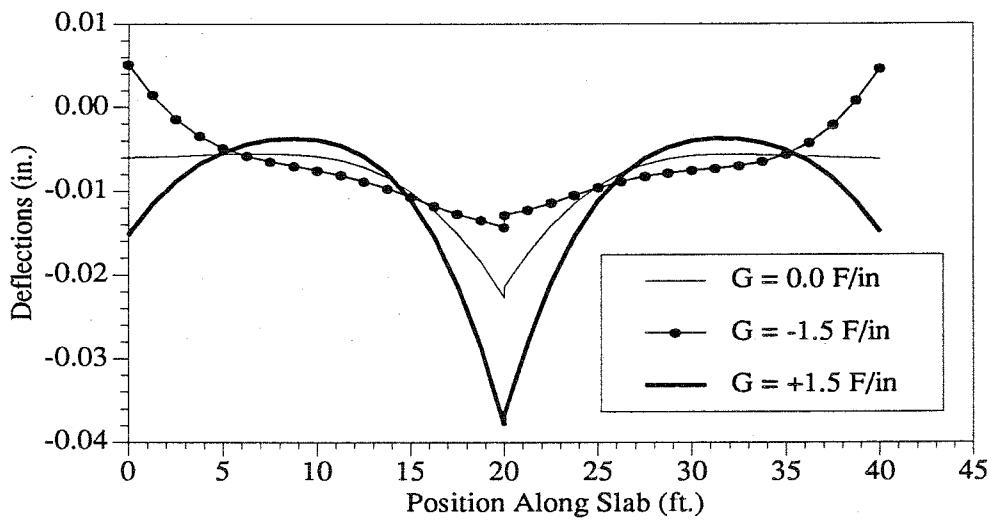


Figure 3-55
Effect of Temperature Gradient on Displacements
After 100,000 Load Applications

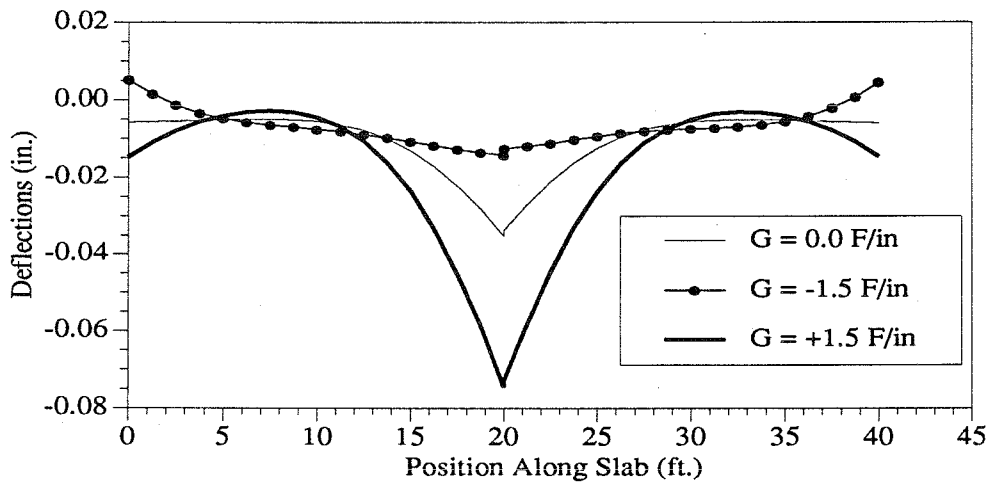


Figure 3-56
Effect of Temperature Gradient on Displacements
After 500,000 Load Applications

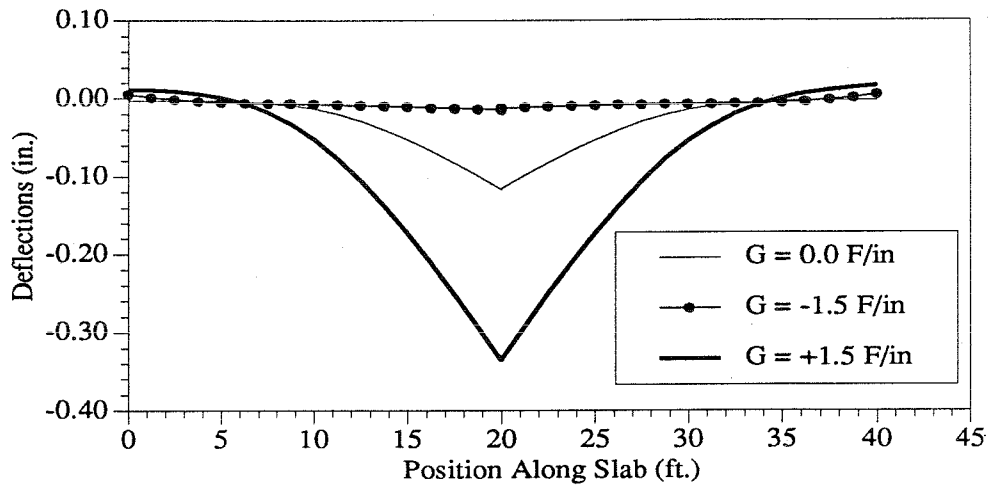


Figure 3-57
Effect of Temperature Gradient on Displacements
After 1,000,000 Load Applications

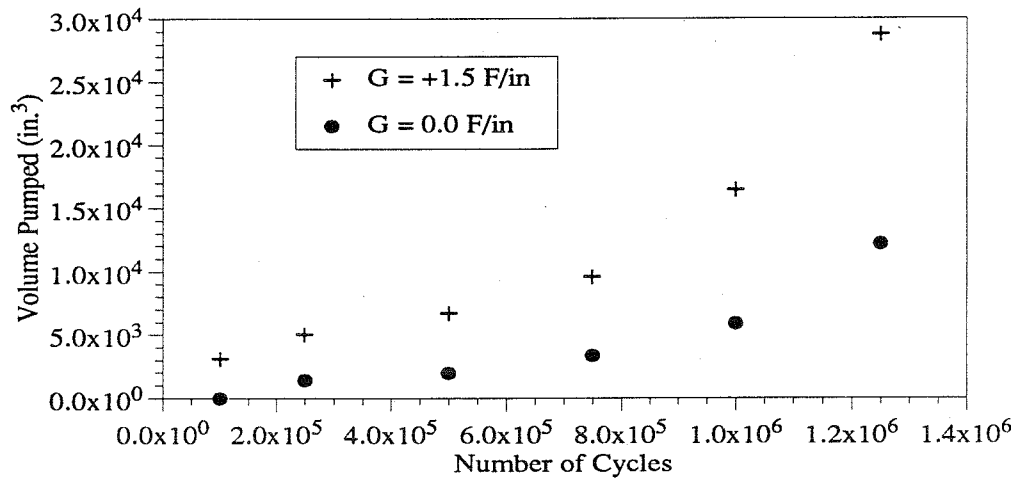


Figure 3-58
Effect of Temperature Gradient in Pumped Material
For Different Numbers of Load Applications

Figure 3-58 shows the relationship between the material pumped and the number of load applications. When a negative gradient was used, the resulting deflections were small and no pumping was predicted. This was not the case for $G = 0.0$ F/inch and $G = +1.5$ F/inch, as can be observed in Figure 3-58. It must be remembered that the pumping model is based on the slab's displacement field, which accounts for the increasing difference in material pumped for increasing number of load applications.

4. Integrated Software Environment

Introduction

The two previous sections of this report have described models used for simulation of alternate truck configurations and estimation of dynamic loads, stress and deflection analysis of pavements, and pavement damage prediction. These models are implemented in separate computer programs to preserve both modularity and ease of development. Input data is read from one set of files and the resulting data is output to a new set of files. Thus, the results of one program may become the input data used by a subsequent sequential modeling process. For example, the axle and wheel forces obtained from the truck simulation program are used by the finite element program as nodal force data. Several additional pre- and post-processing programs are needed to minimize user input requirements and allow rapid interpretation of results. This section describes the integrated software environment that was developed during the course of this project. It should be emphasized that the software structure is still evolving and will be modified slightly before final delivery.

The major components of the software environment are shown in Figure 4-1. All programs are implemented on an Apple Macintosh II fx Personal Workstation. The two front end programs are based on HyperCard, whereas the main simulation programs are written in

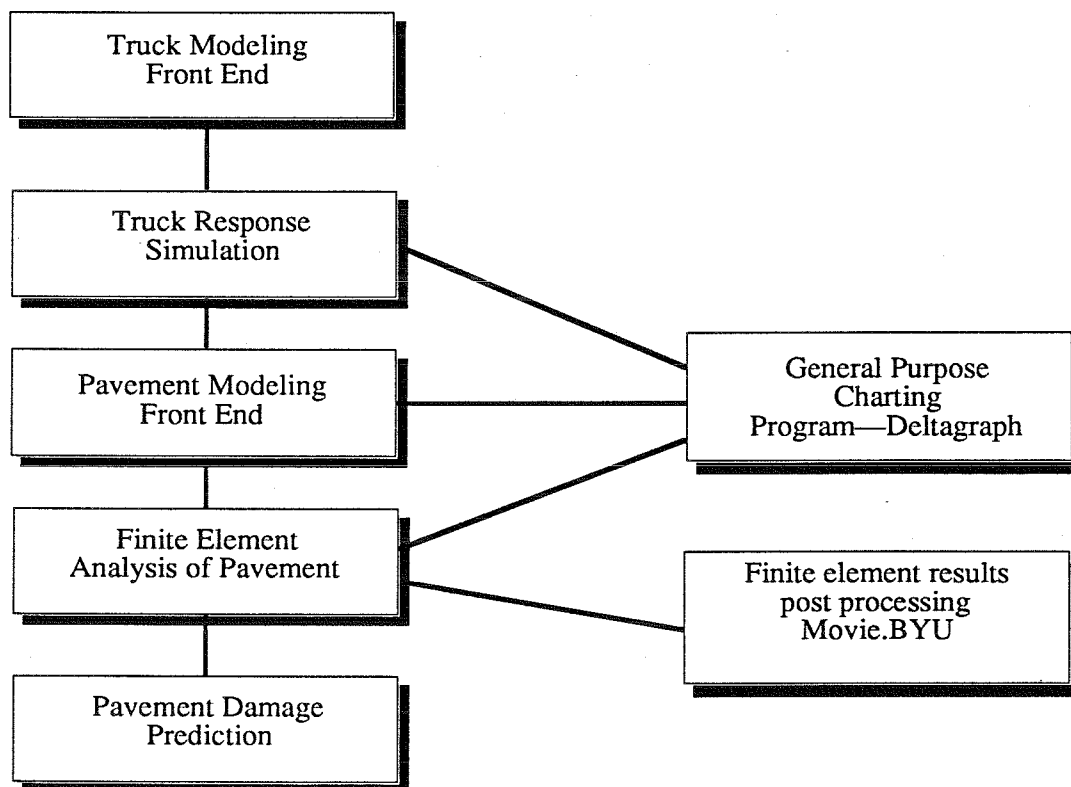


Figure 4-1
An Overview of the Integrated Software Environment

FORTRAN and are implemented using a Language Systems Fortran (Language Systems Corporation, 1990) compiler implemented under the Macintosh Programmers Workshop (MPW—see Apple Computer, Inc., 1990). For post-processing, DeltaGraph (DeltaPoint, Inc., 1990) is used as a general purpose charting program. DeltaGraph is able to plot a variety of charts from data stored in tabular form. The Movie.BYU program (Brigham Young University, 1990) is used for post-processing of the finite element results, including generation of stress and deformation contours.

The front end programs are described in the following sections. A theoretical description of the simulation programs is contained in earlier sections of this report. The front end programs are designed to create all the input data needed by the simulation programs. The post-processing programs, being commercial products, have their own user's manuals which should be consulted before their use.

Vehicle Modeling Front End Program

This section briefly describes a simple, intuitive and graphical front end program linked to the truck simulation code described earlier. The interface makes modeling of some basic truck configurations a routine matter. A general understanding of the vehicle modeling is the only pre-requisite for using this interface; a detailed knowledge of the simulation code is not necessary.

The interface is implemented in HyperCard for Apple Macintosh Computers. Variable values are entered on different "cards" or screens; each card requests data for a specific component of the vehicle. Left and right arrow "buttons" on the cards are used for navigating through a "stack" of cards. The data can be entered in any order and modified at any time.

The user begins by selecting the desired truck configuration from the card shown in Figure 4-2. Truck configurations are selected by (mouse) clicking on the appropriate graphic. Simulation control can be modified as shown in Figure 4-3.

From this point, the main program is launched and input is defined as the user progresses through a series of screens. Figure 4-4 shows the input screen that the user would see if a tandem axle semitrailer with a tandem axle trailer were selected.

The screen will appear with the cursor in the wheel base input box. The user can click into any input field to enter data, or use the tab key to cycle through the input boxes. A label explaining the required data appears next to each input box. On some cards, however, these labels are initially hidden to avoid screen clutter; the label for each input field is shown automatically when the cursor is within the boundaries of that box. The user can go back to a previous screen by simply clicking on the back arrow button located at the bottom of the screen. The next screen will ask the user for front tire and wheel parameters for the tractor, as shown in Figure 4-5. Again, the user can go back as many screens as desired by simply clicking on the back arrow. The next screen, not shown, asks the user for rear tire and wheel parameters for the tractor.

The next screen, shown in Figure 4-6, asks the user for information about the front axle of the tractor. Similarly, information about the rear axle parameters are requested on a screen shown in Figure 4-7.

WELCOME TO THE U OF IOWA TRUCK SIMULATION !

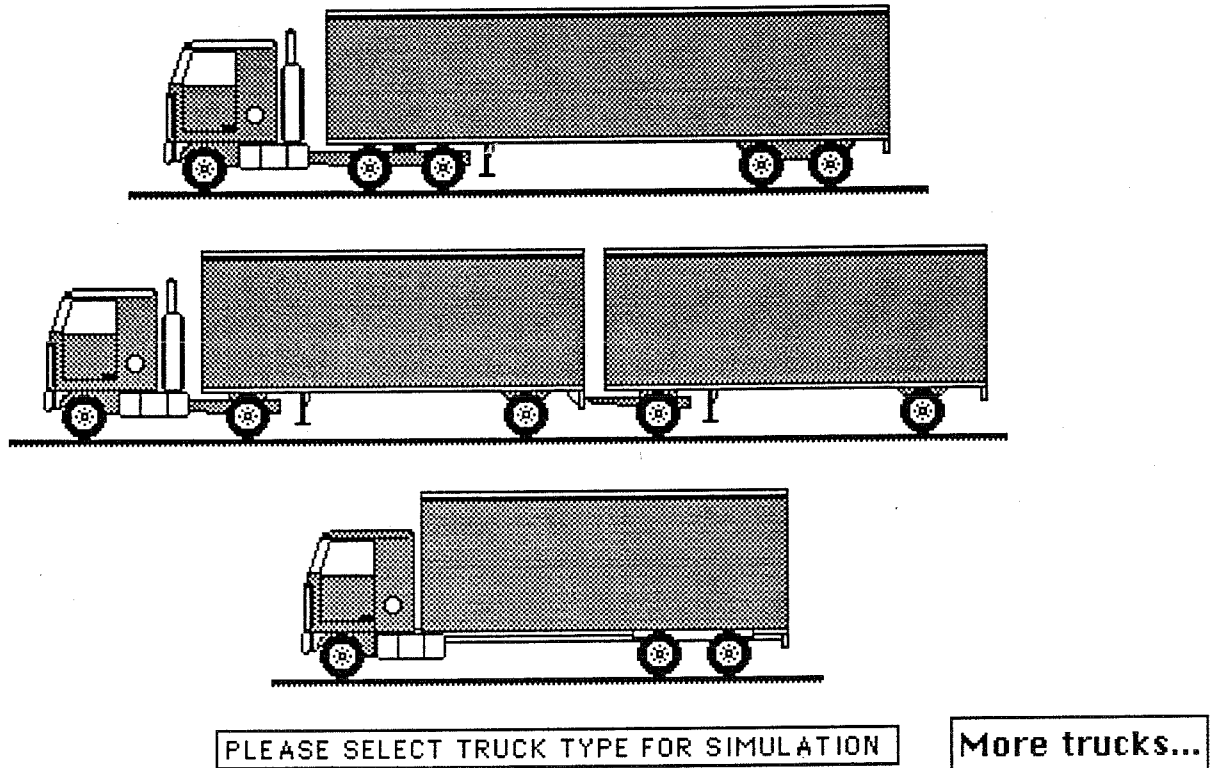


Figure 4-2
Vehicle Modeling Choices

STARTING TIME OF SIMULATION	0.0	seconds
ENDING TIME OF SIMULATION	5.0	seconds
VEHICLE SPEED	65.0	mph

TYPE OF ROAD PROFILE	random	rough
	flat	
	fault	
	sinusoidal	
	warping	

Simulate Truck 1

Figure 4-3
Simulation Control Card

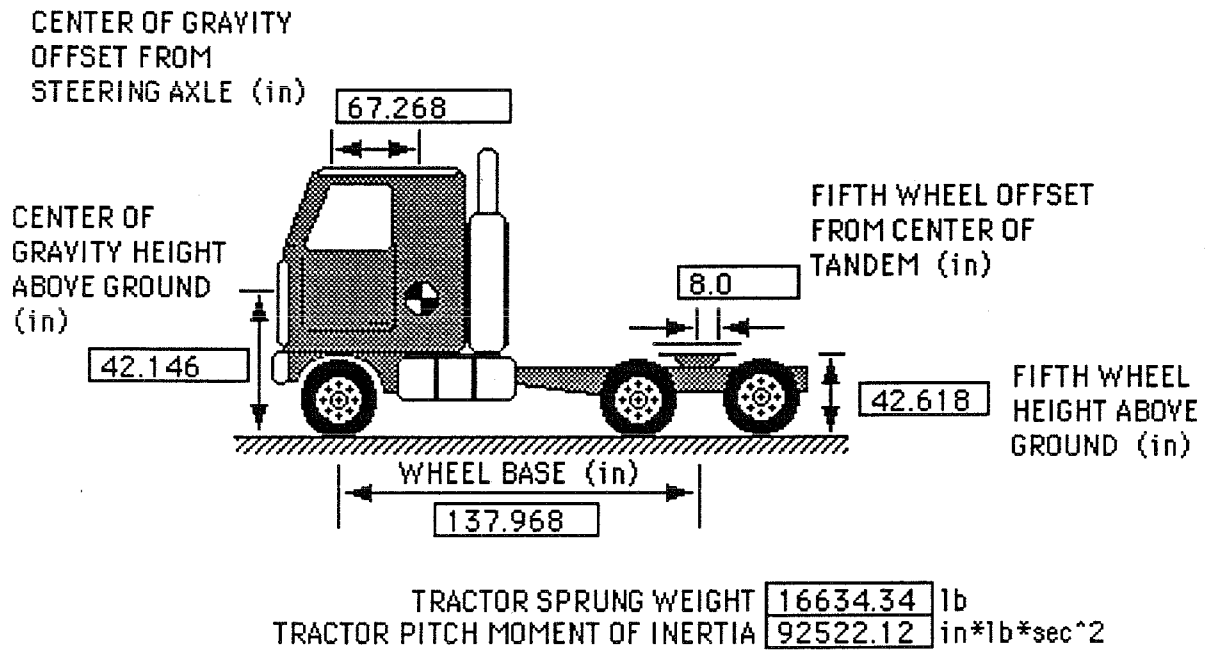
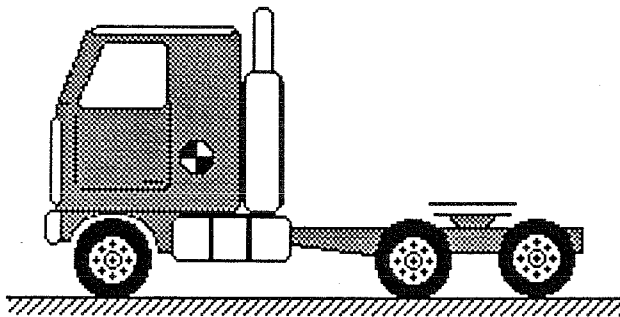
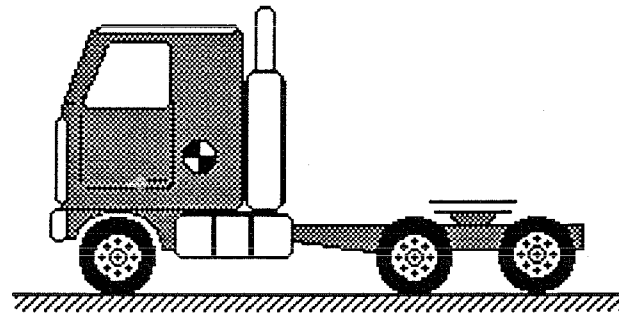


Figure 4-4
Tandem-Axle Tractor Data



TIRE SPRING RATE	4612.0	lb/in/tire
TIRE DAMPING RATE	2.5	lb*sec/in/tire
TIRE RADIUS (LOADED)	18.7	inch

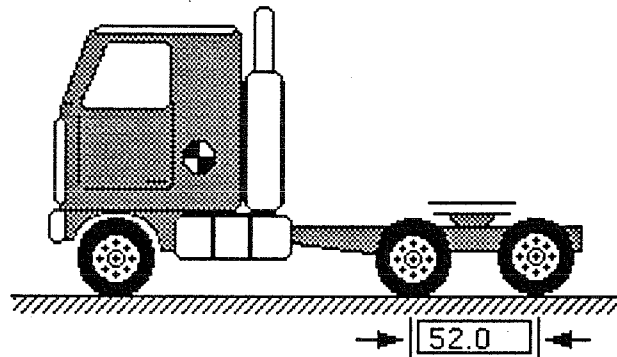
Figure 4-5
Tractor Front Tire and Wheel Parameters



SUSPENSION TYPE Leaf Air Walking

SUSPENSION SPRING RATE	files	
SHOCK ABSORBER DAMPING COEFFICIENT	0.0	lb*sec/in
UNSPRUNG WEIGHT OF STEERING AXLE	1473.57	lb
HEIGHT ABOVE GROUND OF SPRING ATTACHMENT	26.859	inch

Figure 4-6
Tractor Front Axle Parameters



SUSPENSION TYPE Leaf Air Walking

SUSPENSION SPRING RATE	files	
WEIGHT OF LEADING AXLE	2548.46	lb
WEIGHT OF TRAILING AXLE	2308.37	lb
HEIGHT ABOVE GROUND OF SPRING ATTACHMENT	28.1617	inches

TANDEM AXLE SEPARATION (in) 52.0

Figure 4-7
Tractor Rear Axle Parameters

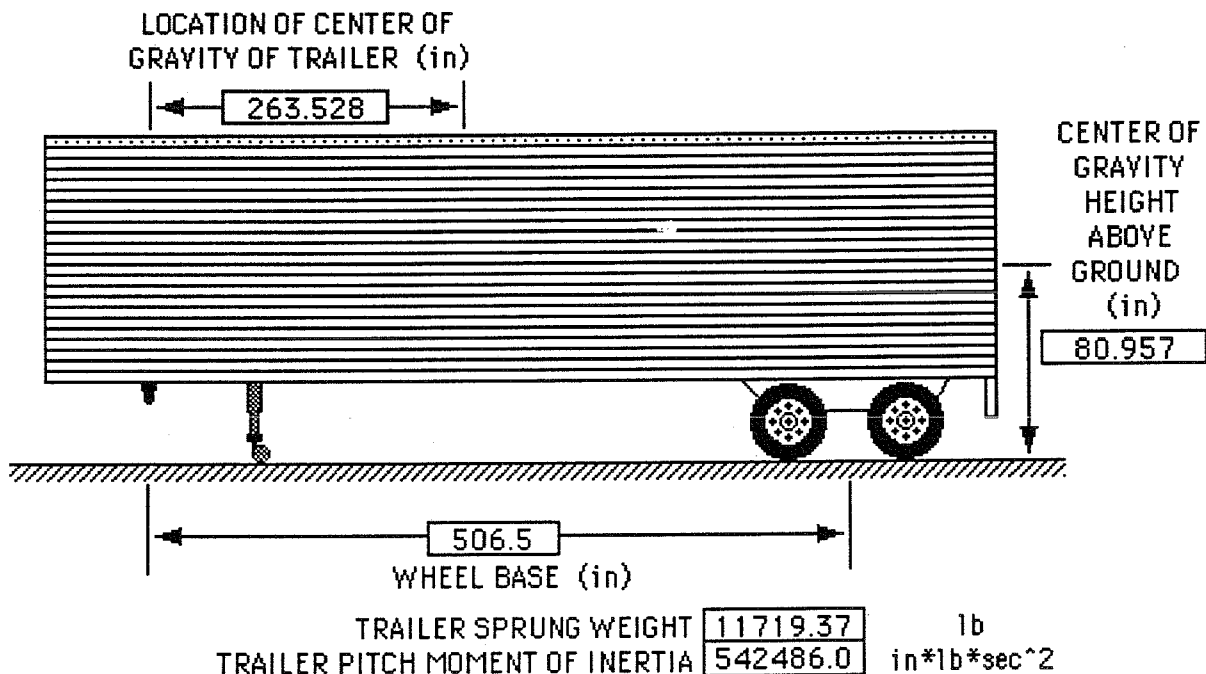


Figure 4-8
Trailer Parameters

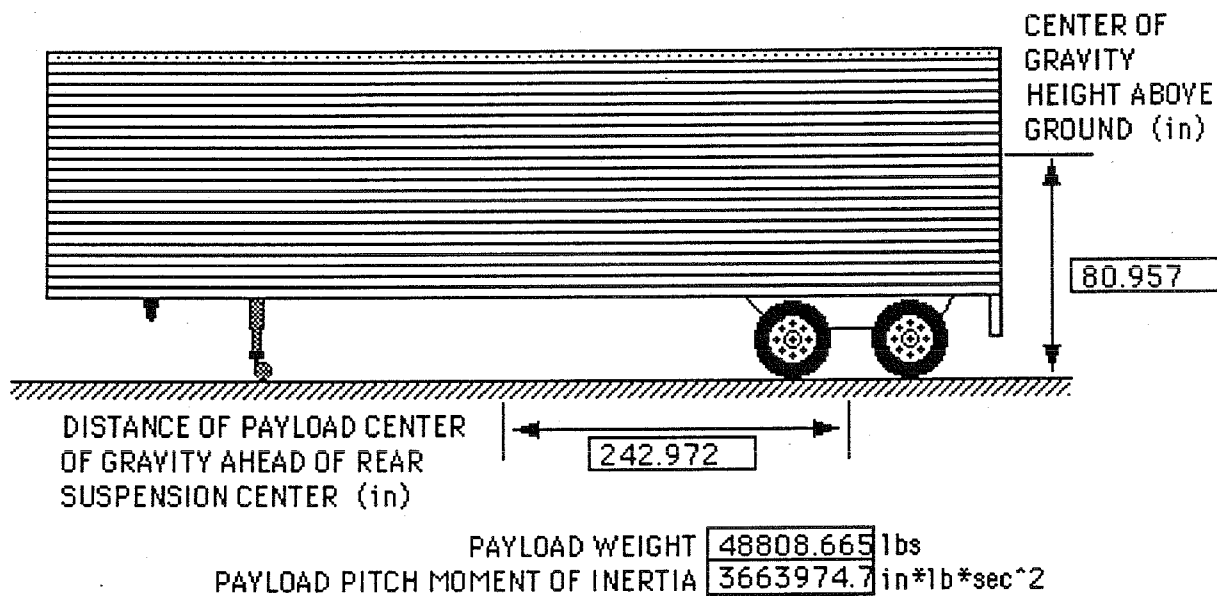
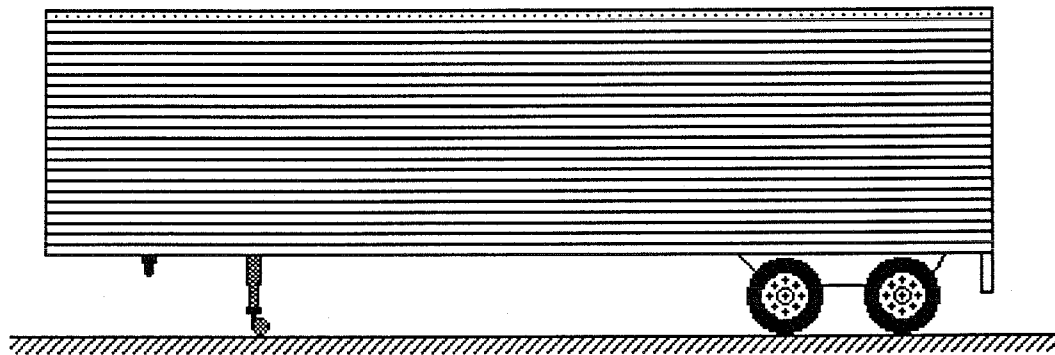


Figure 4-9
Trailer Payload Parameters

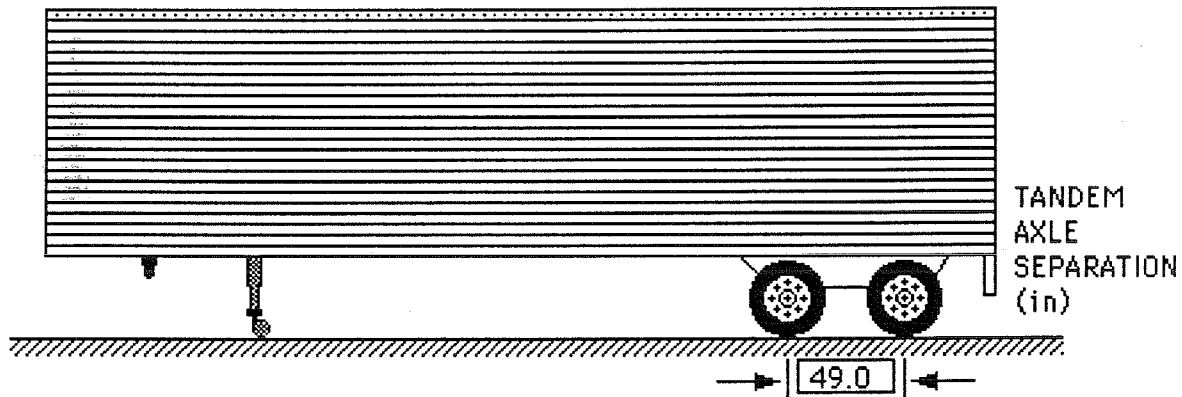
After the tractor parameters have all been entered, trailer parameters are requested. The initial screen is shown in Figure 4-8.

The trailer will be hauling some known or assumed payload. The weight of the payload and various other parameters are entered by the user on the screen shown in Figure 4-9.



TIRE SPRING RATE	4614.0	lb/in/tire
TIRE DAMPING RATE	2.5	lb*sec/in/tire
TIRE RADIUS (LOADED)	18.543	inch

Figure 4-10
Trailer Rear Tire and Wheel Parameters



SUSPENSION TYPE Leaf Air Walking

SUSPENSION SPRING RATE	files	
UNSPRUNG WEIGHT OF LEADING AXLE	1528.634	lb*in*sec ²
UNSPRUNG WEIGHT OF TRAILING AXLE	1528.634	lb*in*sec ²
HEIGHT ABOVE GROUND OF SPRING ATTACHMENT	29.811	inch

Figure 4-11
Trailer Rear Axle Parameters

Similar to the data required of the tractor, the trailer rear tire and wheel parameters are asked for in Figure 4-10.

Finally, the user must input rear axle parameters as shown in Figure 4-11.

Vehicle Response Simulation and Post-Processing of Simulation Results

The last card in the vehicle modeling front end program has a button which can trigger execution of the vehicle response simulation program. Any data not supplied by the front end program is directly requested by the simulation program. At the end of the program's execution, control is transferred back to the front end program. Another button on the last card can be used to execute the post-processing program for creating charts, for example, of the axle forces' time histories.

Pavement Modeling Front End Program

An easy-to-use interface for developing the finite element model of the pavement is described in this section. The interface is implemented using HyperCard on an Apple Macintosh computer, and automatically generates all of the necessary model data for the pavement analysis program from a minimum amount of information to be provided by the user. Examples of necessary data are: pavement slab length and width, the number of slabs to be included in the model, diameter of dowels, distance between dowels, material properties, and the location of the front axle of the truck on the pavement. Other pertinent information is calculated and written to a file which is used by the finite element program to perform a stress and fatigue analysis of the pavement.

The user begins by entering the physical and geometrical information of one pavement slab. The program assumes that all slabs used for the analysis are alike, and determines the number of slabs that are necessary. Data are entered into the appropriate spaces as shown in Figure 4-12.

The user may, at any time, click on an arrow that will move the program forward or back to another screen. If the user clicks on the forward arrow, the screen that comes up is used to define the finite element discretization of the pavement slabs and is shown in Figure 4-13. The user enters the number of elements desired along the length and width of the slab. The elements along the length of the slab are of uniform size, but the elements along the width of the slab are divided into two groups. The number of elements along the travel path of the truck should be approximately two times the number of elements for the remaining width of the slab. A large number of elements will generally mean more accurate results; however, the computational effort increases dramatically with the increase in the number of elements. For a 20-foot pavement segment, reasonable results are obtained using the distribution of elements shown in Figure 4-13. Note that it is assumed that the truck travel path is along the bottom half of the pavement.

The user must also enter information about the dowels in the next screen, shown in Figure 4-14. The finite element program can only analyze the effect of the dowels when they are located at the element nodes. Using the data entered on this screen, the interface program defines an "equivalent" dowel size such that the total area of dowels across the width of the slab remains constant. These equivalent dowels are then assumed for all adjacent nodes across the joints in the pavement.

The next step is to define a wheel path by entering the required parameters on the screen shown in Figure 4-15. These parameters determine the location of the first axle of the

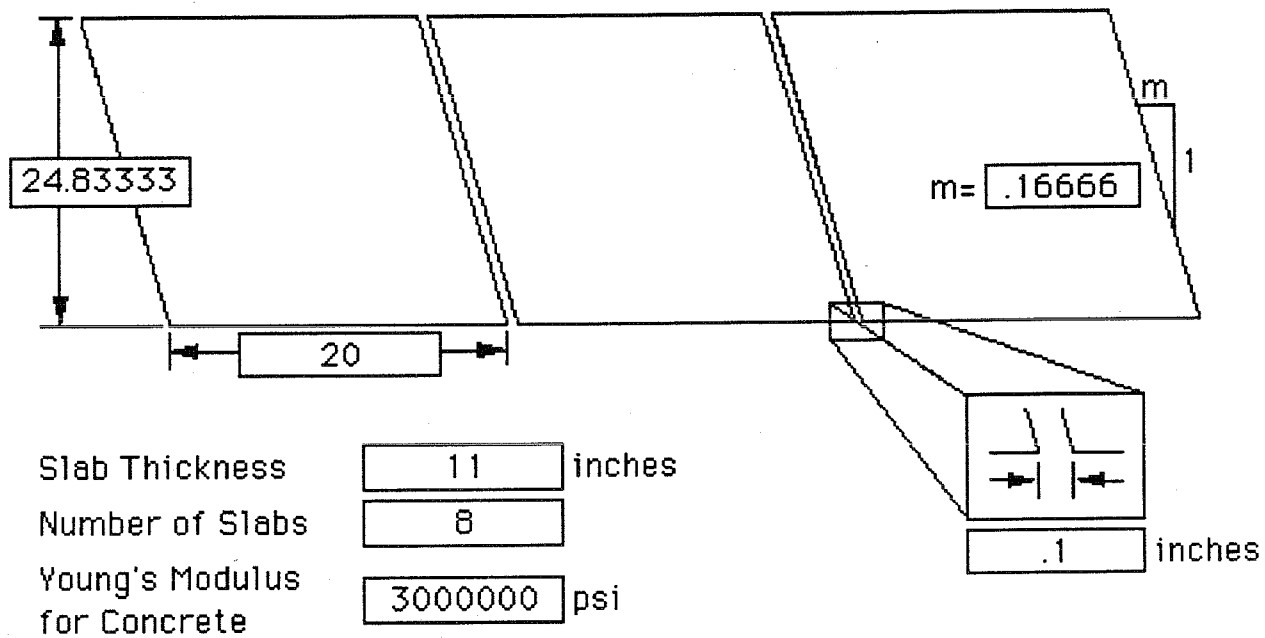


Figure 4-12
Pavement Slab Data

ELEMENT INFORMATION

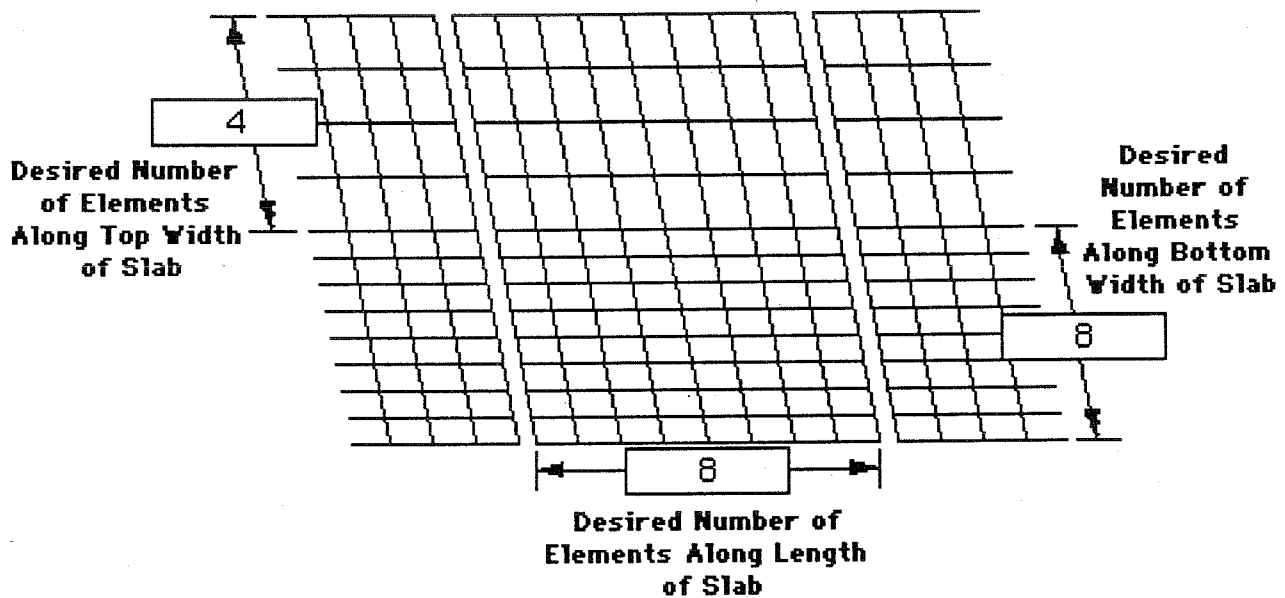


Figure 4-13
Pavement Discretization Into Finite Elements

truck that was defined earlier. After the wheel path is defined, the program generates both the number of slabs necessary for a fatigue analysis and the necessary boundary conditions.

There are other screens where the type of analysis (linear or non-linear) and the type of damage to be considered, such as pumping or fatigue, may be defined. Other screens then ask for the appropriate information depending upon the type of analysis and damage consideration desired. One example is shown in Figure 4-16.

The user must also enter material properties to be used for the analysis. Several different types of concrete and subgrade materials may be defined. If the concrete is reinforced, then steel properties must also be defined. The pavement cross section is assumed to be divided into layers that are numbered, starting from the bottom. Each layer can have different material properties. There may be up to fifteen layers of subgrade, concrete and steel materials.

After entering this information in the appropriate fields indicated by the interface, the user clicks on the button marked "Analyze" and the interface generates the necessary data and sends it to the finite element program. Data should be entered in all of the available spaces, otherwise the program will not generate the data file, but instead will take the user back to the screen where input data is required.

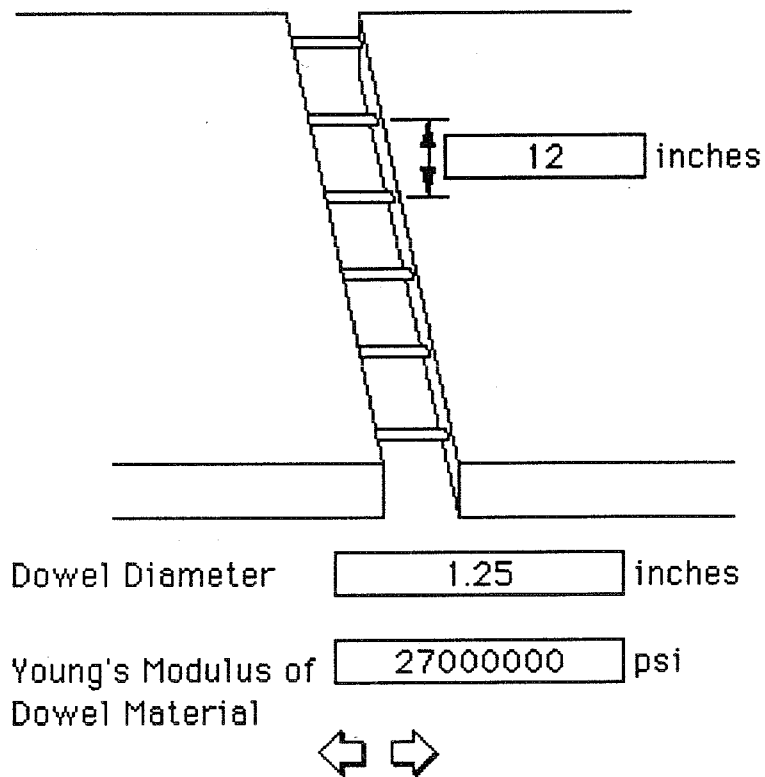


Figure 4-14
Dowel Data

Pavement Response Simulation and Post-Processing of Simulation Results

The last card in the pavement modeling front end program has a button that can trigger execution of the finite element response analysis and pavement damage simulation program. At the end of the execution, the Movie.BYU program can be used to prepare stress and deformation contours. Finally DeltaGraph will produce x-y and bar charts of the results.

LOCATION OF FRONT AXLE OF SEMI TRACTOR WITH RESPECT TO THE EDGE OF THE PAYEMENT

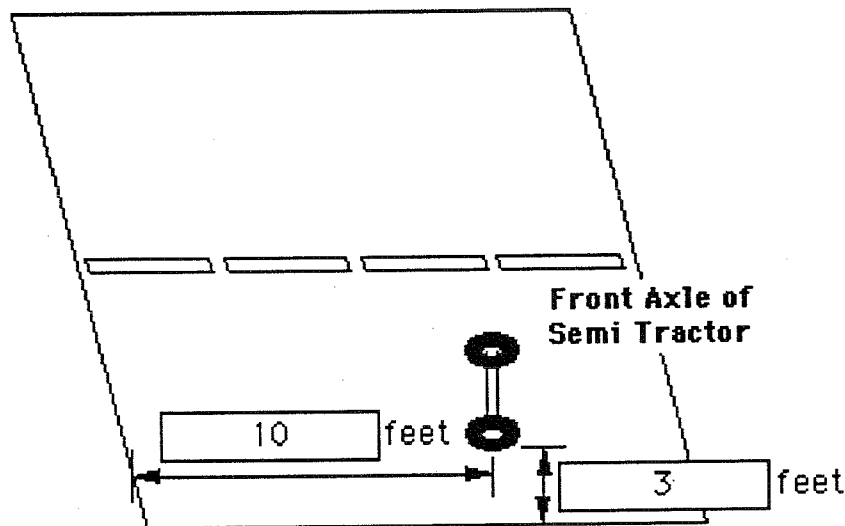


Figure 4-15
Truck Travel Path

General Information

Number of concrete material sets
 Number of steel material sets

- Linear Analysis (subgrade is to resist tension)
 Non-Linear Analysis (subgrade is not to resist tension)

- Consider Fatigue Damage
 Do Not Consider Fatigue Damage

- Consider Pumping Damage
 Do Not Consider Pumping Damage

Total number of times at which
 damage is to be calculated

Total number of cycles to be run



Figure 4-16
General Pavement Analysis Information

APPENDIX

Matrix Formulation of the Elastoplastic Constitutive Matrix

The yield function can be written as

$$f(\sigma) = K(\kappa) \quad (1)$$

Rearranging equation 1 we get

$$F(\sigma, \kappa) = f(\sigma) - K(\kappa) = 0.0 \quad (2)$$

and

$$dF = \frac{\partial F}{\partial \sigma} d\sigma + \frac{\partial F}{\partial \kappa} d\kappa = 0.0 \quad (3)$$

or

$$\mathbf{a}^T d\sigma - A d\lambda = 0.0 \quad (4)$$

where

$$\mathbf{a}^T = \frac{\partial F}{\partial \sigma} = \left[\frac{\partial F}{\partial \sigma_x}, \frac{\partial F}{\partial \sigma_y}, \frac{\partial F}{\partial \sigma_z}, \frac{\partial F}{\partial \tau_{yz}}, \frac{\partial F}{\partial \tau_{zx}}, \frac{\partial F}{\partial \tau_{xy}} \right] \quad (5)$$

$$A = - \frac{1}{d\lambda} \frac{\partial F}{\partial \kappa} dk \quad (6)$$

Vector \mathbf{a} is termed Flow Vector.

The incremental relationship between stresses and strains for elastoplastic deformation can be written as

$$d\varepsilon_{ij} = \frac{d\sigma_{ij}}{2\mu} + \frac{(1-2\nu)}{E} \delta_{ij} d\sigma_{kk} + d\lambda \frac{\delta f}{\delta \sigma_{ij}}$$

or, from the above equations

$$d\varepsilon = [D]^{-1} d\sigma + d\lambda \frac{\partial F}{\partial \sigma} \quad (7)$$

with $[D]$ = elastic constitutive matrix.

$$\text{Let us define } \mathbf{d}_D^T = \mathbf{a}^T D \quad (8)$$

Premultiplying equation 7 by equation 8

$$\mathbf{d}_D^T d\varepsilon = \mathbf{d}_D^T [D]^{-1} d\sigma + d\lambda \mathbf{d}_D^T \frac{\partial F}{\partial \sigma} = \mathbf{a}^T d\sigma + d\lambda \mathbf{d}_D^T \frac{\partial F}{\partial \sigma}$$

Using equation 4

$$\mathbf{d}_D^T d\boldsymbol{\varepsilon} = A d\lambda + d\lambda \mathbf{d}_D^T \frac{\partial F}{\partial \sigma} \quad (9)$$

or

$$d\lambda = \frac{\mathbf{a}^T D d\boldsymbol{\varepsilon}}{A + \mathbf{d}_D^T \mathbf{a}} \quad (10)$$

Equation 10 in equation 7 gives

$$d\boldsymbol{\varepsilon} = [D]^{-1} d\sigma + \frac{\mathbf{a}^T D d\boldsymbol{\varepsilon}}{A + \mathbf{d}_D^T \mathbf{a}} \frac{\partial F}{\partial \sigma}$$

$$d\sigma = \left[D - \frac{\mathbf{a}^T D \mathbf{a} D}{A + \mathbf{d}_D^T \mathbf{a}} \right] d\boldsymbol{\varepsilon} \quad (11)$$

$$d\sigma = \left[D - \frac{\mathbf{d}_D \mathbf{d}_D^T}{A + \mathbf{d}_D^T \mathbf{a}} \right] d\boldsymbol{\varepsilon} \quad (12)$$

or

$$d\sigma = D_{ep} d\boldsymbol{\varepsilon} \quad (13)$$

It can be shown that

$$A = H' = \frac{E_t}{\left(1 - \frac{E_t}{E}\right)} \quad (14)$$

$$d\lambda = d\bar{\varepsilon}_p \quad (15)$$

where

E_t elasto-plastic tangent modulus

E initial tangent modulus

$d\bar{\varepsilon}_p$ effective plastic strain defined as

$$d\bar{\varepsilon}_p = \sqrt{\frac{2}{3}} \left\{ (d\varepsilon_{ij})_p (d\varepsilon_{ij})_p \right\}^{\frac{1}{2}} \quad (16)$$

$(d\varepsilon_{ij})_p$ plastic component of the strain increment

Alternative form of the yield criterion for numerical computation—Nayak and Zienkiewicz, 1972a,1972b

The yield criterion, $F(\sigma, \kappa)$, can be written as a function of I_1, J_2 and θ , with

$$\sin(3\theta) = -\frac{4J_3}{r^3} = -\frac{3\sqrt{3}}{2} - \frac{J_3}{(J_2)^{3/2}} \quad (17)$$

$$\text{with } -\frac{\pi}{6} \leq \theta \leq \frac{\pi}{6}$$

In order to calculate D_{ep} we write a as

$$\mathbf{a}^T = \frac{\partial F(I_1, J_2, \theta)}{\partial \sigma} = \frac{\partial F}{\partial I_1} \frac{\partial I_1}{\partial \sigma} + \frac{\partial F}{\partial (J_2)^{1/2}} \frac{\partial (J_2)^{1/2}}{\partial \sigma} + \frac{\partial F}{\partial \theta} \frac{\partial \theta}{\partial \sigma} \quad (18)$$

with

$$\sigma = \{ \sigma_x, \sigma_y, \sigma_z, \tau_{yz}, \tau_{xz}, \tau_{xy} \}$$

differentiating equation 17 we obtain

$$\frac{\partial \theta}{\partial \sigma} = \frac{-\sqrt{3}}{2 \cos(3\theta)} \left[\frac{1}{(J_2)^{3/2}} \frac{\partial (J_3)}{\partial \sigma} - \frac{3 J_3}{(J_2)^2} \frac{\partial (J_2)^{1/2}}{\partial \sigma} \right] \quad (19)$$

Equation 17 and 19 in equation 18:

$$\mathbf{a} = C_1 \mathbf{a}_1 + C_2 \mathbf{a}_2 + C_3 \mathbf{a}_3 \quad (20)$$

with

$$\mathbf{a}_1^T = \frac{\partial (I_1)}{\partial \sigma} = \{ 1, 1, 1, 0, 0, 0 \} \quad (21)$$

$$\mathbf{a}_2^T = \frac{\partial (J_2)^{1/2}}{\partial \sigma} = \frac{1}{2(J_2)^{1/2}} \{ s_x, s_y, s_z, 2\tau_{yz}, 2\tau_{xz}, 2\tau_{xy} \} \quad (22)$$

$$\begin{aligned}
 \mathbf{a}_3^T = \frac{\partial(J_3)}{\partial\sigma} = & \left\{ (s_y s_z - \tau_{yz}^2 + \frac{J_2}{3}), (s_x s_z - \tau_{xz}^2 + \frac{J_2}{3}), \right. \\
 & (\sigma_x \sigma_y - \tau_{xy}^2 + \frac{J_2}{3}), 2(\tau_{xy} \tau_{xz} - \sigma_x \tau_{yz}), \\
 & \left. 2(\tau_{xy} \tau_{xz} - \sigma_x \tau_{yz}), 2(\tau_{xy} \tau_{xz} - \sigma_x \tau_{yz}) \right\} \quad (23)
 \end{aligned}$$

and

$$C_1 = \frac{\partial F}{\partial I_1} \quad (24)$$

$$C_2 = \left(\frac{\partial F}{(J_2)^{1/2}} - \frac{\tan(3\theta)}{(J_2)^{1/2}} \frac{\partial F}{\partial \theta} \right) \quad (25)$$

$$C_3 = \frac{-\sqrt{3}}{2 \cos(3\theta)} \frac{1}{(J_2)^{3/2}} \frac{\partial F}{\partial \theta} \quad (26)$$

References

- AASHO. 1962. The AASHO Road Test, Report 7. Special Report 61G. Washington, DC: Highway Research Board.
- Apple Computer, Inc. 1990. *Macintosh Programmers Workshop Reference Manual*. Cupertino, CA: Apple Computer.
- Ballinger, C.A. 1972. *Effect of Load Variations on the Flexural Fatigue Strength of Plain Concrete*. Washington, DC: Federal Highway Administration.
- Bradbury, R.D. 1938. *Reinforced Concrete Pavements*. Washington DC: Wire Reinforcement Institute.
- Brigham Young University. 1990. *Movie.BYU Reference Manual*. Provo, UT: Brigham Young University.
- Cebon, D. 1988a. "Theoretical road damage due to dynamic tire forces of heavy vehicles: Part 1: dynamic analysis of vehicles and road surfaces," *Proceedings of the Institution of Mechanical Engineers*, Vol. 202, No. C2, pp. 106-108.
- Cebon, D. 1988b. "Theoretical road damage due to dynamic tire forces of heavy vehicles: Part 2: simulated damage caused by a tandem-axle vehicle," *Proceedings of the Institution of Mechanical Engineers*, Vol. 202, No. C2, pp. 109-117.
- Christofieds, N. 1986. *Graph Theory: An Algorithmic Approach*. New York, NY: Academic Press.
- Clemer, H.F. 1922. "Fatigue of Concrete," *Proc. American Society of Testing and Materials*, Vol. 22, Part. 2, pp. 409-419.
- Computer Aided Design Software, Inc. 1988. *DADS User's Manual, Rev. 5.0*. Oakdale, IA: CADSI.
- Delta Point, Inc. 1990. *DeltaGraph: The Ultimate Charting and Graphics Solution*. Monterey, CA: DeltaPoint.
- Featherstone, R. 1987. *Robot Dynamics Algorithms*. Boston, MA: Kluwer Academic Publishers.
- Figueiras, J.A., and D.R. J. Owen. 1984a. "Analysis of Elasto-Plastic and Geometrically Nonlinear Anisotropic Plates and Shells." In *Finite Element Software for Plates and Shells*. E. Hinton and D.R.J. Owen, ed. Swansea, U.K.: Pineridge Press, pp. 235-326.
- Figueiras, J.A. , and D.R. J. Owen. 1984b. "Ultimate Load Analysis of Reinforced Concrete Plates and Shells, Including Geometric Nonlinear Effects." In *Finite Element Software for Plates and Shells*. E. Hinton and D.R.J. Owen, ed. Swansea, U.K.: Pineridge Press, pp. 327-388.
- Frieberg, B.F. 1940. "Design of Dowels in Transverse Joints of Concrete Pavements," *Transactions American Society of Civil Engineering*, Vol. 105, pp. 1076-1095.
- Gulden, W. 1983. "Experience in Georgia with Drainage of Jointed Concrete Pavements." In *International Seminar on Drainage and Erodability*. Conference held at Paris, France.
- Haug, Edward J. 1989. *Computer Aided Kinematics and Dynamics of Mechanical Systems, Volume 1: Basic Methods*. Boston, MA: Allyn and Bacon.
- Hetenyi, M. 1946. *Beams on Elastic Foundation*. Ann Arbor, MI: University of Michigan Press.
- Hilsdorf, H.K., and C.E. Kesler. 1966. "Fatigue Strength of Concrete Under Varying Flexural Stresses," *Journal of the American Concrete Institute*, Vol. 63, October, pp. 1059-1075.

- Holmen, J.O. 1982. "Fatigue of Concrete by Constant and Variable Amplitude Loading." In *Fatigue of Concrete Structures, SP-75*. Detroit, MI: American Concrete Institute.
- Hu, Garrick. 1988. "Use of Road Simulator for Measuring Dynamic Wheel Loads." In *Vehicle/Pavement Interaction: where the truck meets the road, SP-765*. Warrendale, PA: Society of Automotive Engineers, pp. 61-68.
- Kading, R. R., and M. J. Vanderploeg. 1985. *Dynamic Analysis of Vehicles Using a Rigid Body Dynamics General Purpose Computer Code*. Technical Report 85-6. Iowa City, IA: Center for Computer Aided Design, University of Iowa.
- Kesler, C.E. 1953. *Significance of Tests and Properties of Concrete-Making Materials*. Special Technical Publication 169A. American Society of Testing and Materials.
- Klaiber, F.W., T.L. Thomas, and D.Y. Lee. 1979. *Fatigue Behavior of Air-Entrained Concrete: Phase II*. Ames, IA: Engineering Research Institute, Iowa State University.
- Kupfer, H., H. Hilsdorf, and H. Rusch. 1969. "Behavior of Concrete under Biaxial Stresses," *Journal of the American Concrete Institute*, Vol. 66, No. 8, pp. 656-666.
- Language Systems Corporation. 1990. *Language Systems Fortran Reference Manual*. Herndon, VA: Language Systems Corporation.
- Larralde, J. 1984. *Structural Analysis of Rigid Pavements with Pumping*. PhD Dissertation. West Lafayette, IN: Purdue University.
- Li, Chang-Jin. 1989. "A New Lagrangian Formulation of Dynamics for Robot Manipulators," *Journal of Dynamic Systems, Measurement, and Control*, Vol. 111 (December), pp. 559-567.
- MacAdam, C. C. et al. 1980. *A Computerized Model for Simulating the Braking and Steering Dynamics of Trucks, Tractor-Semitrailers, Doubles, and Triples Combinations: User's Manual—Phase IV*. Report No. UM-HSRI-80-58. Ann Arbor, MI: Highway Safety Research Institute, University of Michigan.
- Markow, Michael J., J. Karl Hedrick, Brian D. Brademeyer, and Edward Abbo. 1988. "Analyzing the interactions between dynamic vehicle loads and highway pavements," *Transportation Research Record* 1196, pp. 161-169.
- Miner, M. 1945. "Cumulative Damage in Fatigue," *Transactions ASCE*, Vol. 67, pp. A159-A164.
- Murdock, J.W., and C.E. Kesler. 1958. "Effect of Range of Stress on Fatigue Strength of Plain Concrete Beams," *Journal of the American Concrete Institute*, Vol. 55 (August), pp. 221-232.
- Nayak, G.C., and O.C. Zienkiewicz. 1972a. "Convenient Form of Stress Invariants for Plasticity," *Journal of the Structural Division, ASCE*, Vol. 98, No. ST4 (April), pp. 949-954.
- Nayak, G.C., and O.C. Zienkiewicz. 1972b. "Elasto-Plastic Stress Analysis. A Generalization for Various Constitutive Relations, Including Strain Softening," *International Journal for Numerical Methods in Engineering*, Vol. 5, No. 1 (September), pp. 113-135.
- Neville, A.M. 1973. *Properties of Concrete*. New York, NY: John Wiley and Sons, Inc.
- Nordby, G. M. 1958. "Fatigue of Concrete - A Review of Research," *Journal of the American Concrete Institute*, Vol. 55, August, pp. 191-220.
- Orlandea, N., M. A. Chase, and D. A. Calahn. 1977. "A Sparsity-Oriented Approach to Dynamic Analysis and Design of Mechanical Systems, Part I and II," *Journal of Engineering for Industry, Transactions of the ASME*, Vol. 99 (August), pp. 773-784.

- Pickett, G., and G.K. Ray. 1951. "Influence Charts for Concrete Pavements," *Transactions ASCE*, Vol. 116, pp. 49-73.
- Raithby, K.D., and J.W. Galloway. 1974. "Effects of Moisture Condition, Age and Rate of Loading on Fatigue of Plain Concrete." In *Abeles Symposium: Fatigue of Concrete, SP-41*. Detroit, MI: American Concrete Institute, pp. 15-34.
- Sayers, M., and T. D. Gillespie. 1983. "Dynamic Pavement/Wheel Loading for Trucks with Tandem Suspension." In *Proceedings of the 8th IAVSD Symposium*.
- Schiehlen, Werner, ed. 1990. *Multibody Systems Handbook*. New York, NY: Springer-Verlag.
- Small, Kenneth A., Clifford Winston, and Carol A. Evans. 1989. *Road Work: A New Highway Pricing and Investment Policy*. Washington, DC: Brookings Institution.
- Stoner, J. W., M. A. Bhatti, S. S. Kim, J. K. Koo, I. Molinas-Vega, and B. Amhof. 1990. *Dynamic Simulation Methods for Evaluating Motor Vehicle and Roadway Design and Resolving Policy Issues*. Prepared for the Midwest Transportation Center. Iowa City, IA: Public Policy Center, University of Iowa.
- Sutherland, E. C., and H. D. Cashell. 1945. "Structural Efficiency of Transverse Weakened Plane Joints," *Public Roads*, Vol. 24, pp. 88-97.
- Teller, L. W., and H. D. Cashell. 1958. "Performance of Doweled Joints Under Repetitive Loading," *Public Roads*, Vol. 30, pp. 1-24.
- Teller, L. W., and E. C. Sutherland. 1938. "A Study of the Structural Action of Several Types of Transverse and Longitudinal Joint Designs," *Public Roads*, Vol. 17, pp. 143-192.
- Timoshenko, S., and J. Lessels. 1925. *Applied Elasticity*. Pittsburgh, PA: Westinghouse Technical Night School Press.
- Troxell, G.E., H.F. Davis, and J.W. Kelly. 1968. *Composition and Properties of Concrete*. New York, NY: McGraw-Hill.
- Ullidtz, Per. 1987. *Pavement Analysis*. New York, NY: Elsevier.
- Walker, Michael W., and David E. Orin. 1982. "Efficient Dynamic Computer Simulation of Robotic Mechanisms," *Journal of Dynamic Systems, Measurement, and Control*, Vol. 104, No. 3, pp. 205-211.
- Wehage, R. A., and E. J. Haug. 1982. "Generalized Coordinate Partitioning for Dimensional Reduction in Analysis of Constrained Dynamic Systems," *Journal of Mechanical Design, Transactions of the ASME*, Vol. 104 (January), pp. 247-255.
- Westergaard, H.M. 1947. "New Formulas for Stresses in Concrete Pavements of Airfields," *Proceeding ASCE*, Vol. 73, No. 5.
- Yoder, E.J., and M.W. Witczak. 1975. *Principles of Pavement Design*. John Wiley and Sons Inc.

This document was prepared on Apple Macintosh IIcx and SE/30 computers, printed on an Apple Laserwriter II NT, using the following software: Aldus Pagemaker 4.01, Microsoft Word 4.0, DeltaGraph 1.5, Canvas 2.1, EndNote Plus, and MathWriter.

